

Spring 5-17-2013

## Nanomaterials for Biological Applications: Drug Delivery and Bio-sensing

Hui Ma  
wendy9494@gmail.com

Follow this and additional works at: <https://scholarworks.uno.edu/td>



Part of the [Inorganic Chemistry Commons](#), [Materials Chemistry Commons](#), and the [Nanoscience and Nanotechnology Commons](#)

---

### Recommended Citation

Ma, Hui, "Nanomaterials for Biological Applications: Drug Delivery and Bio-sensing" (2013). *University of New Orleans Theses and Dissertations*. 1647.  
<https://scholarworks.uno.edu/td/1647>

This Dissertation is protected by copyright and/or related rights. It has been brought to you by ScholarWorks@UNO with permission from the rights-holder(s). You are free to use this Dissertation in any way that is permitted by the copyright and related rights legislation that applies to your use. For other uses you need to obtain permission from the rights-holder(s) directly, unless additional rights are indicated by a Creative Commons license in the record and/or on the work itself.

This Dissertation has been accepted for inclusion in University of New Orleans Theses and Dissertations by an authorized administrator of ScholarWorks@UNO. For more information, please contact [scholarworks@uno.edu](mailto:scholarworks@uno.edu).

# Nanomaterials for Biological Applications: Drug Delivery and Bio-sensing

A Dissertation

Submitted to the Graduate Faculty of the  
University of New Orleans  
In partial fulfillment of the  
Requirements for the degree of

Doctor of Philosophy  
in  
Chemistry

by

Hui Ma

B.S. University of Science and Technology of China, 2007  
M.S. University of New Orleans, 2010

May, 2013

Copyright 2013, Hui Ma

## ACKNOWLEDGEMENTS

This research work was conducted at Department of Chemistry and Advanced Materials Research Institute (AMRI) at University of New Orleans (UNO), under the supervision of Professor Weilie Zhou.

First, I would like to express my most sincere gratitude to my advisor Professor Zhou for recruiting me and providing consistent support through all the years of my study in his group. Thank to his disciplinary supervision, inspiring instruction and generous help, I'm able to successfully finish my work in time. I really enjoyed doing my work in his group, and I could not have imagined having a better advisor for my graduate study.

I want to thank my committee members: Prof. O'Connor, Prof. Wiley, Prof. Cai and former committee member Prof. Poudeu. They shared a lot of valuable comments and suggestions with me on my projects and thesis.

I want to thank our collaborators, Dr. Seth Pincus and Dr. Kejing Song from Children's Hospital of New Orleans, Dr. Mark DeCoster from Louisiana Tech University, and Dr. Jost Geottert and Dr. Yoonyoung Jin from Louisiana State University, for their brilliant input for my projects and unreserved help with the instrumentation.

I also want to thank many of my group members and friends: Dr. Jiajun Chen, Dr. Hongtao Yu, Miss. Jie Zhou, Miss. Sarah Wozny, Mr. Haiqiao Su and Mr. Satish Rai. They help me and support me during my Ph.D. studies. I'm indebted to Dr. Zhongming Zeng for him being incredibly patient and informative while training me for e-beam lithography. I also want to thank Dr. Kun Yao for many helpful discussions about the property of field effect transistor, and Dr. Kai Wang and Dr. Baobao Cao for their assistance in nanowire synthesis and electron microscopy.

I gratefully acknowledge the support of this work by a research grant from Louisiana Board of Regents Contract No. LEQSF(2007-12)-ENH-PKSFI-PRS-04.

Last, I want to thank my family: my husband Haiou for his understanding and support. Without him, I cannot finish this work. I want to show my deepest appreciation to my parents Ruichang Ma and Junrui Dong who gave birth to me, raised me and support me for the last twenty-eight years.

## Table of Contents

|                       |      |
|-----------------------|------|
| List of Schemes ..... | viii |
| List of Figures ..... | ix   |
| List of Tables .....  | xiv  |
| Abstract .....        | xv   |

### **Part One: Magnetic Hollow Mesoporous Silica nanostructures for bio-medicine application**

#### **Chapter I: Introduction** **1**

|  |    |
|--|----|
| 1.1 Synthesis of uniform mesoporous silica nanoparticles (MSN).....  | 2  |
| 1.2 Synthesis of hollow mesoporous silica nanoparticles (HMSN) .....   | 4  |
| 1.2.1 Hard template method for synthesizing HMSN .....   | 4  |
| 1.2.2 Soft template method for synthesizing HMSN.....  | 6  |
| 1.2.3 Selective etching for synthesizing HMSN.....   | 7  |
| 1.3 Introducing superparamagnetic iron oxide nanoparticles (SPION) to mesoporous silica nanoparticle (MSN) ..... | 8  |
| 1.3.1 SPION/MSN core/shell structure.....  | 9  |
| 1.3.2 SPION embedded in MSN framework .....  | 10 |
| 1.3.3 Rattle type SPION core in MSN shell .....  | 11 |
| 1.4 Further functionalization and applications of SPION/MSN .....  | 12 |
| 1.4.1 Drug/gene delivery.....  | 13 |
| 1.4.2 Fluorescence imaging .....   | 15 |
| 1.5 References .....   | 16 |

#### **Chapter II: Magnetic porous hollow silica nanostructures from CaCO<sub>3</sub> template for drug delivery application** **21**

|   |    |
|---|----|
| 2.1 Introduction.....   | 21 |
| 2.2 Experimental .....  | 23 |
| 2.3 Result and discussion.....  | 28 |
| 2.3.1 Preparation of Fe <sub>3</sub> O <sub>4</sub> /CaCO <sub>3</sub> composite nanoparticle templates ..... | 29 |

|   |    |
|---|----|
| 2.3.2 Synthesis of Magnetic Porous Hollow Silica Nanospheres (MPHSNs) and BET analysis. | 30 |
| 2.3.3 Synthesis of Magnetic Porous Hollow Silica Nanotubes (MPHSNTs) and BET analysis.  | 33 |
| 2.3.4 Magnetic measurements. ....   | 37 |
| 2.3.5 Drug loading and releasing. ....  | 38 |
| 2.3.6 Toxicity study. ....  | 41 |
| 2.4 Conclusion .....  | 43 |
| 2.5 References .....  | 44 |

### **Chapter III: Magnetic porous hollow silica nanospheres (MPHSNs) templated from polystyrene beads** **46**

|   |    |
|---|----|
| 3.1 Introduction .....  | 46 |
| 3.2 Experimental .....  | 47 |
| 3.3 Result and discussion: .....  | 52 |
| 3.3.1 PS nanoparticle synthesis with acrylic acid as comonomer. ....  | 53 |
| 3.3.2 Synthesis of amine-ended Fe <sub>3</sub> O <sub>4</sub> nanoparticles, linkage to carboxyl-ended PS beads and formation of magnetic porous hollow silica nanospheres (MPHSNs) ..... | 58 |
| 3.3.3 In-situ growth of Fe <sub>3</sub> O <sub>4</sub> nanoparticles on PS particles.....   | 60 |
| 3.3.4 Preparation of mesoporous silica nanospheres based on PS templating.....  | 61 |
| 3.3.4.1 Ethanol-only medium for silica coating on PS nanoparticle. ....   | 63 |
| 3.3.4.2 Water/ethanol mixed medium for silica coating on PS nanoparticles.....  | 66 |
| 3.3.5 Microemulsion method using PVP as stabilizer for preparation of PS beads with large yield.....  | 67 |
| 3.3.6 Mesoporous silica coating on PS nanoparticles.....  | 69 |
| 3.3.7 In-situ growth of Fe <sub>3</sub> O <sub>4</sub> nanoparticles on mesoporous silica nanospheres, synthesis and XRD study .....  | 71 |
| 3.3.8 Magnetic property of as-prepared magnetic hollow silica nanospheres. ....   | 76 |
| 3.3.9 BET analysis. ....  | 77 |
| 3.3.10 FT-IR spectrum. ....   | 79 |
| 3.3.11 Fluorescence linkage using water soluble quantum dots .....  | 79 |
| 3.4 Conclusion .....  | 80 |
| 3.5 References .....  | 81 |

## **Part II: Semiconductive nanostructure for biosensor application**

### **Chapter IV: Introduction 83**

|   |    |
|---|----|
| 4.1 Nanoparticles based biosensors .....  | 84 |
| 4.1.1 Fluorescence sensing .....  | 84 |
| 4.1.2 Colorimetric sensing .....  | 86 |
| 4.1.3 Electrochemical sensing.....  | 87 |
| 4.2 Nanowire based biosensors .....   | 88 |
| 4.2.1 Principle of nanowire field effect transistor (FET) in biosensing.....    | 88 |
| 4.2.2 Semiconductive nanowires for biosensing .....                             | 90 |
| 4.2.2.1 Indium Oxide ( $\text{In}_2\text{O}_3$ ) nanowire based biosensor ..... | 90 |
| 4.2.2.2 Zinc oxide (ZnO) nanowire based biosensor .....                         | 92 |
| 4.2.2.3 Silicon nanowire based biosensor .....                                  | 93 |
| 4.2.2.4 Conducting polymer (CP) nanowire based biosensor.....                   | 95 |
| 4.2.2.5 Others .....  | 96 |
| 4.3 References .....  | 97 |

### **Chapter V: Indium oxide nanowire based field-effect transistor for biosensing 103**

|  |     |
|--|-----|
| 5.1 Introduction.....  | 103 |
| 5.2 Experimental .....   | 104 |
| 5.3 Result and discussion.....   | 107 |
| 5.3.1 Device fabrication of $\text{In}_2\text{O}_3$ nanowire based field-effect transistor ..... | 107 |
| 5.3.1.1 $\text{In}_2\text{O}_3$ nanowire synthesis. ....   | 107 |
| 5.3.1.2 Device fabrication.....  | 109 |
| 5.3.1.3 Device measurement.....  | 110 |
| 5.3.1.4 Microfluidic channel integration.....  | 112 |
| 5.3.1.5 Preliminary detection of ricin. ....   | 112 |
| 5.3.2 Nonspecific binding of between bio-species and $\text{In}_2\text{O}_3$ nanowire.....       | 114 |
| 5.3.2.1 Engineered antibody.....   | 114 |
| 5.3.2.2 Quantification of binding efficiency between nanowire, antibody and antigen. ....        | 115 |
| 5.4 Conclusion .....   | 119 |
| 5.5 References .....   | 120 |

|  |                |
|--|----------------|
| <b>Chapter VI: Silicon nanowire based field effect transistor using top-down approach for biosensing</b> | <b>121</b>     |
| 6.1 Introduction.....  | 121            |
| 6.2 Experimental .....   | 121            |
| 6.3 Result and discussion.....   | 123            |
| 6.3.1 Device fabrication.....  | 123            |
| 6.3.2 FET property. ....   | 124            |
| 6.3.3 Design of wafer size electrode pattern.....  | 126            |
| 6.4 Conclusion .....   | 127            |
| 6.5 References.....  | 127            |
| <br><b>Appendix: Copyright and Permission</b>  | <br><b>128</b> |
| <b>Vita</b>  | <b>133</b>     |



## List of Scheme

|            |  |     |
|------------|--|-----|
| Scheme 2.1 | Rotating packed bed (RPB) reactor: (1) CO <sub>2</sub> gas inlet; (2) rotator; (3) packing; (4) distributor; (5) casing and routeway of circulating water; (6) outlet of suspension of Ca(OH) <sub>2</sub> and Fe <sub>3</sub> O <sub>4</sub> ; (7) CO <sub>2</sub> gas outlet; (8) inlet of suspension of Ca(OH) <sub>2</sub> and Fe <sub>3</sub> O <sub>4</sub> . <sup>24</sup> Reprinted with permission. Copyright 2007 American Chemical Society. | 29  |
| Scheme 2.2 | Synthesis of Magnetic Porous Hollow Silica Nanospheres (MPHSNP).   | 30  |
| Scheme 2.3 | Synthesis of Magnetic Porous Hollow Silica Nanotubes (MPHSNTs).  | 33  |
| Scheme 3.1 | Synthesis approach for magnetic porous hollow silica nanospheres using PS beads as template.   | 52  |
| Scheme 3.2 | Synthesis approach for magnetic porous hollow silica nanospheres using PS beads as template and in-situ growth of Fe <sub>3</sub> O <sub>4</sub> nanoparticles.  | 62  |
| Scheme 4.1 | Schematics showing the structure and working mechanism of nanowire FET based biosensor.  | 88  |
| Scheme 5.1 | Device fabrication procedure of In <sub>2</sub> O <sub>3</sub> nanowire field-effect transistor using bottom-up method.  | 109 |
| Scheme 6.1 | Procedure of top-down method to fabricate multiplexed silicon nanowire FET device array for biosensor.   | 123 |

## List of Figure

|             |   |    |
|-------------|---|----|
| Figure 2.1  | Fe <sub>3</sub> O <sub>4</sub> /CaCO <sub>3</sub> magnetic composite nanoparticles. (a) Bright-field TEM micrograph. The Fe <sub>3</sub> O <sub>4</sub> nanoparticles appear in darker dots embedded in the CaCO <sub>3</sub> particles. (b) The EDS spectrum of the composite particles. | 30 |
| Figure 2.2  | TEM image (a) and EDS spectrum (b) of MPHSNs. The inset is a HREM image, showing pores on the hollow silica shell.  | 31 |
| Figure 2.3  | Nitrogen absorption-desorption isotherms of MPHSNs.   | 32 |
| Figure 2.4  | Pore size distribution for the MHSNs sample calculated using BJH method.  | 32 |
| Figure 2.5  | SEM image of CaCO <sub>3</sub> nanoneedle template (a) before and (b) after the size selection process.   | 34 |
| Figure 2.6  | SEM image of MPHSNTs showing general morphology.  | 34 |
| Figure 2.7  | (a) TEM image of a MPHSNT, showing the middle region the nanotube. The size of the darker contrast magnetite nanoparticles is about 10 nm. (b) The EDS spectrum of MPHSNT.  | 35 |
| Figure 2.8  | (a) Nitrogen absorption-desorption isotherms of MPHSNTs. (b) Pore size distribution for the MPHSNTs sample calculated using BJH method.   | 36 |
| Figure 2.9  | Magnetic properties of the MHSNs: (a) temperature dependence of magnetization at ZFC and FC conditions; (b) hysteresis loops of the MHSNs at 5 and 300 K.   | 38 |
| Figure 2.10 | Magnetic properties of the MPHSNTs: (a) temperature dependence of magnetization at ZFC and FC conditions; (b) hysteresis loops of the MHSNs at 5 and 300 K.   | 38 |
| Figure 2.11 | In vitro drug release of ibuprofen from the MPHSNs showing sustained release.   | 39 |
| Figure 2.12 | In vitro drug release of ibuprofen for MPHSNTs (20 mg) with and without CTAB directed mesoporous structure. The amount of loaded drug was calculated as 1.462 mg for non-surfactant sample and 2.774 mg for CTAB modified sample.   | 40 |

|             |  |    |
|-------------|--|----|
| Figure 2.13 | CRL-2199 cell toxicity: phase microscopy. Cells were treated with control media (A+B), or with 50 $\mu\text{g/ml}$ of copper nanoparticles (C+D) or MPHSN nanoparticles (E+F). Panels A, C, and E show cultures 5 minutes after treatment and panels B, D, and F at 20 hours after treatment. The large black dot in each figure is an orientation marker to ensure that the same area or cells is monitored over time. Scale bar indicated. | 41 |
| Figure 2.14 | CRL 2020 Brain tumor cells grown at a density of 30,000 cells per ml were treated with 50 $\mu\text{g/ml}$ of silica nanotubes (D-F) or copper nanoparticles (G-I), or with Locke's solution as a control (A-C) for 4.5 hours. Phase microscopy pictures, or same areas stained with calcein or propidium iodide are indicated. Original microscope magnification= 200 x.  | 42 |
| Figure 3.1  | TEM images of PS nanoparticles synthesized with (a) 13.8 mM, (b) 34.4 mM, (c) 41.4 mM, (d) 68.8 mM of acrylic acid.  | 53 |
| Figure 3.2  | TEM images of PS nanoparticles synthesized under different nitrogen flow rate: (a) 4 sccm, (b) 1 sccm. The concentration of acrylic acid is 68.8 mM.   | 55 |
| Figure 3.3  | The polymer chain prolongation of (a) polystyrene and (b) poly(styrene-acrylic acid) showing radical polymerization mechanism.   | 56 |
| Figure 3.4  | FT-IR spectra of (a) plain PS nanoparticle and (b) PS nanoparticles with $-\text{COOH}$ functionality.   | 57 |
| Figure 3.5  | TEM images of (a) as-synthesized $\text{Fe}_3\text{O}_4$ nanoparticles with amine functionality, (b) Carboxyl group modified PS nanoparticles, (c) PS nanoparticles with $\text{Fe}_3\text{O}_4$ nanoparticles linked on surface, (d) higher magnification image of (c) showing detailed morphology.   | 58 |
| Figure 3.6  | TEM images of (a) silica coated $\text{Fe}_3\text{O}_4$ -PS nanoparticles and (b) higher magnification image of (a).   | 59 |
| Figure 3.7  | TEM images of (a) $\text{Fe}_3\text{O}_4$ nanoparticles in-situ grown on PS particles, (b) higher magnification of (a) showing surface detail of single PS particle.   | 61 |
| Figure 3.8  | TEM image of silica hollow nanospheres synthesized under ammonia concentration of (a) and (b) 0.74 M, (c) 1.11 M, (d) 1.48 M. Inserts are showing details of small silica particles. Scale bar of inserts: 20 nm.  | 64 |
| Figure 3.9  | TEM image of silica nanospheres synthesized from (a) shorter and (b) longer treatment of sonication and stirring.  | 66 |

|             |  |     |
|-------------|--|-----|
| Figure 3.10 | TEM images of mesoporous silica nanospheres from water/ethanol ratio of 1:4 v/v at (a) low and (b) high magnification.   | 67  |
| Figure 3.11 | TEM image of (a) PS nanoparticles synthesized by microemulsion method (b) PS nanoparticles achieved after reduced pressure filtration of (a).  | 68  |
| Figure 3.12 | TEM images of mesoporous hollow silica nanospheres from different TEOS/PS ratio (w/w): (a) 0.75, (b) 1.56, (c) 2.99, (d) 6.22.   | 69  |
| Figure 3.13 | TEM images of silica coated PS nanoparticle (a) before and (b) after calcination treatment for template removal.   | 70  |
| Figure 3.14 | TEM images of Fe <sub>3</sub> O <sub>4</sub> nanoparticle coated silica nanospheres in TETA with reaction time of (a) 1 hr and (b) 3 hr.   | 72  |
| Figure 3.15 | TEM images of magnetic nanoparticles from the synthesis by using (a) TEPA and (b) TEG as reaction solvent; and (c) XRD spectra of samples, from top: synthesis with TEPA, Fe standard, synthesis with TEG, Fe <sub>3</sub> O <sub>4</sub> standard.  | 73  |
| Figure 3.16 | TEM image of (a) magnetic nanoparticle decorated silica nanospheres (highlighted in red dashed circles) and (b) higher magnified image showing magnetic particles filling inside silica shell.   | 74  |
| Figure 3.17 | XRD spectrum of (a) as-prepared magnetic nanoparticles on silica and (b) Fe <sub>3</sub> O <sub>4</sub> standard.  | 75  |
| Figure 3.18 | Magnetic properties of the Fe <sub>3</sub> O <sub>4</sub> decorated silica: (a) temperature dependence of magnetization at ZFC and FC conditions; (b) hysteresis loops 300 K.  | 77  |
| Figure 3.19 | (a) Nitrogen absorption-desorption isotherms and (b) Pore size distribution calculated using BJH method of mesoporous silica nanospheres and after in-situ growth of magnetic nanoparticles.   | 78  |
| Figure 3.20 | FT-IR spectra of silica nanospheres with in-situ growth of Fe <sub>3</sub> O <sub>4</sub> nanoparticles by using (a) TEG and (b) combination of TEPA and TEG, as reaction solvent.   | 79  |
| Figure 3.21 | Fluorescence image of MPHSN linked with CdSe/ZnS quantum dots with maximum emission at 595 nm using a 40x objective lens.  | 80  |
| Figure 5.1  | (a) schematics for the synthesis of In <sub>2</sub> O <sub>3</sub> nanowires: (1) InAs precursor, (2) silicon substrate, (3) alumina crucible boat, (4) quartz test tube, (5) 2-inch furnace tube and (6) furnace heating coil, (b) SEM and (c) TEM image of as-prepared In <sub>2</sub> O <sub>3</sub> nanowires. | 108 |

|             |   |     |
|-------------|---|-----|
| Figure 5.2  | (a) SEM image of as-fabricated $\text{In}_2\text{O}_3$ NW device and (b) UV response of single NW semiconducting transistor, arrows represent the points that UV was applied.   | 110 |
| Figure 5.3  | (a) I-V curves of as fabrication $\text{In}_2\text{O}_3$ NW transistor under a series of gate voltage. (b) $I_{\text{ds}}$ (source-drain current)- $V_{\text{gs}}$ (gate-source voltage) curve under $I_{\text{ds}}=1.0$ V.   | 111 |
| Figure 5.4  | (a) Schematic of the sensor dye – polymer fluid cap assembly (b) Completely assembled dice with fluidic cap, inlet and out let tube interconnect, and FET device.   | 112 |
| Figure 5.5  | (a) Water, buffer and ricin biological responses of a typical $\text{In}_2\text{O}_3$ FET device. (b) The enlarged response curve in the blue box in (a). Ab-antibody and Ag- antigen.  | 113 |
| Figure 5.6  | (a) schematics of antibody molecule with engineered tag, (b) molecular structure of histidine, (c) theoretical arrangement of antibody, antigen and blocking agent BSA on NW during detection.  | 115 |
| Figure 5.7  | Laser confocal microscopy images of $\text{In}_2\text{O}_3$ nanowires treated with different antibody and fluorescence labeled antigen. Insert percentages are the colocalisation rate between red pixel (antigen) and dark pixel (nanowire).   | 116 |
| Figure 5.8  | Laser confocal microscopy images of $\text{In}_2\text{O}_3$ nanowires treated CHRAC or CHRAC-His antibody and fluorescence labeled ricin in different order of BSA and antibody. Inserts are average red fluorescence intensity of colocalized red and black pixels.  | 117 |
| Figure 5.9  | Laser confocal microscopy images of $\text{In}_2\text{O}_3$ nanowires treated CHRAC or CHRAC-His antibody first, and then applied with either fluorescence labeled ricin or anti-human IgG. Sample (c) and (d) are without antibody and used as control. Inserts are average red fluorescence intensity of colocalized red and black pixels with standard deviation (n=5 images taken for each sample). | 118 |
| Figure 5.10 | Slicing scan with $0.5 \mu\text{m}$ interval of single NW treated with CHRAC-His and fluorescence labeled ricin, showing the position of the bio-molecules.   | 119 |
| Figure 6.1  | SEM images of nanowire array after removing Cr mask. The width of Si NW is about 300 nm.  | 124 |
| Figure 6.2  | (a) SEM image of single silicon nanowire device, (b) Current (I)-voltage (V) curve of single silicon nanowire device.   | 124 |

|            |   |     |
|------------|---|-----|
| Figure 6.3 | Electrode pattern design of SOI wafer (a) wafer size arrangement, (b) detailed measurement on single dice, (c) size of electrode tip area for nanowire fabrication. | 125 |
| Figure 6.4 | Surface modification of silicon nanowire FET device using APTES.  | 126 |
| Figure 6.5 | Surface modifications for selective detection, showing simultaneous multiplex detection.  | 127 |

## **List of Table**

|           |  |    |
|-----------|--|----|
| Table 2.1 | BET surface area and pore texture parameters of the MPHSNs.  | 32 |
| Table 2.2 | BET surface area and pore texture parameters of the MPHSNTs. | 35 |

## Abstract

The idea of utilizing nanomaterials in bio-related applications has been extensively practiced during the recent decades. Magnetic nanoparticles (MPs), especially superparamagnetic iron oxide nanoparticles have been demonstrated as promising candidates for biomedicine. A protective coating process with biocompatible materials is commonly performed on MPs to further enhance their colloidal and chemical stability in the physiological environment. Mesoporous hollow silica is another class of important nanomaterials that are extensively studied in drug delivery area for their ability to carry significant amount of guest molecules and release in a controlled manner.

In this study, different synthetic approaches that are able to produce hybrid nanomaterials, constituting both mesoporous hollow silica and magnetite nanoparticles, are described. In a two-step approach, pre-synthesized magnetite nanoparticles are either covalently conjugated to the surface of polystyrene beads and coated with silica or embedded/enclosed in the porous shell during a nanosized  $\text{CaCO}_3$  templated condensation of silica precursors, followed by acid dissolution to generate the hollow structure. It was demonstrated that the hollow interior is able to load large amount of hydrophobic drugs such as ibuprofen while the mesoporous shell is capable of prolonged drug. In order to simplify the fabrication procedure, a novel in-situ method is developed to coat silica surface with magnetite nanoparticles. By refluxing the iron precursor with mesoporous hollow silica nanospheres in polyamine/polyalcohol mixed media, one is able to directly form a high density layer of magnetite nanoparticles on silica surface during the synthesis, leaving reactive amine groups for further surface functionalization such as fluorescence conjugation. This approach provides a convenient synthesis for silica nanostructures with promising potential for drug delivery and multimodal imaging.

In addition to nanoparticles, nanowires also benefit the research and development of instruments in clinical diagnosis. Semiconductive nanowires have demonstrated their advantage in the fabrication of lab-on-a-chip devices to detect many charge carrying molecules such as antibody and DNA. In our study,  $\text{In}_2\text{O}_3$  and silicon nanowire based field effect transistors were fabricated through bottom-up and top-down approaches, respectively, for ultrasensitive bio-detection of toxins such as ricin. The specific binding and non-specific interaction of nanowires with antibodies were also investigated.

Mesoporous hollow silica, Magnetic nanoparticle, Drug delivery, Field-effect transistor biosensor,  $\text{In}_2\text{O}_3$  nanowire, Silicon nanowire.



# **Part One: Magnetic Hollow Mesoporous Silica Nanostructures for Bio-medicine Application**

## **Chapter I: Introduction**

Amorphous silica material has been widely exploited in various applications such as adsorption and separation of impurity, catalysis and drug delivery. Nanosized mesoporous silica structures feature in many outstanding advantages in the field of bio-medicine and bio-engineering including bio-compatibility, low toxicity, highly designable morphology and large surface area providing excellent platform for drug loading and modification of further functionalities. Uniform mesoporous silica particles are usually obtained by ordered self assembly of surfactant molecules integrated with silica precursors. Subsequently, methods such as soft/hard template and selective etching are fast developing techniques for synthesizing mesoporous silica with hollow interior which has been demonstrated to be more efficient for drug loading due to increased surface area and nanochannels connecting exterior and interior surface.<sup>1</sup> Based on the foundation of mesoporous silica, decoration with superparamagnetic iron oxide nanoparticles (SPION) is one of the most popular research concentrations for the purpose of targeted drug delivery, MRI contrast enhancement, hyperthermia treatment and other potential biomedicine applications. Furthermore, by combining with features like fluorescence, plasmonic resonance and targeting biological molecules conjugation, numerous designs of multi-functional silica nanostructure have been reported to achieve the best platform for targeted imaging and drug delivery in the diagnosis and treatment for infection, cancer and genetic diseases.

In this chapter, a review of several representative categories of mesoporous silica nanostructures with and without hollow interior is provided. Then various approaches of

attaching or integrating SPION to silica nanoparticles, either in the core area, embedded in the shell or conjugated on surface, are introduced. At last, further particle engineering modifications to achieve multifunctional particle for different biomedicine applications will be discussed, such as simple trigger drug release and fluorescence imaging.

### **1.1 Synthesis of uniform mesoporous silica nanoparticles (MSN)**

The first reported ordered MSN was MCM-41 (Mobil Composition of Matter No. 41) prepared through liquid crystal template method by Mobil R&D in 1992.<sup>2</sup> Ever since then, the synthesis of MSN with controllable morphology and potential functionalization has been drawing extensive attention through decades. Generally speaking, MSN materials are synthesized from the self-assembly of surfactants which serve as structure-directing template, followed by the hydrolysis and condensation of silica precursor with opposite charge around the surfactants.<sup>3</sup> Based on abundant available selection of surfactants and silica precursors with nature better understood, and fine adjustment of pH and solvents, a great variety of MSN with different pore size, pore structure and arrangement, as well as particle size and shape has been prepared. Several kinds of MSN with pore diameter from 1 to tens of nanometer are deeply involved in bio-medicine applications, such as MCM, TUD (Technische Universit ä Delft), SBA (Santa Barbara Amorphous), and so on.

As mentioned before, MCM-41 was the earliest synthesized, and also the most widely studied MSN. By using cetyltrimethylammonium bromide (CTAB) as templating surfactant, tetraethyl orthosilicate (TEOS) or sodium metasilicate ( $\text{Na}_2\text{SiO}_3$ ) as precursor which hydrolyses under the catalysis of alkaline, uniform mesopores in hexagonal arrangement with tunable pore size between 1.6-10 nm was obtained. During the synthesis in polar solvent, the amphiphilic

CTAB molecules would form micelles in the shape of spherical, rod-like or 2-D alignment under a concentration higher than a critical value (critical micelle concentration, CMC), and then condensation of silica precursors occurs around the polar head of the surfactant to form silica after hydrolysis. Surfactant template can be easily removed through either calcinations or solvent extraction, and the mesoporous silica is finally obtained.<sup>2,4</sup>

SBA-15 is another popular MSN material that has been widely introduced for application such as catalysis and drug delivery. It was originally prepared through a triblock copolymer consisting of poly(ethylene oxide)-poly(propylene oxide)-poly(ethylene oxide) (PEO-PPO-PEO) as structure-directing template in acidic media. Investigations of using different ratio between EO and PO, silica precursors (tetraethoxysilane (TEOS), tetramethoxysilane (TMOS), tetrapropoxysilane (TPOS)), inorganic acid and pH were conducted, resulting larger tunable pore sizes up to 30 nm and thicker wall. Furthermore, while the template removal can be completed by either calcinations or solvent extraction, the latter one allows the triblock polymer to be recovered for reuse.<sup>5,6</sup> However, due to the nature of polymeric template, SBA-15 particles is restricted to only relatively larger size and rigid structure, which significantly limit the potential for *in vivo* drug delivery application.<sup>1</sup>

Different from MCM and SBA, TUD-1 is a three-dimensional disordered, sponge-like mesoporous silica network structure synthesized from hydrolysis of TEOS with organic base tetraethylammonium hydroxide (TEAOH) and triethanolamine (TEA). Mesoporous silica was achieved by simple aggregation of the molecules without introducing surfactant template, and the pore size can be tunable between 2.5 nm to 25nm. The randomly arranged mesopores and large pore volume provide high accessibility for drug molecules and exhibit higher drug loading efficiency and rapid initial release (60% in 15 min for ibuprofen) by comparing with MCM-41.

However, due to lack of surfactant directed micelle formation, the morphology of TUD-1 stays in amorphous instead of homogeneous nanoparticle or nanorod and less designable, which prevents it from *in vivo* application in bio-medicine.<sup>7,8</sup>

## **1.2 Synthesis of hollow mesoporous silica nanoparticles**

In the recent decade, hollow mesoporous silica nanoparticle (HMSN) with void interior space and improved surface area has been drawing extensive attention. Comparing to conventional uniform MSN, the hollow interior that is easily accessible by diffusion of drug molecules through well ordered mesopores channels from exterior surface provides additional mesoporous surface for drug adsorption. Therefore the whole HMSN act as a capsule for drug molecules storage and the drug release is also controllable in two stages due to relatively rapid initial release from outer surface adsorption and slower permeation from inner void through cavities. So far, HMSN can be obtained by using either sacrificial templates in core area or selective etching inner layer of silica.<sup>1,3</sup>

### **1.2.1 Hard template method for synthesizing HMSN**

Hard template method can be described as using pre-prepared nanoparticle in sol-gel process to direct the self-assembly of surfactant and lead the condensation of silica precursor only happens on around surface of the template material, and hollow interior can be achieved after template removal by calcination and/or solvent extract. The size of HMSN is mainly predetermined by the diameter of the template, and the thickness of silica shell can be tuned by adjusting the ration between template, surfactant and precursor. Various nanoparticle materials

with features such as good dispersity, homogeneous size, easy synthesis and low cost have been selected as the sacrificial template.

Polystyrene (PS) nanoparticle is the most widely used hard template for HMSN synthesis. The preparation of monodispersed PS latex is a well established technique through microemulsion or emulsifier-free process within oil-in-water system with monomer styrene and polymerization inducer like potassium persulfate ( $K_2S_2O_8$ ). So far the available particle size varies from several nanometers to microns, which provides large selection for synthesis of HMSN with different diameter. Also, the functionalization of PS particles can be completed by blending in other comonomers such as acrylic acid, or functional surfactant sodium dodecyl sulfate (SDS) during the polymerization of styrene to achieve functionalities of amine, carboxyl, thiol, sulfate and so on, in order to further improve monodispersity and stability of the particles.<sup>9-12</sup> The process of silica coating on PS is usually carried out in the mixed media of ethanol and water under ammonia catalysis, the template removal can be achieved by calcination or solvent extraction using toluene, chloroform and dichloromethane.<sup>13-15</sup>

Several other nanosized organic compounds have also been applied for templating the formation of hollow silica structure. Solid lipid nanoparticles (SLN) has been demonstrated to be a promising material for hydrophobic drug delivery due to the advantage of facile synthesis, easy drug loading, low toxicity, highly bio-compatibility and bio-degradability.<sup>16</sup> HMSN prepared from cetylpalmitate SLN was obtained with size around 500 nm and present promising potential in pharmaceutics applications.<sup>17</sup> In addition, recently polysaccharide materials such as cellulose<sup>18</sup> and chitosan<sup>19</sup> are also reported as the template for HMSN synthesis.

Among inorganic materials, hematite ( $Fe_2O_3$ ) has also been used for the synthesis of HMSN. Spherical and spindle shaped hematite was first prepared from ferric chloride in low acidic

aqueous solution.<sup>20,21</sup> In water/isopropyl alcohol mixed media and catalysis of ammonia, different amount of precursor TEOS and surfactant n-octadecyl-trimethoxysilane (C18TMS) mixture with fixed molar ratio was then applied to obtain silica shell thickness from 8 to 30 nm, followed by acid etching to remove hematite.<sup>22</sup> Also, calcium carbonate ( $\text{CaCO}_3$ ) nanoparticles and nanoneedles prepared from industrial apparatus have been chosen as the template to synthesize hollow mesoporous silica nanospheres and nanotubes, respectively.<sup>23,24</sup> In addition, CTAB modified PbS nanocubes with good monodispersity was employed for the synthesis of mesoporous silica nanocages.<sup>25</sup>

### **1.2.2 Soft template method for synthesizing HMSN**

Soft template method is based on using multiple surfactants or oil/water phase different to form a water or organic droplet in the core area and then the condensation of silica precursor would happen on the surface to form silica shell. It is usually a one-pot procedure without a separated step for template preparation. One approach to soft template synthesis is co-templating which employs more than one layer of surfactant formed self-assembly to build vesicle in the core. A cationic-anionic-neutral block copolymer ternary surfactant system was studied to achieve HMSN. Aqueous solutions of cationic surfactant CTAB and anionic SDS were first mixed together to form dual-surfactant micelles with water droplets in it. Then tri-block copolymer Pluronic P123 ( $\text{EO}_{20}\text{PO}_{70}\text{EO}_{20}$ ) worked as outer layer surfactant to anchor on the micelle surface, direct the formation mesoporous silica shell and prevent aggregation in slightly acidic condition. After template removal by calcination, the resulted HMSN present diameter between 100 to 500 nm with permeable shell and uniform pore size around 5 nm.<sup>26</sup> In another reported study, poly(vinylpyrrolidone) (PVP) was chosen as the core template to synthesize

HMSN with CTAB directed mesopores. The product is uniform in diameter with smaller pore size of 2.67 nm in hexagonal arrangement, and was demonstrated to be a promising material for controlled drug release.<sup>27</sup>

Oil-in-water (O/W) and water-in-oil (W/O) microemulsion is another synthesis approach to soft template by dispersing one solvent (dispersed phase) in another (continuous phase) with totally opposite hydrophilicity under the assistant of surfactant to form homogeneous droplets as template. *N,N* -dimethylformamide (DMF) has been reported to be the dispersed phase of the O/W synthesis and the inner size of HMSN with radially orientated mesopores can be precisely adjusted by changing the ratio of DMF/water.<sup>28</sup> In the W/O reversed microemulsion, HMSN with the size from 20 nm to several micron can be prepared by dispersing small amount of aqueous solution in cyclohexane with low polarity surfactants like Triton-100 and Igepal CO-520.<sup>29-32</sup> Based on traditional water-oil microemulsion, recently an oil-in-DEG (diethylene glycol) synthesis was developed. Using DEG instead of water can strictly limit the hydrolysis and condensation of silica precursor within the oil droplets, providing better control of particle size and prevent agglomeration.<sup>33,34</sup>

### **1.2.3 Selective etching for synthesizing HMSN**

Pure silica and other silica-organic composite network present different structure and degree of crosslinking from the condensation of silica precursors. Therefore, their stability against various etching agent, pH or temperature is also different, which provides the platform for designing multiple layers core/shell structure within one single nanoparticle in order to achieve hollow or rattle type silica by applying selective etching on designated layer(s).<sup>35-37</sup> For example, Stöber method is the most widely conducted method for the fabrication of solid silica. But

recently, it was demonstrated that the outer layer of Stober silica exhibit much higher density and degree of crosslinking comparing to innermost part of the silica particle. Studies show that the inner silica part can be etched by either simple hot water treatment of 90 °C for 30 min or hydrothermal process in acidic condition to obtain hollow silica structure.<sup>38,39</sup> Also, the surface of silica can be protected by applying surfactants such as PVP against alkaline etching, resulting in mesoporous silica shell with void interior.<sup>40</sup> And the etching process can be controlled by the concentration of etchant and reaction time. Similarly, another strategy is to apply a secondary surfactant assisted silica coating with controllable thickness on solid silica nanoparticle and only the core area is removed after alkaline etching due to the structural difference.<sup>41,42</sup>

### **1.3 Introducing superparamagnetic iron oxide nanoparticles (SPION) to mesoporous silica nanoparticle (MSN)**

SPION, mainly magnetite ( $\text{Fe}_3\text{O}_4$ ) and maghemite ( $\gamma\text{-Fe}_2\text{O}_3$ ), is an important inorganic material that can be synthesized by several well established wet chemistry approaches including hydrothermal, co-precipitation, microemulsion and thermal decomposition.<sup>43</sup> The superparamagnetism property possesses zero coercivity which allows the particle to move towards and stay at desired area under existence of external magnetic field and be able to move freely once the magnetic field is removed, and is a significant advantage for applications targeted drug delivery, MRI contrast enhancement, and hyperthermia therapy for the treatment of numerous diseases including infections and tumor. While MSN is an ideal drug carrier candidate with good bio-compatibility, numerous studies are concentrated on the integration of these two materials in different morphologies and strategies. While the most direct combination of SPION and MSN is through covalent linkage using surface modified silica and ligand-capped



magnetic nanoparticles, but always suffers from low crosslinking efficiency, complicated preparation of both materials and ligand exchange process of magnetic particle.<sup>44</sup> During the past decade, various pathways for facile and convenient production of magnetic mesoporous silica nanostructures have been developed.<sup>3</sup>

### **1.3.1 SPION/MSN core/shell structure**

Securing SPION in the core area by covering with mesoporous silica shell can effectively protect the iron oxide from biological environment and therefore prevent bio-degradation. Originally, oleic acid capped SPIONs with homogeneous size, good crystalline structure and hydrophobic property is the most commonly achieved SPION through a scalable synthesis.<sup>45</sup> The SPION is first dispersed in chloroform or hexane then introduced to aqueous solution of surfactant for mesoporous silica coating through oil-in-water microemulsion mechanism. Here the surfactant here is a dual-function agent for both stabilization of SPION and mesoporous directing template, and the resulted structure can be either strict SPION/MSN core/shell<sup>46-50</sup> or SPION embedded in MSN framework in a scattered manner.<sup>51,52</sup> Within the same process, other hydrophobic nanoparticles with different characteristics such as quantum dots<sup>52</sup> can also be capsule together with SPION to obtain multi-functional drug carrier.

In an alternative approach, single SPION (<20 nm) or polycrystalline SPIONs which are usually assembled in larger size (>100 nm) from small SPIONs, are prepared in good mono-dispersion and only one can be trapped within each mesoporous silica shell after the sol-gel process with adjustable thickness. The hydrophobicity of as-prepared SPION can be converted by modification with surfactant for stabilization immediately prior to sol-gel mesoporous silica coating.<sup>53,54</sup> It has been frequently reported that hydrothermally prepared SPION core from

diethylene glycol reaction media with diameter above 100 nm was introduced to a two-step silica coating process, resulting in a sandwich structure. A thin nonporous silica coating was first applied to totally conceal the SPION and improve hydrophilicity and stability, followed by a surfactant directed mesoporous shell formation for adsorption of drug molecules.<sup>55-59</sup> In these studies, perpendicular aligned mesopores can usually be achieved, providing nanosized channels for mass storage and transfer in drug delivery and controlled release. Furthermore, since silica provide easier surface modification and better reactive group availability than SPION, conjugations of other functionalities such as gold nanoparticles<sup>56,58</sup> and fluorescence<sup>57</sup> are always introduced between the two silica coating procedures to achieve better efficiency, as well as remain protected by the secondary silica coating.

### **1.3.2 SPION embedded in MSN framework**

Different from encapsulating pre-prepared SPIONs with mesoporous silica shell under the assistant of surfactants, magnetic nanoparticles can be in-situ impregnated in the porous framework, started by immersing MSN in solution of iron oxide precursors. Sol-gel synthesis is one frequently applied technique based on the thermal decomposition of organic iron precursor. Generally,  $\text{Fe}(\text{acac})_3$  (iron(III) acetylacetonate) is first dissolved completely in acidic aqueous solution to form a sol. Then MSN is then added to the system under vigorous stirring for hours then dried, followed by high temperature treatment (500 °C) to yield grain-like magnetic iron oxide. The method has been successfully applied to SBA and MCM silica with well ordered mesopores and mainly resulted in  $\gamma\text{-Fe}_2\text{O}_3$ .<sup>60,61</sup> In addition, spherical mesoporous silica nanoparticles with size ranging between 0.3-3  $\mu\text{m}$  and an average pore diameter of 4.6 nm was also used to achieve  $\gamma\text{-Fe}_2\text{O}_3$  nanoparticles of 5 nm diameter embedded in the mesopores.<sup>62</sup>

Another method is to use  $\text{Fe}(\text{NO}_3)_3$  as the iron precursor that is easier to penetrate through mesopores channels due to smaller ion size and better solubility. The obtained hematite nanoparticles can be further reduced to  $\text{Fe}_3\text{O}_4$  by either heating under  $\text{H}_2$  or  $\text{NaBH}_4$  reduction in solution.<sup>63-65</sup> This in-situ growth of SPION provides facile integration in mesoporous silica and protection against bio-degradation, leaving sufficient pore volume and surface area for further matter storage as drug carrier.

### **1.3.3 Rattle type SPION core in MSN shell**

During the recent years, rattle type core/shell structure has been a popular approach for combining SPION with mesoporous silica nanospheres. With cavity between SPION core and silica shell, these magnetic silica nanorattles possess significant advantages of both strong magnetization, as well as increased surface area and sustained release performance of drug molecules provided from hollow silica nanospheres. The first reported magnetic nanorattles synthesis was based on the mechanism of selective etching to achieve hollow mesoporous silica. Hematite core with a diameter around 100 nm was first subjected to a solid layer of silica coating with desired thickness, followed by a surfactant incorporated mesoporous silica coating on outside. The sample was then introduced to hydrothermal treatment to selectively etch away the solid silica layer while the mesoporous layer remains protected by surfactant, leaving the cavity structure. At last the surfactant was removed by calcination, followed by hydrogen reduction of the hematite to yield magnetite.<sup>66,67</sup> Later on, triblock copolymer  $(\text{EO})_{106}(\text{PO})_{70}(\text{EO})_{106}$  (denoted as F127) was selected as the template for building the cavity instead of solid silica. The core material, not limited to magnetic particle, was first stabilized by the copolymer and surfactant through electrostatic interaction and synergetic effect to form a core-vesicle complex. Then the

deposition of mesoporous silica was directed by the vesicle templating through sol-gel polymerization of TEOS. After the hydrolysis and condensation of TEOS which caused shrinkage of silica shell, the cavity of nanorattles was obtained.<sup>68</sup>

Another approach to nanorattles structure is to employ a composite sacrificial template in the core area. Colloidal carbon spheres of 800 nm diameter with adsorbed iron precursor on surface were first prepared by hydrothermal treatment of glucose with  $\text{FeCl}_3$ , then subject to sol-gel mesoporous silica coating. Hematite was originally obtained after the calcination treatment for carbon template removal, and then converted to magnetite under hydrogen reduction. It was observed that the hematite nanoparticles were initially formed at the surface of carbon spheres, then aggregated after calcination and resulted in polycrystalline cluster with diameter within 100 nm. Therefore, with this size shrinkage of core material from 800 to 100 nm during carbon removal, a large cavity was achieved.<sup>69-71</sup>

#### **1.4 Further functionalization and applications of SPION/MSN**

Founded on the combination nanostructures of SPION and MSN which provides significant advantages in both physical and chemical aspects, including superparamagnetism, large surface area with mesopores, low toxicity and chemically modifiable surface, numerous studies have been carried out to explore potential application in bio-medicine field. An interesting observation revealed that magnetic silica nanoparticles that are cellular internalized are able to drive the suspended cells to move towards a magnet, suggesting good magnetic targeting ability.<sup>72</sup> SPION/MSN nanomaterial with further functionalization has been demonstrated to be a promising candidate for drug/gene delivery carriers and fluorescence imaging agents.<sup>73</sup>

### 1.4.1 Drug/gene delivery

It is widely admitted that mesoporous silica possesses large surface area and pore volume and makes it a preferred candidate for high efficiency drug loading by simply immersed in solution and continuous releasing in physiological environment.<sup>49</sup> Many drugs with poor water solubility have been explored to demonstrate this concept, including ibuprofen,<sup>61,74</sup> doxorubicin,<sup>75</sup> docetaxel,<sup>67</sup> and so on. Obvious sustained release can be achieved by comparing with the behavior of solid silica nanostructures or pure drug pellets.<sup>3</sup> And amino group functionalized silica can be applied for gene delivery by absorbing oligonucleotide through electronic interaction to reach into tumor cell.<sup>76</sup>

Other than physical absorption, many groups have been focusing on designing the covalent binding between drug molecules and silica surface that can be manipulated through external condition control. For example, doxorubicin (DOX) has been a model drug for the study of drug delivery carrier because of its anti-cancer effect and strong fluorescence emission property which enables the localization and imaging functions.<sup>77</sup> pH triggered release of DOX has been reported by using 1,2-cyclohexanedicarboxylic anhydride as a crosslinker. The conjugation efficiency of DOX silica is considerably high (>10% w/w) and the drug remains stable in neutral pH 7.4, but occurs rapid initial release under pH 5 and remains sustainable in days.<sup>78</sup>

In controlled drug delivery, the function of SPION is not limited to providing magnetic property, but also concealing the load drug molecules in the porous structure as a cap and releasing upon external stimulus. A recent study has reported that SPION was first covalently conjugated on surface of MCM-41 silica after loading anticancer drug in mesopores, and then was detached from silica surface due to cleavage of covalent bonds under stimulus of magnetic field. It was discovered that there was neglectable amount of drug release without magnetic

stimulus, and the number of SPION detached, exposed silica surface and drug release rate can be precisely controlled by the time duration of magnetic field exposure.<sup>79</sup> In another strategy, pH sensitive association/dissociation of SPION on silica was also exploited. Carboxybenzaldehyde functionalized SPIONs are able to closely bind to tri(aminomethyl)ethane (TAE) functionalized silica through non-covalent interaction in neutral pH as nanocap of the mesopores, and detach in acidic condition in endosome (pH 5).<sup>80</sup> The hybridization between complementary ssDNA strands that conjugated on silica and SPION respectively has also been employed for thermal responsive release as the dissociation happens at temperature above 42 °C, and the process is reversible. Coupling this response together with hyperthermia effect of SPION would achieve an optimized controllable release strategy.<sup>81</sup> Other environmental responsive reactions that has been reported includes boronate esters linkage for pH response,<sup>82</sup> disulfide linkage for redox response,<sup>83</sup>

Thermal responsive polymers, for example, poly(ethyleneimine)-b-poly(N-isopropylacrylamide) (PEI/NIPAM) that has dissociable bond at 35-40 °C, are frequently employed as the modification of mesoporous silica. After drug molecules entering the porous structure, the polymer attached on silica surface acts as a temperature-responsive gatekeeper for loaded drug, and also retains other larger molecules such as therapeutic proteins within the polymer shell through electrostatic force or hydrogen bond to achieve a multi-drug carrier.<sup>84</sup> Other polymers, poly(N-isopropylacrylamide-co-methacrylic acid) (P(NIPAM-co-MAA))<sup>85</sup> and P(NIPAM-co-NHMA) (NHMA: N-hydroxymethyl acrylamide)<sup>46</sup> can be also introduced to achieve a thermo/pH dual-responsive release on silica shell. Besides polymer shell assembly, conjugation of functional organic molecule or inorganic nanocaps to guard the mesopores was

also studied to achieve triggered release promoted by various kind of stimulation, includes photo-responsive,<sup>86,87</sup> redox responsive<sup>86,88</sup>, pH responsive<sup>89-92</sup> and enzyme response.<sup>93</sup>

#### 1.4.2 Fluorescence imaging

Fluorescence dye incorporated silica that coupled with conjugations targeting molecules such as folic acid, aptamer and antibody has been extensively reported for the purpose of bio-imaging. Dye molecule can be attached to silica surface by covalent binding to achieve water-dispersible, stable, and biocompatible product.<sup>94,95</sup> However, due to the potential degradation of the binding and toxicity of the dye, an alternative approach became more popular: dye molecules can be easily doped into silica matrix by conjugating to silica precursor prior to the synthesis of silica nanoparticles. Due to the instant covalent bond formation between isothiocyanate and amine groups, Rhodamine B isothiocyanate (RITC) and fluorescein isothiocyanate (FITC) can first link to 3-aminopropyltriethoxysilane (APTES) as part of silica resource, and then introduced to the silica formation with other precursor such as TEOS. This doping technique ensures the stability of dye molecules and minimizes degradation and diffusion into physiological environment. In vitro cellular imaging generated by the doped dye helps to track and understand the cellular uptake of the nanoparticles, including intracellular location, concentration and accumulation through time.<sup>44,53,96,97</sup>

As another fluorescence resource, semiconductive nanocrystals quantum dots possess unique advantages such as single excitation, narrow and tunable emission spectrum, strong and stable fluorescence intensity.<sup>98</sup> And quantum dots integrated silica nanoparticles through different pathways such as surface covalent linkage<sup>99</sup> and enclosed as composite,<sup>100-102</sup> has been widely applied for both *in vitro* and *in vivo* fluorescence imaging.<sup>103</sup> In addition, the combination of

quantum dots and silica can also be accomplished by using the spontaneous assembly between a positively charged polymer such as polyelectrolyte (PAH) and negatively charged fluorescent quantum dots (QDs) to form a composite shell onto silica surface.<sup>104</sup>

Besides organic dye and quantum dots, lanthanide ion compounds also have unique luminescence properties, such as sharp emission lines, long lifetimes, good photostability, and effective elimination of short-lived scattering light and background noises.<sup>105-107</sup> It was demonstrated that by conjugating the organic chromophore, chelation agent and silane precursor together as part of the resource and woven into silica nanoparticle during synthesis, terbium ( $\text{Tb}^{3+}$ ) can be successfully dope into silica network with good stability.<sup>105</sup>

## 1.5 References

- (1) Tang, F.; Li, L.; Chen, D. *Adv. Mater.* **2012**, *24*, 1504.
- (2) Beck, J. S.; Vartuli, J. C.; Roth, W. J.; Leonowicz, M. E.; Kresge, C. T.; Schmitt, K. D.; Chu, C. T. W.; Olson, D. H.; Sheppard, E. W. *J. Am. Chem. Soc.* **1992**, *114*, 10834.
- (3) Yang, P.; Gai, S.; Lin, J. *Chem. Soc. Rev.* **2012**, *41*, 3679.
- (4) Kresge, C. T.; Leonowicz, M. E.; Roth, W. J.; Vartuli, J. C.; Beck, J. S. *Nature* **1992**, *359*, 710.
- (5) Zhao, D.; Feng, J.; Huo, Q.; Melosh, N.; Fredrickson, G. H.; Chmelka, B. F.; Stucky, G. D. *Science* **1998**, *279*, 548.
- (6) Ji, X.; Lee, K. T.; Monjauze, M.; Nazar, L. F. *Chem. Commun.* **2008**, 4288.
- (7) Heikkilä T.; Salonen, J.; Tuura, J.; Hamdy, M. S.; Mul, G.; Kumar, N.; Salmi, T.; Murzin, D. Y.; Laitinen, L.; Kaukonen, A. M.; Hirvonen, J.; Lehto, V. P. *Int. J. Pharm.* **2007**, *331*, 133.
- (8) Jansen, J. C.; Shan, Z.; Marchese, L.; Zhou, W.; Puil, N. v. d.; Maschmeyer, T. *Chem. Commun.* **2001**, 713.
- (9) Chang, C. H.; Son, P. S.; Yoon, J.-A.; Choi, S.-H. *J. Nanomaterials* **2010**, *2010*, 1.
- (10) Hsiao, S.-C.; Ou, J.-L.; Sung, Y.; Chang, C.-P.; Ger, M.-D. *Colloid & Polymer Science* **2010**, *288*, 787.
- (11) Dong, H.; Lee, S.-Y.; Yi, G.-R. *Macromolecular Research* **2009**, *17*, 397.
- (12) Goodwin, J. W.; Hearn, J.; Ho, C. C.; Ottewill, R. H. *Colloid & Polymer Science* **1974**, *252*, 464.
- (13) Qi, G.; Wang, Y.; Estevez, L.; Switzer, A. K.; Duan, X.; Yang, X.; Giannelis, E. P. *Chem. Mater.* **2010**, *22*, 2693.
- (14) Hu, H.; Zhou, H.; Du, J.; Wang, Z.; An, L.; Yang, H.; Li, F.; Wu, H.; Yang, S. *J. Mater. Chem.* **2011**, *21*, 6576.



- (15) Cao, S.; Jin, X.; Yuan, X.; Wu, W.; Hu, J.; Sheng, W. *J. Polym. Sci., Part A: Polym. Chem.* **2010**, *48*, 1332.
- (16) Müller, R. H.; Mäder, K.; Gohla, S. *European Journal of Pharmaceutics and Biopharmaceutics* **2000**, *50*, 161.
- (17) Pasc, A.; Blin, J.-L.; Stebe, M.-J.; Ghanbaja, J. *RSC Advances* **2011**, *1*, 1204.
- (18) Guangshuai, F.; Aijian, H.; Yongcan, J.; Qiang, C.; Junlong, S. *BioResources* **2012**, *7*, 2319.
- (19) Tsai, M.-S.; Li, M. J. *J. Non-Cryst. Solids* **2006**, *352*, 2829.
- (20) Matijevic, E. *Annu. Rev. Mater. Sci.* **1985**, *15*, 483.
- (21) Ozaki, M.; Kratochvil, S.; Matijević, E. *J. Colloid Interface Sci.* **1984**, *102*, 146.
- (22) Zhao, W.; Lang, M.; Li, Y.; Li, L.; Shi, J. *J. Mater. Chem.* **2009**, *19*, 2778.
- (23) Zhou, W.; Gao, P.; Shao, L.; Caruntu, D.; Yu, M.; Chen, J.; O'Connor, C. J. *Nanomedicine: Nanotechnology, Biology and Medicine* **2005**, *1*, 233.
- (24) Zhou, J.; Wu, W.; Caruntu, D.; Yu, M. H.; Martin, A.; Chen, J. F.; O'Connor, C. J.; Zhou, W. L. *J. Phys. Chem. C* **2007**, *111*, 17473.
- (25) Wang, T.; Chai, F.; Fu, Q.; Zhang, L.; Liu, H.; Li, L.; Liao, Y.; Su, Z.; Wang, C.; Duan, B.; Ren, D. *J. Mater. Chem.* **2011**, *21*, 5299.
- (26) Yeh, Y.-Q.; Chen, B.-C.; Lin, H.-P.; Tang, C.-Y. *Langmuir* **2005**, *22*, 6.
- (27) Yufang, Z.; Jianlin, S.; Weihua, S.; Hangrong, C.; Xiaoping, D.; Meilin, R. *Nanotechnology* **2005**, *16*, 2633.
- (28) Li, J.; Liu, J.; Wang, D.; Guo, R.; Li, X.; Qi, W. *Langmuir* **2010**, *26*, 12267.
- (29) Teng, F.; Tian, Z.; Xiong, G.; Xu, Z. *Catal. Today* **2004**, *93–95*, 651.
- (30) Lin, Y.-S.; Wu, S.-H.; Tseng, C.-T.; Hung, Y.; Chang, C.; Mou, C.-Y. *Chem. Commun.* **2009**, 3542.
- (31) Park, S.-J.; Kim, Y.-J.; Park, S.-J. *Langmuir* **2008**, *24*, 12134.
- (32) Wu, S.-H.; Tseng, C.-T.; Lin, Y.-S.; Lin, C.-H.; Hung, Y.; Mou, C.-Y. *J. Mater. Chem.* **2011**, *21*, 789.
- (33) Li, L.; Choo, E. S. G.; Yi, J.; Ding, J.; Tang, X.; Xue, J. *Chem. Mater.* **2008**, *20*, 6292.
- (34) Li, L.; Choo, E. S. G.; Tang, X.; Ding, J.; Xue, J. *Chem. Commun.* **2009**, 938.
- (35) Loy, D. A.; Shea, K. J. *Chem. Rev.* **1995**, *95*, 1431.
- (36) Yang, Y.; Liu, J.; Li, X.; Liu, X.; Yang, Q. *Chem. Mater.* **2011**, *23*, 3676.
- (37) Roca, M.; Haes, A. J. *J. Am. Chem. Soc.* **2008**, *130*, 14273.
- (38) Yu, Q.; Wang, P.; Hu, S.; Hui, J.; Zhuang, J.; Wang, X. *Langmuir* **2011**, *27*, 7185.
- (39) Wong, Y. J.; Zhu, L.; Teo, W. S.; Tan, Y. W.; Yang, Y.; Wang, C.; Chen, H. *J. Am. Chem. Soc.* **2011**, *133*, 11422.
- (40) Zhang, Q.; Zhang, T.; Ge, J.; Yin, Y. *Nano Lett.* **2008**, *8*, 2867.
- (41) Zhang, K.; Chen, H.; Zheng, Y.; Chen, Y.; Ma, M.; Wang, X.; Wang, L.; Zeng, D.; Shi, J. *J. Mater. Chem.* **2012**, *22*, 12553.
- (42) Chen, Y.; Chen, H.; Guo, L.; He, Q.; Chen, F.; Zhou, J.; Feng, J.; Shi, J. *ACS Nano* **2009**, *4*, 529.
- (43) Lu, A.-H.; Salabas, E. L.; Schüth, F. *Angew. Chem. Int. Ed.* **2007**, *46*, 1222.
- (44) Lee, J. E.; Lee, N.; Kim, H.; Kim, J.; Choi, S. H.; Kim, J. H.; Kim, T.; Song, I. C.; Park, S. P.; Moon, W. K.; Hyeon, T. *J. Am. Chem. Soc.* **2009**, *132*, 552.
- (45) Park, J.; An, K.; Hwang, Y.; Park, J.-G.; Noh, H.-J.; Kim, J.-Y.; Park, J.-H.; Hwang, N.-M.; Hyeon, T. *Nat Mater* **2004**, *3*, 891.
- (46) Liu, C.; Guo, J.; Yang, W.; Hu, J.; Wang, C.; Fu, S. *J. Mater. Chem.* **2009**, *19*, 4764.

- (47) Liong, M.; Lu, J.; Kovochich, M.; Xia, T.; Ruehm, S. G.; Nel, A. E.; Tamanoi, F.; Zink, J. I. *ACS Nano* **2008**, 2, 889.
- (48) Feng, J.; Song, S.-Y.; Deng, R.-P.; Fan, W.-Q.; Zhang, H.-J. *Langmuir* **2009**, 26, 3596.
- (49) Gai, S.; Yang, P.; Ma, P. a.; Wang, D.; Li, C.; Li, X.; Niu, N.; Lin, J. *J. Mater. Chem.* **2011**, 21, 16420.
- (50) Feng, J.; Fan, W.-Q.; Song, S.-Y.; Yu, Y.-N.; Deng, R.-P.; Zhang, H.-J. *Dalton Transactions* **2010**, 39, 5166.
- (51) Kim, J.; Lee, J. E.; Lee, J.; Yu, J. H.; Kim, B. C.; An, K.; Hwang, Y.; Shin, C.-H.; Park, J.-G.; Kim, J.; Hyeon, T. *J. Am. Chem. Soc.* **2005**, 128, 688.
- (52) Sathe, T. R.; Agrawal, A.; Nie, S. *Anal. Chem.* **2006**, 78, 5627.
- (53) Kim, J.; Kim, H. S.; Lee, N.; Kim, T.; Kim, H.; Yu, T.; Song, I. C.; Moon, W. K.; Hyeon, T. *Angew. Chem. Int. Ed.* **2008**, 47, 8438.
- (54) Liu, H.-M.; Wu, S.-H.; Lu, C.-W.; Yao, M.; Hsiao, J.-K.; Hung, Y.; Lin, Y.-S.; Mou, C.-Y.; Yang, C.-S.; Huang, D.-M.; Chen, Y.-C. *Small* **2008**, 4, 619.
- (55) Deng, Y.; Qi, D.; Deng, C.; Zhang, X.; Zhao, D. *J. Am. Chem. Soc.* **2007**, 130, 28.
- (56) Deng, Y.; Cai, Y.; Sun, Z.; Liu, J.; Liu, C.; Wei, J.; Li, W.; Liu, C.; Wang, Y.; Zhao, D. *J. Am. Chem. Soc.* **2010**, 132, 8466.
- (57) Gai, S.; Yang, P.; Li, C.; Wang, W.; Dai, Y.; Niu, N.; Lin, J. *Adv. Funct. Mater.* **2010**, 20, 1166.
- (58) Ge, J.; Zhang, Q.; Zhang, T.; Yin, Y. *Angew. Chem. Int. Ed.* **2008**, 47, 8924.
- (59) Yang, P.; Quan, Z.; Hou, Z.; Li, C.; Kang, X.; Cheng, Z.; Lin, J. *Biomaterials* **2009**, 30, 4786.
- (60) Huang, S.; Yang, P.; Cheng, Z.; Li, C.; Fan, Y.; Kong, D.; Lin, J. *J. Phys. Chem. C* **2008**, 112, 7130.
- (61) Huang, S.; Fan, Y.; Cheng, Z.; Kong, D.; Yang, P.; Quan, Z.; Zhang, C.; Lin, J. *J. Phys. Chem. C* **2009**, 113, 1775.
- (62) Martín-Saavedra, F. M.; Ruiz-Hernández, E.; Boré, A.; Arcos, D.; Vallet-Regí, M.; Vilaboa, N. *Acta Biomater.* **2010**, 6, 4522.
- (63) Yiu, H. H. P.; Niu, H.-j.; Biermans, E.; van Tendeloo, G.; Rosseinsky, M. J. *Adv. Funct. Mater.* **2010**, 20, 1599.
- (64) Zhu, Y.; Kaskel, S.; Shi, J.; Wage, T.; van Pée, K.-H. *Chem. Mater.* **2007**, 19, 6408.
- (65) Yiu, H. H. P.; Keane, M. A.; Lethbridge, Z. A. D.; Lees, M. R.; Haj, A. J. E.; Dobson, J. *Nanotechnology* **2008**, 19, 255606.
- (66) Zhao, W.; Chen, H.; Li, Y.; Li, L.; Lang, M.; Shi, J. *Adv. Funct. Mater.* **2008**, 18, 2780.
- (67) Wu, H.; Liu, G.; Zhang, S.; Shi, J.; Zhang, L.; Chen, Y.; Chen, F.; Chen, H. *J. Mater. Chem.* **2011**, 21, 3037.
- (68) Liu, J.; Qiao, S. Z.; Budi Hartono, S.; Lu, G. Q. *Angew. Chem. Int. Ed.* **2010**, 49, 4981.
- (69) Zhu, Y.; Kockrick, E.; Ikoma, T.; Hanagata, N.; Kaskel, S. *Chem. Mater.* **2009**, 21, 2547.
- (70) Zhu, Y.; Ikoma, T.; Hanagata, N.; Kaskel, S. *Small* **2010**, 6, 471.
- (71) Zhu, Y.; Fang, Y.; Kaskel, S. *J. Phys. Chem. C* **2010**, 114, 16382.
- (72) Yoon, T.-J.; Kim, J. S.; Kim, B. G.; Yu, K. N.; Cho, M.-H.; Lee, J.-K. *Angew. Chem. Int. Ed.* **2005**, 44, 1068.
- (73) Liu, J.; Qiao, S. Z.; Hu, Q. H.; Lu, G. Q. *Small* **2011**, 7, 425.
- (74) Xu, Z.; Li, C.; Kang, X.; Yang, D.; Yang, P.; Hou, Z.; Lin, J. *J. Phys. Chem. C* **2010**, 114, 16343.
- (75) Chang, B.; Guo, J.; Liu, C.; Qian, J.; Yang, W. *J. Mater. Chem.* **2010**, 20, 9941.

- (76) Shen, S.; Gu, T.; Mao, D.; Xiao, X.; Yuan, P.; Yu, M.; Xia, L.; Ji, Q.; Meng, L.; Song, W.; Yu, C.; Lu, G. *Chem. Mater.* **2011**, *24*, 230.
- (77) Oh, J. K.; Siegwart, D. J.; Lee, H.-i.; Sherwood, G.; Peteanu, L.; Hollinger, J. O.; Kataoka, K.; Matyjaszewski, K. *J. Am. Chem. Soc.* **2007**, *129*, 5939.
- (78) Zhang, X. F.; Mansouri, S.; Clime, L.; Ly, H. Q.; Yahia, L. H.; Veres, T. *J. Mater. Chem.* **2012**, *22*, 14450.
- (79) Chen, P.-J.; Hu, S.-H.; Hsiao, C.-S.; Chen, Y.-Y.; Liu, D.-M.; Chen, S.-Y. *J. Mater. Chem.* **2011**, *21*, 2535.
- (80) Gan, Q.; Lu, X.; Dong, W.; Yuan, Y.; Qian, J.; Li, Y.; Shi, J.; Liu, C. *J. Mater. Chem.* **2012**, *22*, 15960.
- (81) Ruiz-Hernández, E.; Baeza, A.; Vallet-Regí, M. a. *ACS Nano* **2011**, *5*, 1259.
- (82) Gan, Q.; Lu, X.; Yuan, Y.; Qian, J.; Zhou, H.; Lu, X.; Shi, J.; Liu, C. *Biomaterials* **2011**, *32*, 1932.
- (83) Giri, S.; Trewyn, B. G.; Stellmaker, M. P.; Lin, V. S. Y. *Angew. Chem. Int. Ed.* **2005**, *44*, 5038.
- (84) Baeza, A.; Guisasola, E.; Ruiz-Hernández, E.; Vallet-Regí, M. *Chem. Mater.* **2012**, *24*, 517.
- (85) Chang, B.; Sha, X.; Guo, J.; Jiao, Y.; Wang, C.; Yang, W. *J. Mater. Chem.* **2011**, *21*, 9239.
- (86) Nguyen, T. D.; Leung, K. C. F.; Liong, M.; Liu, Y.; Stoddart, J. F.; Zink, J. I. *Adv. Funct. Mater.* **2007**, *17*, 2101.
- (87) Vivero-Escoto, J. L.; Slowing, I. I.; Wu, C.-W.; Lin, V. S. Y. *J. Am. Chem. Soc.* **2009**, *131*, 3462.
- (88) Liu, R.; Zhao, X.; Wu, T.; Feng, P. *J. Am. Chem. Soc.* **2008**, *130*, 14418.
- (89) Muhammad, F.; Guo, M.; Qi, W.; Sun, F.; Wang, A.; Guo, Y.; Zhu, G. *J. Am. Chem. Soc.* **2011**, *133*, 8778.
- (90) Angelos, S.; Yang, Y.-W.; Patel, K.; Stoddart, J. F.; Zink, J. I. *Angew. Chem. Int. Ed.* **2008**, *47*, 2222.
- (91) Liu, R.; Zhang, Y.; Zhao, X.; Agarwal, A.; Mueller, L. J.; Feng, P. *J. Am. Chem. Soc.* **2010**, *132*, 1500.
- (92) Lai, C.-Y.; Trewyn, B. G.; Jeftinija, D. M.; Jeftinija, K.; Xu, S.; Jeftinija, S.; Lin, V. S. Y. *J. Am. Chem. Soc.* **2003**, *125*, 4451.
- (93) Coll, C.; Mondragón, L.; Martínez-Máñez, R.; Sancenón, F.; Marcos, M. D.; Soto, J.; Amorós, P.; Pérez-Payá, E. *Angew. Chem. Int. Ed.* **2011**, *50*, 2138.
- (94) Yang, H.; Zhuang, Y.; Hu, H.; Du, X.; Zhang, C.; Shi, X.; Wu, H.; Yang, S. *Adv. Funct. Mater.* **2010**, *20*, 1733.
- (95) Gang, L.; Huixia, W.; Haoran, Z.; Lihui, T.; He, H.; Hong, Y.; Shiping, Y. *Journal of Materials Science* **2011**, *46*, 5959.
- (96) Wang, F.; Chen, X.; Zhao, Z.; Tang, S.; Huang, X.; Lin, C.; Cai, C.; Zheng, N. *J. Mater. Chem.* **2011**, *21*, 11244.
- (97) Yoon, T.-J.; Yu, K. N.; Kim, E.; Kim, J. S.; Kim, B. G.; Yun, S.-H.; Sohn, B.-H.; Cho, M.-H.; Lee, J.-K.; Park, S. B. *Small* **2006**, *2*, 209.
- (98) Michalet, X.; Pinaud, F. F.; Bentolila, L. A.; Tsay, J. M.; Doose, S.; Li, J. J.; Sundaresan, G.; Wu, A. M.; Gambhir, S. S.; Weiss, S. *Science* **2005**, *307*, 538.
- (99) Sun, P.; Zhang, H.; Liu, C.; Fang, J.; Wang, M.; Chen, J.; Zhang, J.; Mao, C.; Xu, S. *Langmuir* **2009**, *26*, 1278.

- (100) Bakalova, R.; Zhelev, Z.; Aoki, I.; Ohba, H.; Imai, Y.; Kanno, I. *Anal. Chem.* **2006**, 78, 5925.
- (101) Koole, R.; van Schooneveld, M. M.; Hilhorst, J.; Castermans, K.; Cormode, D. P.; Strijkers, G. J.; de Mello Donegá, C.; Vanmaekelbergh, D.; Griffioen, A. W.; Nicolay, K.; Fayad, Z. A.; Meijerink, A.; Mulder, W. J. M. *Bioconjugate Chem.* **2008**, 19, 2471.
- (102) Law, W.-C.; Yong, K.-T.; Roy, I.; Xu, G.; Ding, H.; Bergey, E. J.; Zeng, H.; Prasad, P. N. *J. Phys. Chem. C* **2008**, 112, 7972.
- (103) Lim, Y. T.; Kim, J. K.; Noh, Y.-W.; Cho, M. Y.; Chung, B. H. *Small* **2009**, 5, 324.
- (104) Chen, Y.; Chen, H.; Zhang, S.; Chen, F.; Zhang, L.; Zhang, J.; Zhu, M.; Wu, H.; Guo, L.; Feng, J.; Shi, J. *Adv. Funct. Mater.* **2011**, 21, 270.
- (105) Ma, Z.; Dosev, D.; Nickkova, M.; Dumas, R. K.; Gee, S. J.; Hammock, B. D.; Liu, K.; Kennedy, I. M. *J. Magn. Magn. Mater.* **2009**, 321, 1368.
- (106) Steinkamp, T.; Karst, U. *Analytical and Bioanalytical Chemistry* **2004**, 380, 24.
- (107) Nickkova, M.; Dosev, D.; Gee, S. J.; Hammock, B. D.; Kennedy, I. M. *Anal. Chem.* **2005**, 77, 6864.

## **Chapter II: Magnetic Porous Hollow Silica Nanostructures from $\text{CaCO}_3$ Template for Drug Delivery application**

### **2.1 Introduction**

During the recent decade, magnetic nanoparticles (MPs) have been widely studied for its significant potential in the biomedical field. They have been demonstrated as a promising candidate for applications such as Magnetic Resonance Imaging (MRI) contrast enhancement, targeted drug delivery, hyperthermia cancer treatment and bio-separation due to the characteristics of high saturation magnetization, superparamagnetism, high magnetic susceptibility and low toxicity.<sup>1-4</sup> However, pure magnetic nanoparticle has various practical limitations for easily formed aggregation and being decomposed in a biological environment. Due to this reason, great effort has been focused on concealing the MPs into bio-compatible, low toxic materials for stabilization and protection<sup>5-7</sup> by forming either core-shell structure or composite integration. The most commonly studied protective materials include organic molecules (oleic acid<sup>8</sup>, dopamine<sup>9</sup>, amino acid<sup>10</sup>), polymers (polyethylene glycol<sup>11</sup>, starch<sup>12</sup>, chitosan<sup>13</sup> and polystyrene<sup>14</sup>) and inorganic compounds ( $\text{TiO}_2$ <sup>15</sup>,  $\text{SiO}_2$ <sup>16</sup>). Among all these materials, mesoporous silica is one of the most popular structuring materials because of the various precursors, low cost, and easily designable nature. Its high and well-documented biocompatibility is good for practical applications of magnetic nanoparticles in magnetically guided drug delivery and tumor targeting. Another outstanding advantage of mesoporous silica is the adjustable porous structure, with increased surface area and pore volume, which enables higher drug loading efficiency through surface absorbance and diffusion.

Furthermore, comparing to conventional porous silica material, hollow mesoporous silica nanostructures attracted more attention in the study of drug delivery carriers. The addition of accessible inner surface area through mesoporous channels can significantly increase the specific surface area and pore volume of the nanostructure; therefore, provide much higher storage capacity for drug molecules through massive diffusion or electrostatic absorption.<sup>17-19</sup> This enhanced loading efficiency makes it a preferred host material for sustained and controlled release of a variety of chemical compounds.<sup>20-23</sup>

Proper integration of mesoporous silica with magnetic nanoparticles could generate a new class of drug carrier for targeted delivery and controlled release. The magnetic hollow silica nanospheres, with a character of superparamagnetism, are considered to be the proper carriers for drug delivery. In this chapter,  $\text{Fe}_3\text{O}_4/\text{CaCO}_3$  composite particles were prepared by rotating packed bed (RPB) reactor first, and then employed as templates to fabricate hollow structure and the magnetic nanoparticles remains in hollow core after the removal of  $\text{CaCO}_3$ . Hexadecyltrimethylammonium bromide (CTAB) and octane surfactants were used as second templates to direct the mesoporous structures in the silica shells to eventually achieve magnetic porous hollow silica nanospheres (MPHSN). To investigate the nanomedicine applications, the model drug ibuprofen with poor water solubility was loaded into the MPHSNs to study the drug loading capability and releasing performance. The toxicity of MPHSN was also investigated, and the result showed good bio-compatibility.

On the other hand, silica nanotubes are another novel nanostructure that can be potentially used for carrying more drugs. Different from the nanospheres exposed only exterior surface, nanotubes with open ends offer both the inside and outside surface to interact with drug molecules, which largely increases surface/volume ratio and improves drug loading capacity. In

this chapter, the synthesis of magnetic porous hollow silica nanotubes (MPHSNT) using double templates method is also established using similar method. The resulted product possesses a large surface area with well-defined mesopores, good superparamagnetism property, low toxicity, and a slow release of ibuprofen was observed.

## 2.2 Experimental

**2.2.1 Material and chemicals.** Octane (98%), phosphate buffer saline (PBS, 10x stock solution), tetraethoxysilane (TEOS, 99.9%), hexadecyltrimethylammonium bromide (CTAB, 99%), phosphate buffer saline (PBS, 10x stock solution) were purchase from Sigma-Aldrich. Absolute ethanol was purchased from AAPer Alcohol and Chemical Co. and used as received. Ammonium hydroxide solution (28 wt%) and acetic acid (glacial) were purchased from J.T. Baker. Hexane (mixed isomers, 60+% n-hexane) was purchased from Alfa Aesar. Ibuprofen (USP grade) was purchased from MP Biomedical. Snakeskin pleated dialysis tubing (7,000 MWCO) was purchased from Thermo Scientific.

**2.2.2 Synthesis of  $\text{CaCO}_3$  sacrificial templates.** The  $\text{CaCO}_3/\text{Fe}_3\text{O}_4$  composite nanoparticle was prepared by a high gravity reactive precipitation method using rotating packed bed (RPB) reactor.<sup>24</sup> Briefly, 3500 ml of 5.4wt%  $\text{Ca}(\text{OH})_2$  suspension was added to the reactor with a rotating speed of 750 r/min and circulated at 400 l/h at room temperature.<sup>20,25,26</sup> After 10 min, 75 ml of a methanolic dispersion of  $\text{Fe}_3\text{O}_4$  nanoparticles, which was prepared by a method based on the hydrolysis of chelate metal alkoxide complexes at elevated temperatures in solutions of diethylene glycol<sup>27</sup> (15 mg/ml), was added to the system, and then  $\text{CO}_2$  gas was introduced at a rate of 100 l/h. When the pH value of the suspension reached 7.4, the  $\text{CO}_2$  gas was

stopped to end the reaction. The obtained suspension was filtrated and dried at 70 °C in vacuum for 6 h. CaCO<sub>3</sub> nanoneedles were fabricated through a similar procedure without the addition of Fe<sub>3</sub>O<sub>4</sub> nanoparticles.

**2.2.3 Synthesis of Magnetic Porous Hollow Silica Nanospheres (MPHSN).** In a 250 ml three-neck flask, 3.0 g of as-prepared Fe<sub>3</sub>O<sub>4</sub>/CaCO<sub>3</sub> composite nanoparticles was dispersed ultrasonically into a mixture of 80 ml ethanol and 20 ml distilled water for 30 min and then stirred for 30 min. Next 0.74 g of CTAB was added to the above suspension and the obtained mixture was dispersed ultrasonically for another 20 min<sup>28-30</sup> then stirred for 30 min using a mechanical stirrer. After that, 3.7 ml TEOS was added into the reaction mixture, dropwise, followed by adding the appropriate amount of ammonia (30%) to reach the pH value of 11. The system was stirred at 500 rpm for 2 h and aged for 6h at room temperature, then centrifuged. The precipitate was washed twice with distilled water and once with ethanol, then dried at 50 °C for 6 h and calcined at 550 °C for 5 h in air. Diluted acetic acid solution (HAc: H<sub>2</sub>O = 1:15 by volume) was used to remove the CaCO<sub>3</sub> template by immersing the product in it for 5 h. The product was ,afterwards, rinsed with distilled water and alcohol, and dried at 75 °C for 18 h to yield the MPHSNPs. Mixed CTAB (0.74 g) and octane (3.30 ml) was also used as surfactant in a similar synthesis for the purpose of tuning the pore size of the silica shell.

**2.2.4 Synthesis of Magnetic Porous Hollow Silica Nanotubes (MPHSNT).** The synthesis of MPHSNT is similar to the one of MPHSNS by using CaCO<sub>3</sub> nanoneedles instead of Fe<sub>3</sub>O<sub>4</sub>/CaCO<sub>3</sub> composite nanoparticles. Since the size of the as-prepared CaCO<sub>3</sub> nanoneedles was extremely inhomogeneous and not qualified to be directly used in the synthesis, a size selection



process was performed to achieve more homogenous nanoneedles in advance. First, 20 g of original  $\text{CaCO}_3$  nanoneedles was ultrasonically dispersed in 200 ml ethanol for 2 h then introduced to a series of centrifuging with different rates and times. Then the size of the purified samples was checked with scanning electron microscope (SEM) in order to select the qualified template with acceptable size uniformity for the synthesis using the sol-gel method. First, 3 g size  $\text{CaCO}_3$  nanoneedles after size selection with dimensions of less than 1000 nm in length and 200 nm in diameter were ultrasonically dispersed in a mixture of 80 ml ethanol and 20 ml distilled water in a three-neck flask for 25 min. Then 0.5 ml of a methanolic dispersion of  $\text{Fe}_3\text{O}_4$  nanoparticles (10.66 mg/ml) was added to the suspension above and dispersed in an ultrasonic bath for another 10 min. After that, 1 g of CTAB was applied to the mixture and ultrasonically dispersed for 20 min. Then the flask was settled under a mechanical stirrer and stirred at a rate of 500 rpm. Appropriate amount of ammonia (30%) and 3.2 ml of TEOS was added into the reaction mixture within 10 min to reach the pH value 11. The system was continuously stirred at 500 rpm for 6 h at room temperature, and then aged at room temperature for 4 h. The precipitate was washed twice with distilled water and once with ethanol, then dried at 50 °C for 6 h and calcined at 550 °C for 5 h in air. Diluted acetic acid solution ( $\text{HAc}:\text{H}_2\text{O} = 1:15$  by volume) was used to remove the  $\text{CaCO}_3$  template by immersing the product in it for 5 h. The product was afterwards rinsed with distilled water and alcohol, and dried at 75 °C for 18 h to yield the MPHSNTs. Nanotubes without a mesoporous structure for the purpose of comparison was also prepared by skipping the surfactant CTAB during the sol-gel synthesis.

**2.2.5 Drug loading and releasing test of MPHSN.** At room temperature, 75 mg of MPHSNS was mixed in 25 ml of ibuprofen solution with a concentration of 1.8 mg/ml in hexane and

stirred for 48 h, then collected through centrifuging, washed with hexane for one time and dried in air. The concentration of ibuprofen in the remaining hexane solution was obtained by a Varian Cary 500 UV-vis spectrophotometer after establishing a standard absorbance-concentration curve. After that, the drug loaded sample was dispersed in 50 ml of phosphate buffer saline (PBS) solution under slow magnetic stirring (300 rpm). At selected time points, 1 ml of the drug releasing dispersion was removed from the system, and 1 ml of fresh PBS was added back to the system immediately to maintain a constant volume. The 1 ml extracted dispersion was first centrifuged at 3500 rpm for 15 min, and then the upper clear solution was diluted with 4 ml of PBS and measured by UV-vis spectrophotometer.

**2.2.6 Drug loading and releasing test of MPHSNT.** At room temperature, 25 mg of MPHSNT was mixed in 10 ml of ibuprofen solution with a concentration of 2.0 mg/ml in hexane and stirred for 48 h, then collected through centrifuging, washed with PBS solution for one time and dried in air. After that, the drug loaded sample was dispersed in 2 ml of PBS solution and loaded into a dialysis tube. Then the dialysis tube was soaked in a beaker carrying 10 ml PBS under gentle shaking using a vortex shaker. At selected time points, 2 ml of the solution outside dialysis tube was removed from each beaker, and 2 ml of fresh PBS was added back to the system immediately to maintain a constant volume. The 2 ml extracted solution was then diluted into 4 ml with 1x PBS and measured by UV-vis spectrophotometer. After 48 hours of gentle release, the nanotubes were force to completely discharge the entire loaded drug by a three-hour sonication treatment. 2 ml of the final dispersion was centrifuged and the clear solution was diluted into 4 ml with PBS and measured by spectrophotometer. The concentrations of the samples were obtained after establishing a standard absorbance-concentration curve. And the drug loading

efficiency of silica samples were calculated based on the released amount and concentration of final solution.

**2.2.7 Characterizations.** A Carl Zeiss 1530 VP field emission scanning electron microscope (FESEM) and JEOL 2010 LaB6 transmission electron microscope (TEM) at an accelerating voltage of 200kv were used to examine the morphologies and sizes of the particles. Attached EDAX Genesis analyzer energy dispersive spectroscopy (EDS) was used to determine the composition of nanoparticles. ASAP2020 accelerated surface area and porosimetry system was applied to measure the surface area and pore size distribution of the magnetic porous hollow silica, denoted as BET analysis. The magnetic properties were measured on a Quantum Design MPMS-5S superconducting quantum interference device (SQUID) magnetometer.

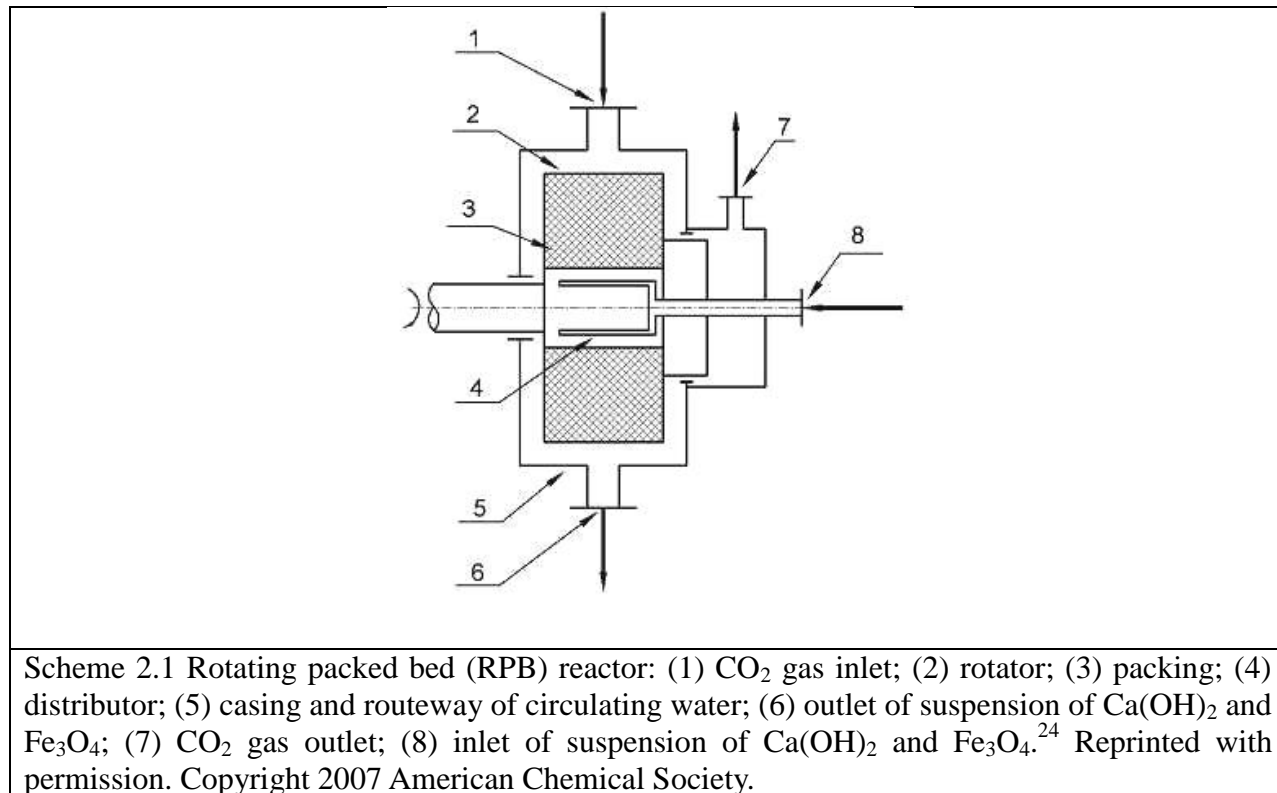
**2.2.8 Toxicity test of MPHSN.** Cell culture: The rat brain cell line CRL-2199 (ATCC, Manassas, Virginia), was used for toxicity testing. Cells were maintained in the suggested medium consisting of Dulbecco's Modified Eagle's medium (with 4.5 g/L glucose, and 1 mM sodium pyruvate), 90%, and fetal bovine serum, 10%. Cells were maintained in humidified 5% CO<sub>2</sub> incubators at 37 °C. Exposure to nanoparticles: CRL-2199 cells were plated onto 35 mm dishes at a density of 50,000 cell/ml. Twenty-four hours after plating, the cells were exposed to 50 µg/ml of porous silica nanoparticle or copper nanoparticle (Sigma-Aldrich, St. Louis, Missouri). Nanoparticles were prepared as a 20x solution in CRL-2199 growth medium and sonicated before addition to cells. Imaging and assessment of toxicity: Cell growth or death was monitored in a pre-marked position of each 35 mm dish and digital images obtained at 40 X magnification using a Nikon Eclipse TE 2000-U model inverted microscope with Photometrics Coolsnap ES

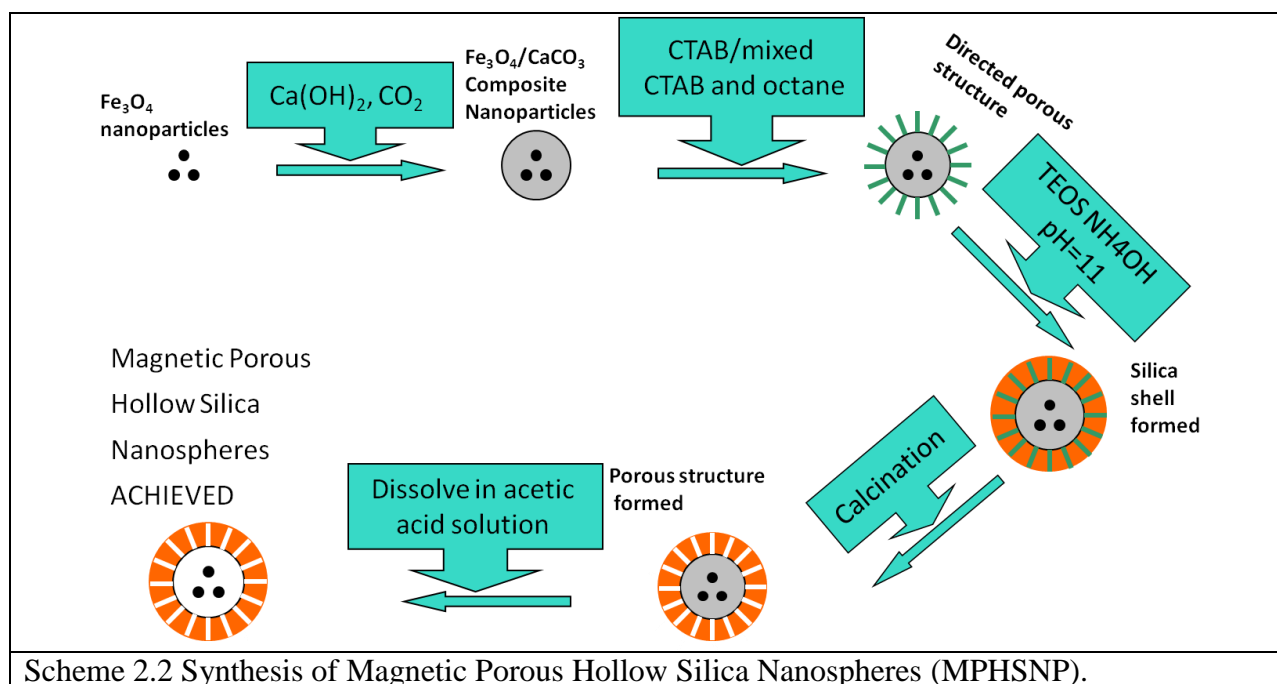
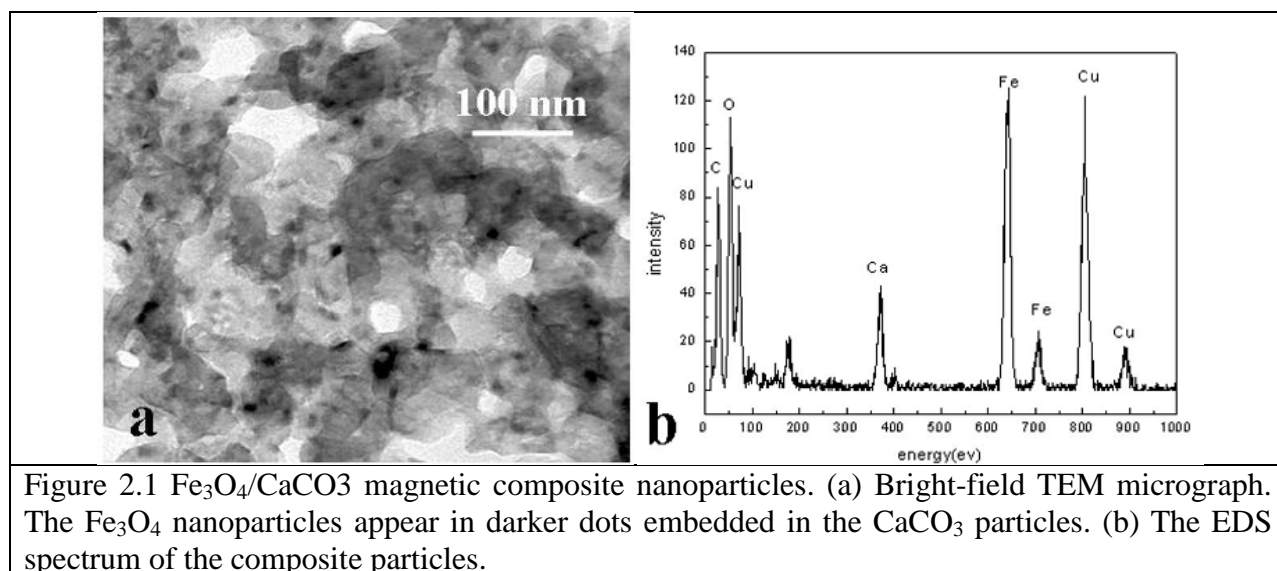
camera and Metamorph acquisition software. After acquisition, digital images were measured for cell growth coverage using Image Pro Plus image analysis software (Version 6.1, Media Cybernetics, Silver Spring, Maryland).

**2.2.9 Toxicity test of MPHSNT.** Cell culture: The rat brain cell line CRL-2020 (ATCC, Manassas, Virginia), was used for toxicity testing. Cells were maintained in the suggested medium consisting of RPMI 1640 medium 90%, and fetal bovine serum, 10%. Cells were maintained in humidified 5% CO<sub>2</sub> incubators at 37 °C. Exposure to nanoparticles: CRL-2020 cells were plated onto 12-well poly-lysine coated culture plates at a density of 30,000 cells/ml. 72 hours after plating, cells were exposed to 50 µg/ml of fabricated porous silica nanotubes or copper nanoparticles (Sigma-Aldrich, St. Louis, Missouri) and placed back into 5% CO<sub>2</sub> incubators as above for 4.5 hours. Nanotubes and nanoparticles were prepared as a 20x concentrated stock in Locke's solution and sonicated before addition to cells. Cell staining: After exposing cells to nanotubes or nanoparticles for 4.5 hours, cells were then loaded with 1 µM of calcein (Invitrogen) and 4 µg/ml of propidium iodide (Sigma-Aldrich) for 30 minutes in a CO<sub>2</sub> incubator, and then imaged by microscopy. Imaging and assessment of toxicity: Cell growth or death was monitored in a pre-marked position of each well and digital images obtained at 200 X magnification using a Nikon Eclipse TE 2000-U model inverted microscope with Photometrics Coolsnap ES camera and Metamorph acquisition software using phase and epifluorescence microscopy for calcein and propidium iodide.

## **2.3 Result and discussion**

**2.3.1 Preparation of  $\text{Fe}_3\text{O}_4/\text{CaCO}_3$  composite nanoparticle template.** In the synthesis of  $\text{Fe}_3\text{O}_4/\text{CaCO}_3$  composite template, RPB (as shown in Scheme 2.1) was employed as a reactor in order to enhance the micromixing strength of the reactant so that the size, size distribution, and reaction rate of  $\text{CaCO}_3$  nanoparticles can be improved.<sup>20</sup> Figure 2.1(a) is a TEM micrograph showing the successfully synthesized  $\text{Fe}_3\text{O}_4/\text{CaCO}_3$  composite nanoparticles. The diameters of  $\text{CaCO}_3$  are about 60-90 nm with magnetic nanoparticles (darker dots) embedded as composite structure. The nanoparticles are slightly aggregated because of the nature of nanoparticles and lack of stabilizing ligand in the synthesis. According to the EDS spectrum shown in Figure 2.1(b), the clear appearance of peaks representing C, O, Ca, and Fe besides Cu peak from TEM grid confirms that composite nanoparticles are indeed composed of  $\text{CaCO}_3$  and  $\text{Fe}_3\text{O}_4$  compounds.

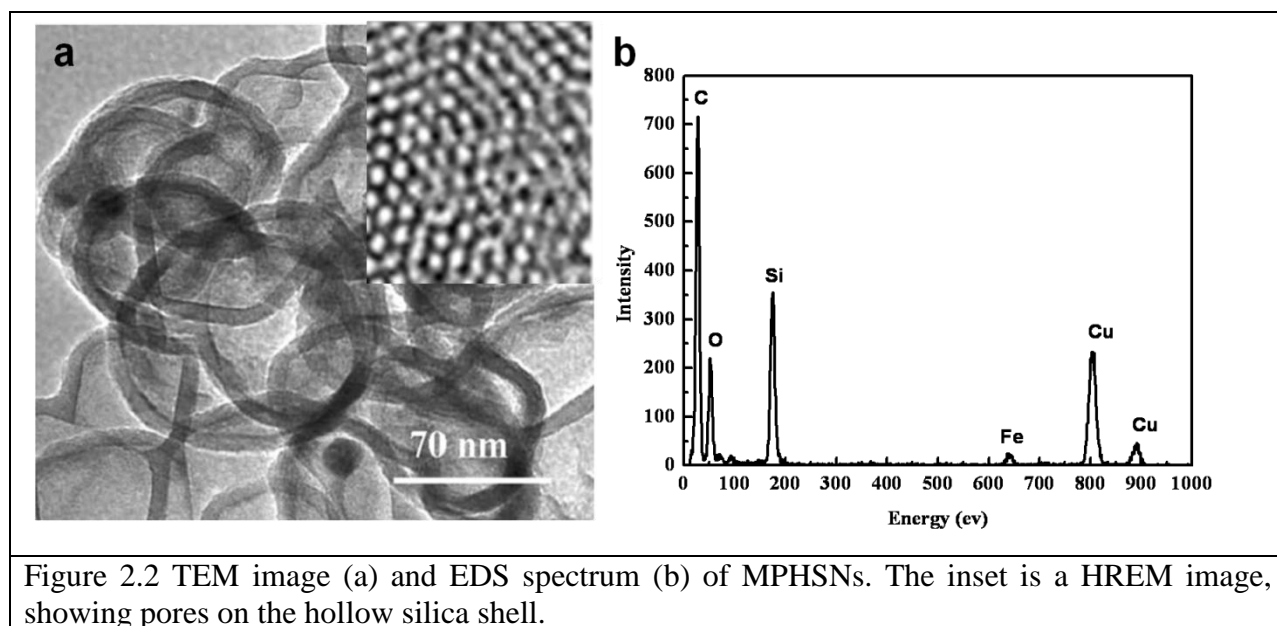




### 2.3.2 Synthesis of Magnetic Porous Hollow Silica Nanospheres (MPHSNs) and BET analysis.

The typical synthesis procedure of MPHSN is illustrated in Scheme 2.2. During the silica shell coating on  $\text{Fe}_3\text{O}_4/\text{CaCO}_3$  composite nanoparticle using sol-gel method, cation surfactant CTAB was first applied as a second template to direct the formation of the mesoporous structure. The cationic carbon chains of CTAB are able to blend with the anionic silicate TEOS molecules upon

contact to build hexagonal mesophase on the outside surface of the  $\text{CaCO}_3$  composite nanoparticle,<sup>31</sup> and the amorphous silica shell is formed through the hydrolysis and condensation of TEOS after the addition of ammonia as a catalyst. After the calcination of CTAB and the removal of  $\text{CaCO}_3$ , by using diluted acetic acid, the magnetic nanoparticles can be clearly observed inside the silica hollow cores, concealed by silica shell with the detailed hexagonal arranged porous structure as shown in Figure 2.2(a). The EDS analysis in Figure 2.2(b) shows no Ca peak, implying that  $\text{CaCO}_3$  was completely etched away after the reaction.



After etching away  $\text{CaCO}_3$ , hollow silica nanospheres containing magnetic nanoparticles were obtained.<sup>24</sup> The surface area of the products was evaluated by nitrogen adsorption-desorption isotherms as shown in Figure 2.3. The isotherm of the sample with only CTAB as well as the one with CTAB and octane possesses a higher position along the vertical axis, indicating a larger pore volume. Also, comparing the sharper inflection on the isotherm to the sample without any surfactant represents uniform pore size formation during capillary

condensation. The actual pore size distribution was achieved through calculation in BJH method and shown in Figure 2.4. According to position of the peak, the pore size of the MPHSNs modified with and CTAB and mixed CTAB and octane are 3.9 nm for and 3.7 nm, respectively, while the sample without any surfactant during preparation doesn't present any distinguishable distribution peak, suggesting less pore size uniformity. This means that a surfactant induced mesoporous structure was successfully formed during the synthesis and were removed during the calcination and rinsing process. The summarized data regarding surface area and pore size is shown in Table 2.1.

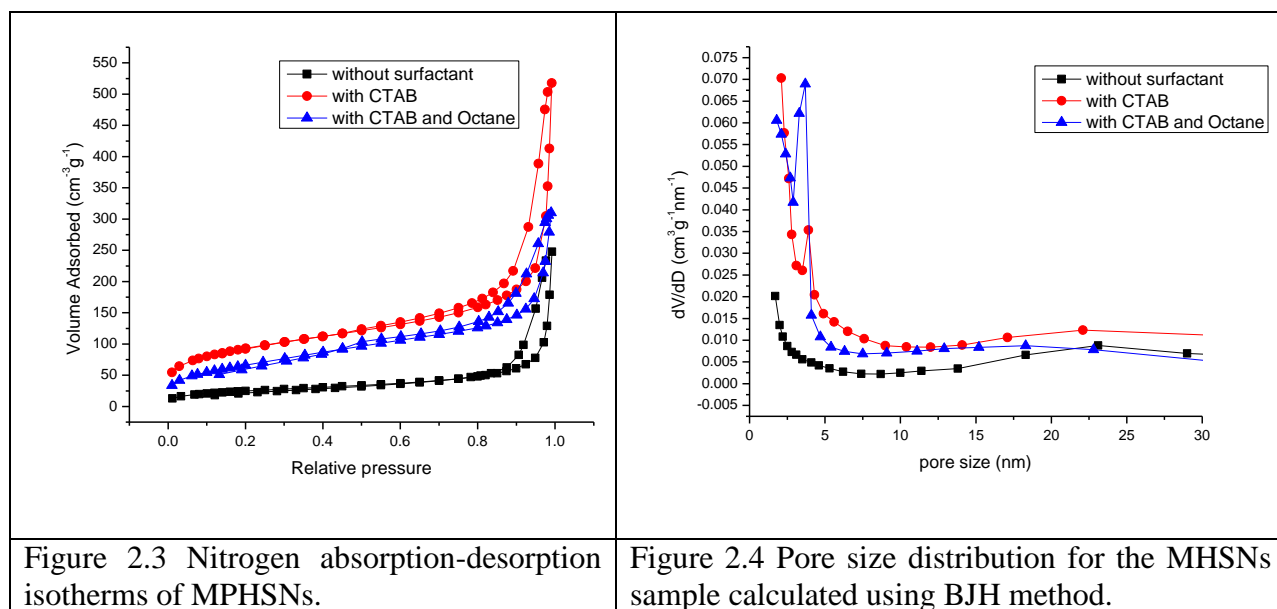
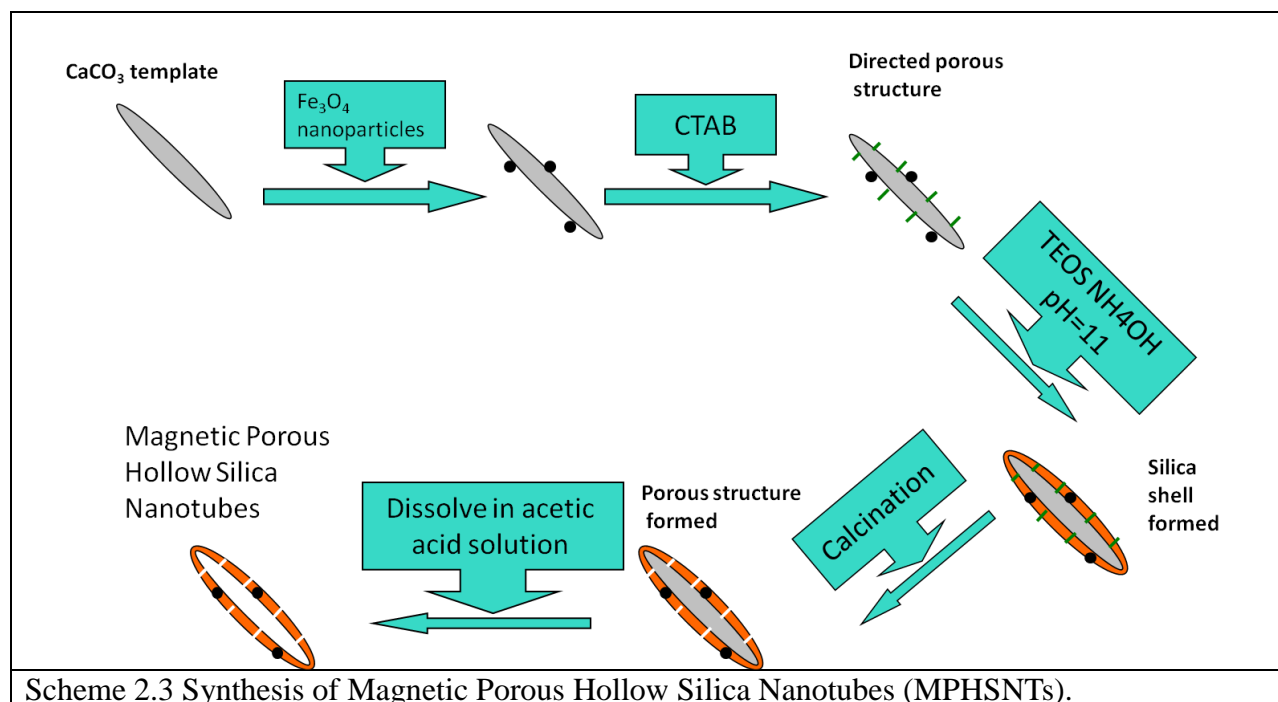


Table 2.1 BET surface area and pore texture parameters of the MPHSNs.

| Surfactant      | Pore size diameter (nm) | BET surface area ( $\text{m}^2/\text{g}$ ) | Drug-load amount (%) |
|-----------------|-------------------------|--|----------------------|
| none            | 1.5                     | 91.9995                                    | 8.70%                |
| CTAB            | 3.9                     | 334.4838                                   | 14.88%               |
| CTAB and octane | 3.7                     | 242.8824                                   | 14.21%               |





**2.3.3 Synthesis and morphology of MPHSNT and BET analysis.** The synthesis procedure of the magnetic hollow silica nanotube (MPHSNT) is illustrated in Scheme 2.3.  $\text{CaCO}_3$  nanoneedles serve as the first template to build the nanotube structure. However, as shown in the SEM images in Figure 2.5(a), as-prepared  $\text{CaCO}_3$  nanoneedles direct from RPB present very wide distribution in size. The length of the nanoneedles varies from about 200 nm to several microns, and the diameter is in the range between tens of nanometer and micron scale. Template with inhomogeneity like this is not suitable for the fabrication of a nanotube drug carrier for multiple reasons: 1) the large sized template makes it hard to penetrate into the cell to deliver the drug; 2) the small sized template may cause massive aggregation of the nanotubes due to the nature of nanomaterials. Therefore, a size selection process was conducted to remove the extra large and small nanoneedles by centrifuging the  $\text{CaCO}_3$  nanoneedles/ethanol dispersion at different rates and times. As the SEM image shown in Figure 2.5(b), the  $\text{CaCO}_3$  nanoneedle template after sized

selection has a relative uniform diameter of 200 nm and length below 1.5  $\mu\text{m}$ , which is qualified for the nanotube synthesis.

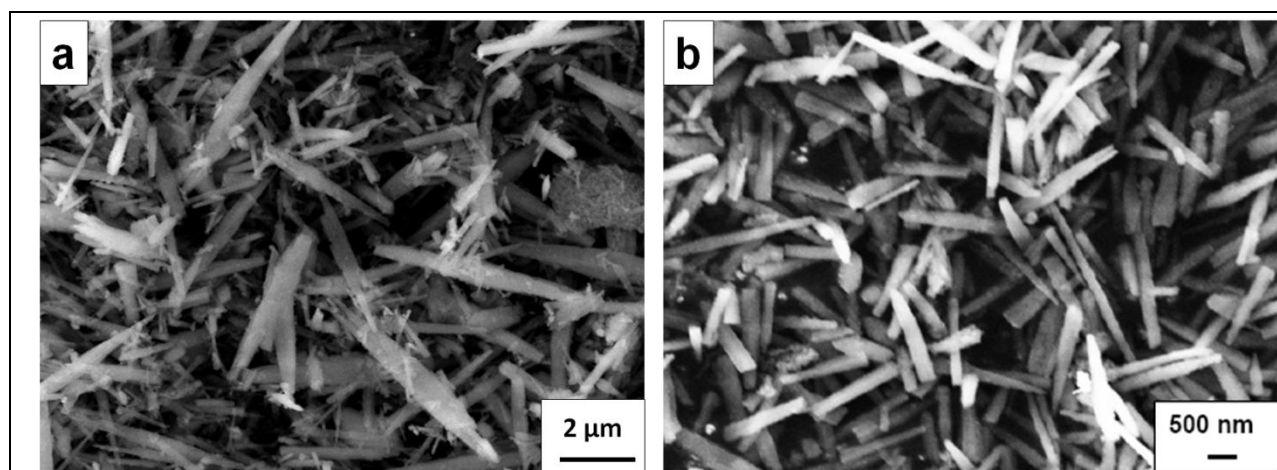


Figure 2.5 SEM image of  $\text{CaCO}_3$  nanoneedle template (a) before and (b) after the size selection process.



Figure 2.6 SEM image of MPHSNTs showing general morphology.

$\text{CaCO}_3$  nanoneedles after size separation was ultrasonically dispersed and mixed with  $\text{Fe}_3\text{O}_4$  nanoparticles. Then cation surfactant CTAB was applied to direct the formation of mesoporous structure, followed by the hydrolysis and condensation of TEOS under the presence of ammonia hydroxide to form the silica shell. After the removal of both templates through calcination and acidic etching, MPHSNT can be achieved. As shown in the SEM image in Figure 2.6 which provides morphology information of the magnetic porous hollow silica nanotube (MPHSNT), the diameter of the nanotubes is below 200 nm and the length is within 1000 nm as pre-determined

by the  $\text{CaCO}_3$  template. Another noticeable point is that most of the nanotubes were broken in the middle with opened ends exposed. This will increase the mesoporous surface area for drug loading which is preferred for drug delivery.

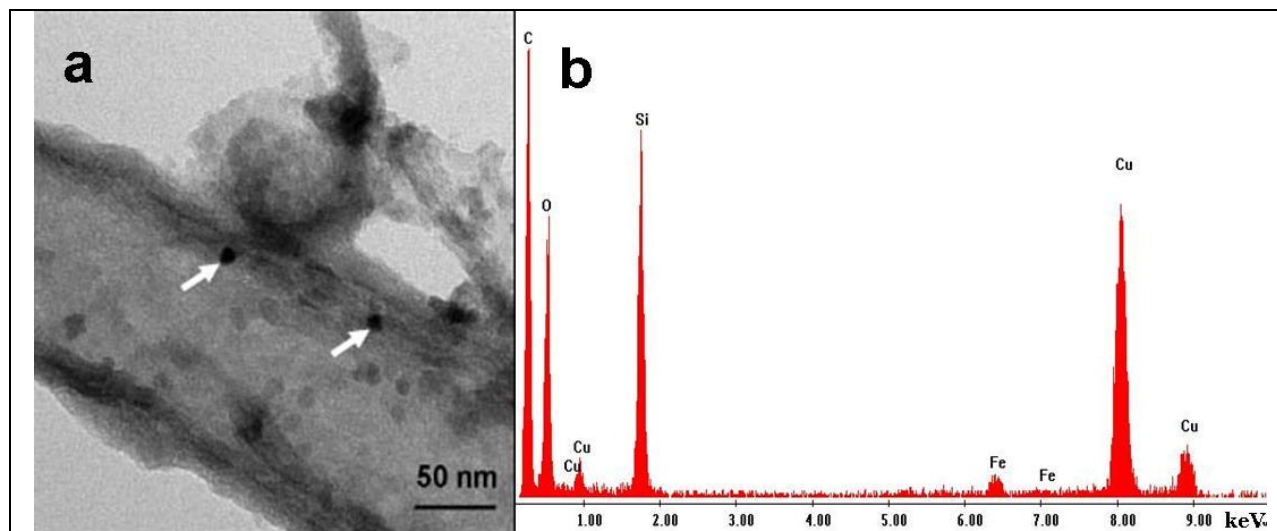


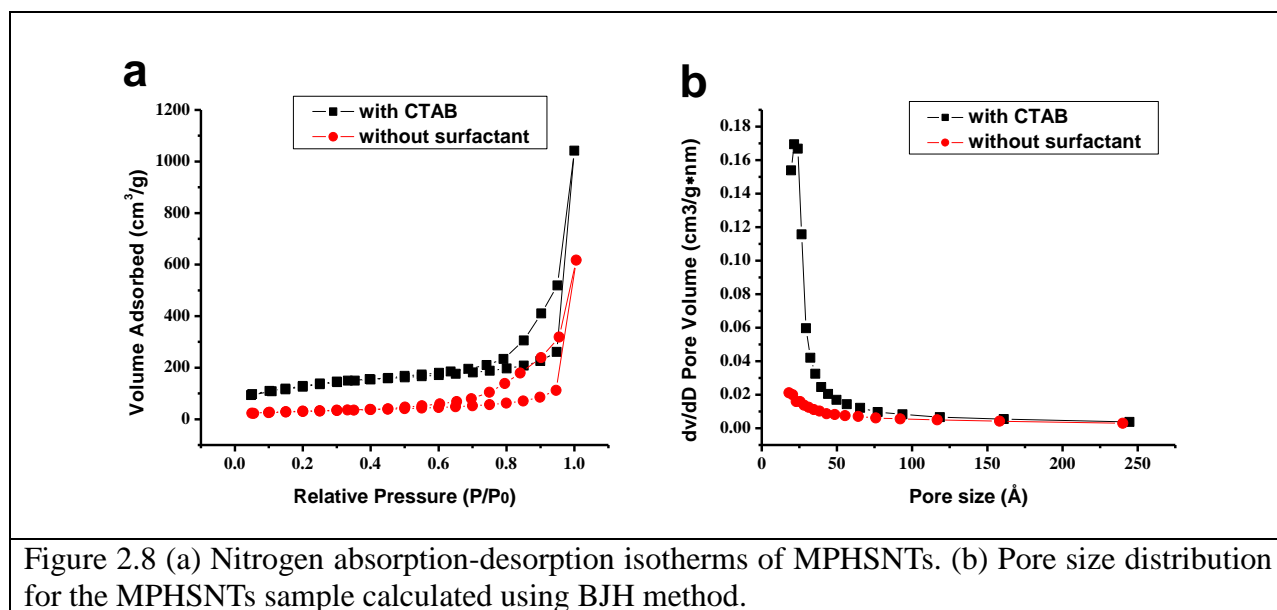
Figure 2.7 (a) TEM image of a MPHSNT, showing the middle region the nanotube. The size of the darker contrast magnetite nanoparticles is about 10 nm. (b) The EDS spectrum of MPHSNT.

Table 2.2 BET surface area and pore texture parameters of the MPHSNTs.

| Surfactant | Pore size diameter (nm) | BET surface area ( $\text{m}^2/\text{g}$ ) | Drug-load amount (% , w/w) |
|------------|-------------------------|--|----------------------------|
| none       | 1.5                     | 43.7807                                    | 7.31                       |
| CTAB       | 2.5                     | 118.6742                                   | 13.87                      |

Figure 2.7(a) is a TEM image showing the middle region of a single MPHSNT. The thickness of silica shell is about 20 nm and the magnetite nanoparticles, with diameters about 10 nm, appear as darker dots. It can be clearly seen that from the edge of the shells the magnetite nanoparticles (denoted by arrows) are successfully embedded in the silica shell. Figure 2.7(b) is the EDS analysis, showing the Si, Fe, and O besides the C and Cu peaks from the sample grid. The presence of the Fe peak also confirms the existence of  $\text{Fe}_3\text{O}_4$  nanoparticles. In addition, the

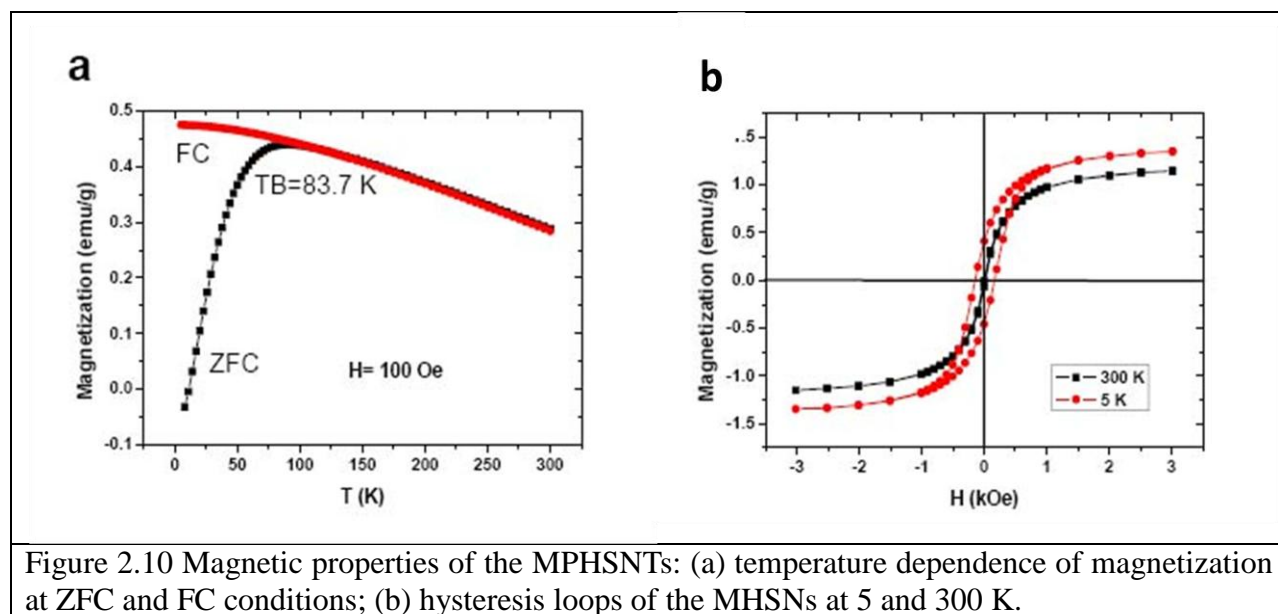
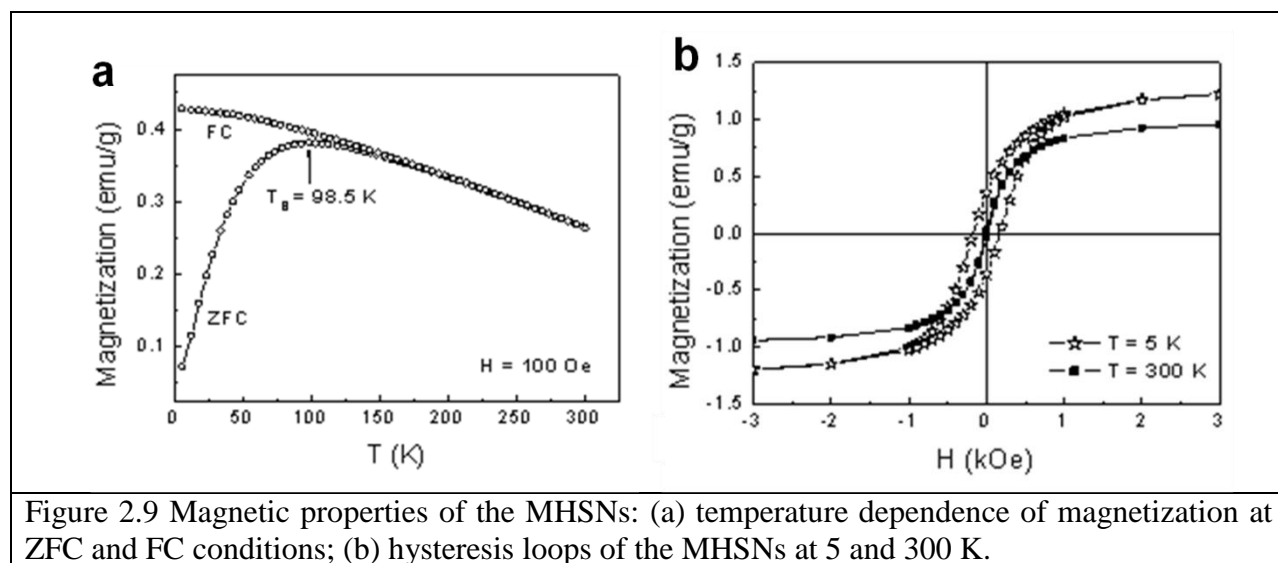
absence of Ca peak indicates that the  $\text{CaCO}_3$  template was completely etched away by the diluted acetic acid, leaving the hollow interior.



During the synthesis of MPHSNT, the cationic surfactant CTAB was introduced as a second template to direct porous structure formation within the silica shell. Information regarding surface areas and pore volume was obtained by measuring  $\text{N}_2$  adsorption-desorption isotherms and pore size distribution was calculated by BJH method. From the isotherms in Figure 2.8(a), it can be clearly seen that the nanotube with surfactant has a much sharper inflection than the one without surfactant during preparation, indicating a more homogeneous mesoporous structure. In Figure 2.8(b), CTAB modified nanotubes represent a quite uniform pore size distribution around 2.5 nm compared with the samples without surfactant modification showing no obvious peak. These mesopores significantly increase the surface area of the nanotube as summarized in Table 2.2, and also behave as nano-channels run through the silica shell, providing a pathway for drug molecule adsorption on both the inside and outside surface for more efficient delivery.

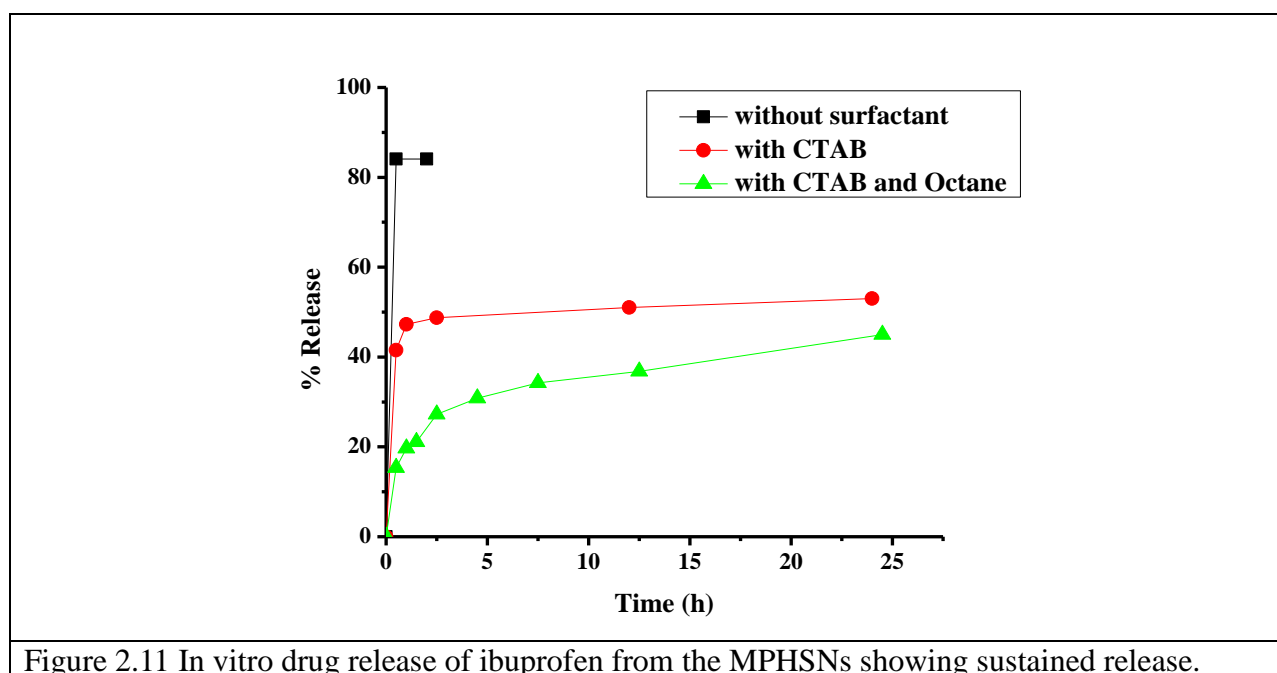
**2.3.4 Magnetic measurements.** The magnetic properties of the MPHSN and MPHSNT were measured by SQUID. Zero-field-cooled (ZFC) and field-cooled (FC) magnetization data measured in the temperature range of 5-300 K are shown in Figure 2.9(a) and Figure 2.10(a). In the ZFC measurement, the initial field was set to zero when cooling the sample from 300 K to 5 K. A field of 100 Oe was applied and the magnetization was measured as the sample was heated from 5 to 300 K. In FC measurement, a field of 100 Oe was applied as the sample was cooled from 300 K to 5 K and the magnetization was measured as the sample was heated from 5 to 300 K, in the field of 100 Oe. The ZFC curves show a maximum at 98.5 K and 83.7 K for MPHSN and MPHSNT, respectively, which are the blocking temperatures ( $T_B$ ) of the magnetic nanoparticles in the samples. Such behavior is the characteristic of superparamagnetism and is due to the progressive blocking of the magnetic moment of the nanoparticles when decreasing the temperature.

Both the nanospheres and nanotubes exhibit superparamagnetism and ferromagnetism above and below the blocking temperature, respectively. To ensure these features, the field-dependent hysteresis loops of the MPHSNs were measured at 5 K ( $<T_B$ ) and 300 K ( $>T_B$ ), as shown in Figure 2.9(b) and Figure 2.10(b). For MPHSN, the hysteresis loop at 5 K shows a saturation magnetization of 1.4 emu/g (at the field of 10000 Oe) and a coercivity of 173 Oe, which confirms that the MPHSNs are ferromagnetic below the blocking temperature. The MPHSNTs present the same ferromagnetic property with a saturation magnetization of 1.35 emu/g and a coercivity of 152 Oe at 5 K. The absence of coercivity in the hysteresis loop at 300 K for both samples indicates a superparamagnetism behavior. The MPHSNs and MPHSNTs possess superparamagnetic properties at room temperature, which means they can be attracted by a magnetic field but retain no residual magnetism once the magnetic field is removed.



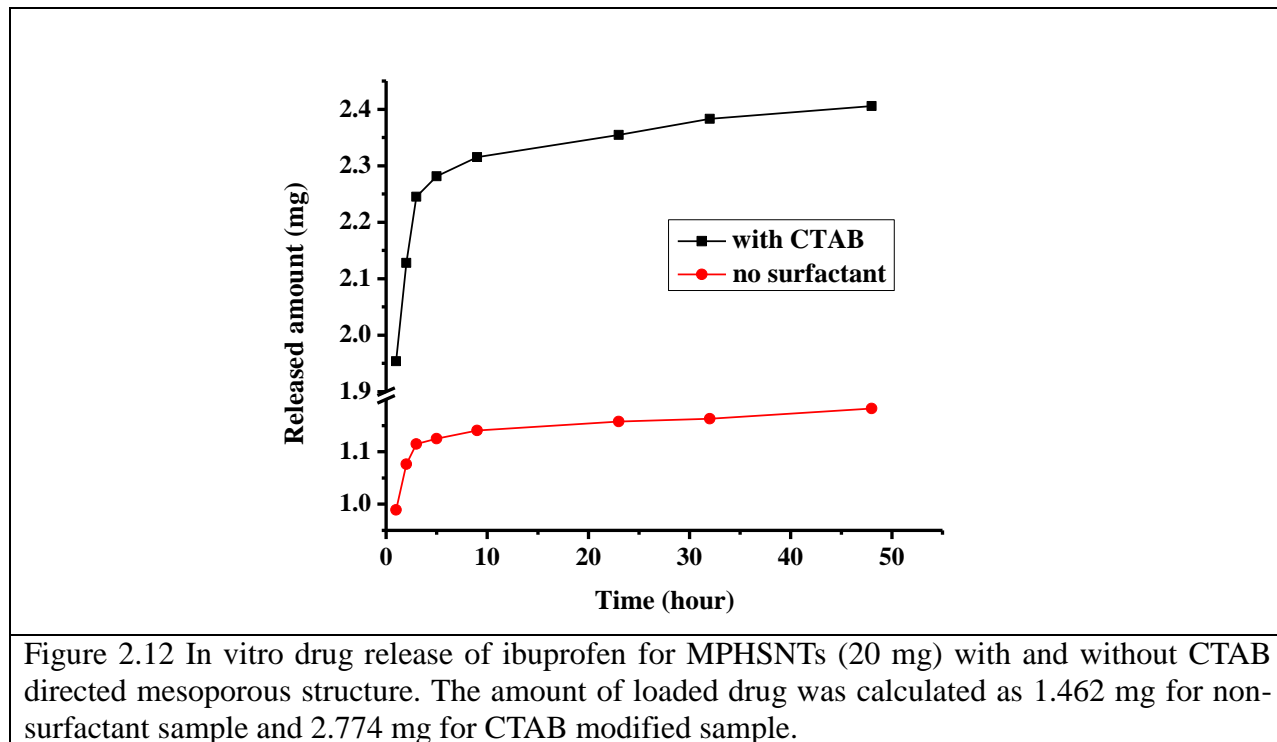
**2.3.5 Drug loading and releasing.** To explore the drug carrying capacity of MPHSNs, ibuprofen, a typical anti-inflammatory drug with poor water solubility, was introduced into the pores of the MPHSNs by immersion in stock solution. The uptake amount of ibuprofen, assessed by UV analysis, was 8.7%, 14.88% and 14.21% for the MPHSNs with pore size of 1.5 nm, 3.9 nm and 3.7 nm (as shown in Table 2.1), respectively, which indicates that the loaded amount of ibuprofen varies with the change of the pore size and surface area. *In-vitro* release behavior was also

investigated by UV-Vis absorbance measurements, as shown in Figure 2.11. It was observed that about 42% and 15% ibuprofen released from the MPHSNs with pore size of 3.9 nm (CTAB) and 3.7 nm (CTAB and octane) during the first half an hour, respectively, and 50% and 42% were released after 24 h respectively. It can be explained that a noticeable amount of drugs entered the mesopores of the hollow structure after modification by the surfactants, resulting in the later sustained release. However, more than 80% of ibuprofen for the MPHSNs without surfactant directed mesoporous structure was released within the first 0.5 h, which indicates that most of ibuprofen was only loaded on the surface of the silica hollow spheres and caused fast initial release.



The drug loading and releasing study for MPHSNTs was also carried out using ibuprofen. The drug loading efficiency of MPHSNT and non-porous nanotube that was prepared as control was 13.87% and 7.31% (w/w) respectively, which is equally comparable to values of nanospheres. It can be explained as the exposure of both the inside and outside surface in

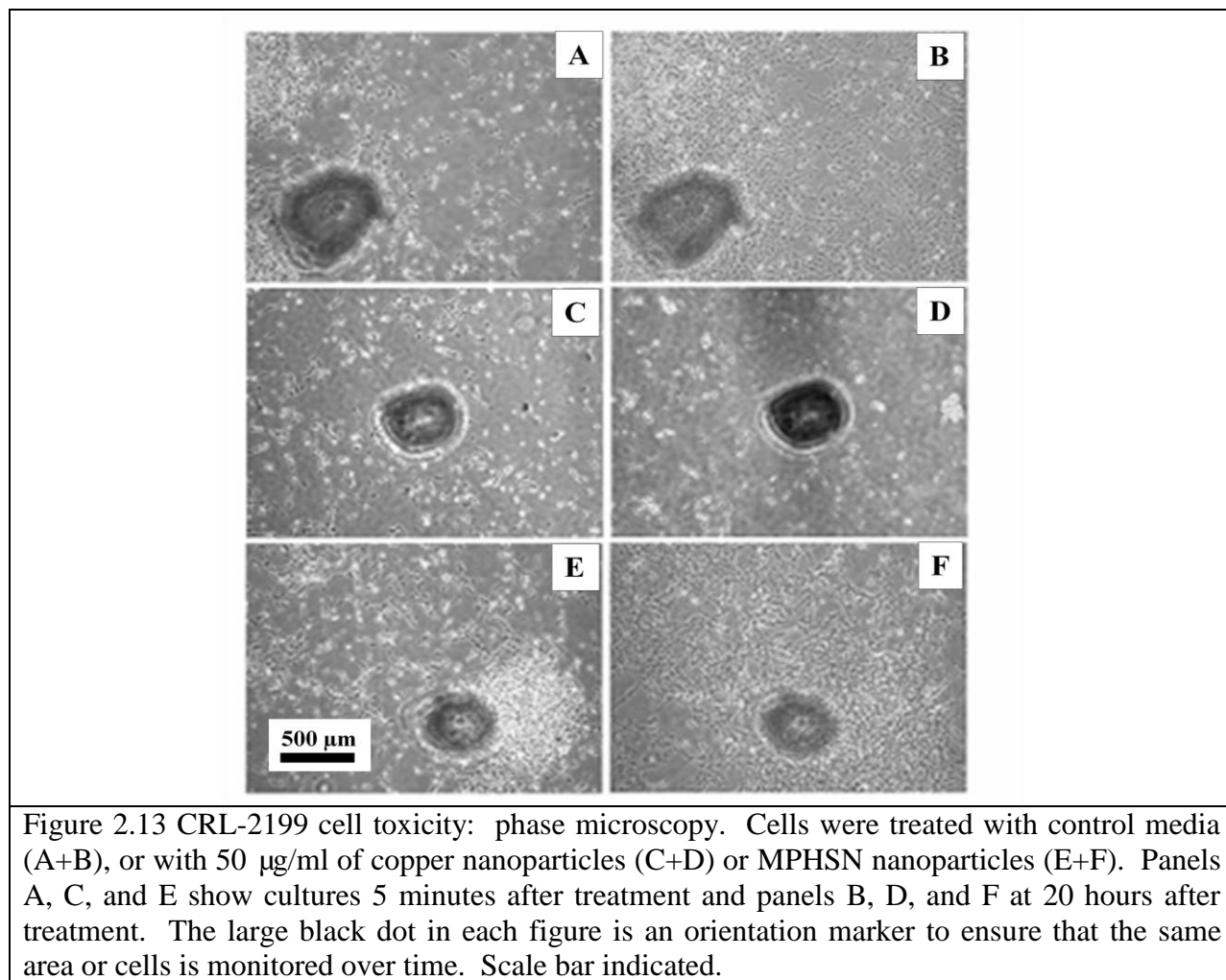
nanotubes, which results in an increased surface/volume ratio. However, while combined with reduced surface/weight ratio due to larger dimensions and thicker silica walls compared to nanospheres, no significant increase of drug loading efficiency was observed. During the investigation of drug release, a dialysis technique was employed to enclose the drug loaded nanotube instead of simple stirring in the release media in order to minimize the external



influence from mechanical disturbance. Unlike mesoporous hollow nanosphere which has an extinguishable sustained release behavior compared with non-porous spheres, both of the nanotube samples, with and without mesopores, exhibit release behavior of approximate 70% of the loaded drug during the first hour and 85% after 5 hours. It is then subject to slow release of remained amount of drugs, as shown in Figure 2.12. The lack of obvious controlled release during initial period can be explained as the broken-in-half nanotubes are serving more like double surfaced vessels rather than hollow capsules, in which the drug molecules adsorbed on

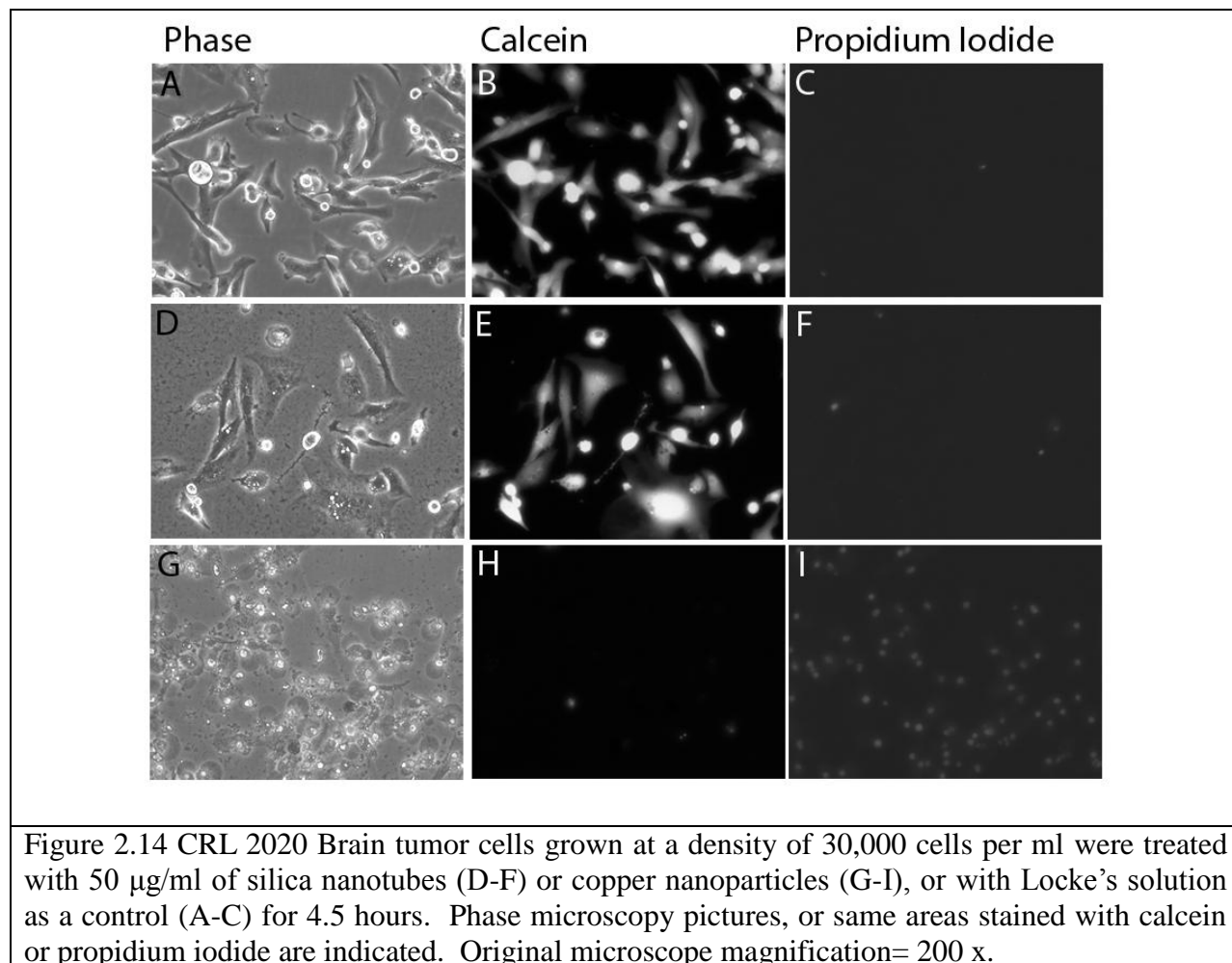


both interior and exterior surfaces can be released at the same time, which resulted in relatively fast initial release. This performance may be more suitable for the treatment of acute infection which requires high drug concentrations to begin with.



**2.3.6 Toxicity studies.** Biocompatibility/toxicity of MPHSNs was tested using the CRL-2199 brain cell line. By comparing the culture treated by 50 µg/ml MPHSN (Figures 2.13 E+F) to the one with only growth media (Figures 2.13 A+B) as blank control at the beginning and 20 hours after applying the nanomaterials, the cells are not showing any obvious sign of death or inactivity, but continue to regular growth and proliferation, indicating low toxicity of as-prepared magnetic silica particle. However, in contrast to the cells cultivated with copper nanoparticles at the same

concentration (Figures 2.13 C+D) which is anticipated as toxic material, the cells presented low viability and no proliferation after 20 hours of incubation. This result indicates that the MPHSN may have potential bio-medical application due to the characteristic of bio-compatibility.



To assess the biocompatibility or potential toxicity of the synthesized silica nanotubes, we exposed the brain cell line CRL 2020 to 50  $\mu\text{g/ml}$  of the fabricated nanotubes and 50  $\mu\text{g/ml}$  of copper nanoparticles respectively for 4.5 hours under normal growth conditions in a 5%  $\text{CO}_2$  incubator. Cell cultivated as the blank control were treated with only physiological Locke's solution.<sup>32</sup> Staining of cells with the vital dye calcein indicated that control cells (Figure 2.14B) and cells treated with nanotubes (Figure 2.14E) were almost completely viable by comparing

with blank control, indicating no toxic effect from the nanotubes. In contrast, treatment of cells with 50  $\mu\text{g/ml}$  of copper nanoparticles caused almost complete loss of calcein staining (Figure 2.14H), and the appearance of significant propidium iodide (PI) staining (Figure 2.14I), an indication of cell death. Control cells and cells treated with nanotubes showed no significant PI staining (Figure 2.14C and F, respectively), demonstrating, by a second indicator, that nanotubes under these conditions are not toxic. As a third marker, no major morphological changes appeared to be occurring due to nanotube exposure under these conditions: cells exposed to nanotubes (Figure 2.14D) appear similar to control cells under phase microscopy (Figure 2.14A), whereas cells exposed to copper nanoparticles show obvious membrane blebbing and cell rupture indicative of cell injury (Figure 2.14G).

## 2.4 Conclusion

In this chapter, magnetic porous hollow silica nanospheres as targeting drug carriers were successfully synthesized using  $\text{CaCO}_3/\text{Fe}_3\text{O}_4$  composite nanoparticles as the first template, and cationic surfactants as the second template in a sol-gel system. The results show that the pore size of the MPHSNs can be tuned by adjusting the surfactants in the system. No  $\text{CaCO}_3$  and surfactant were left after calcination and weak acid etching. SQUID measurements show that the MPHSNs still maintain the superparamagnetic behavior after the calcination. In addition, in vitro release study of ibuprofen shows that MPHSNs can significantly sustain the drug release, and toxicity test suggests good biocompatibility, which indicates their strong potential applications in the biomedical field. Also, magnetic porous hollow silica nanotubes (MPHSNTs) were also successfully prepared by using  $\text{CaCO}_3$  nanoneedle as the sacrificial template for the hollow structure. Most of the obtained nanotubes were broken in the middle and both the interior and

exterior surface of the tube can be exposed to interact with drug molecules, which largely increase the drug loading efficiency. A slow release behavior of ibuprofen was observed compared to the sample without mesoporous feature, and superparamagnetism property from the Fe<sub>3</sub>O<sub>4</sub> nanoparticles was preserved. Both of the nanospheres and nanotubes showed low toxicity in human cells, indicating great potential as qualified carriers for targeted drug delivery.

## 2.7 References:

- (1) Tanaka, T.; Matsunaga, T. *Anal. Chem.* **2000**, *72*, 3518.
- (2) Yang, H.-H.; Zhang, S.-Q.; Chen, X.-L.; Zhuang, Z.-X.; Xu, J.-G.; Wang, X.-R. *Anal. Chem.* **2004**, *76*, 1316.
- (3) Levy, L.; Sahoo, Y.; Kim, K.-S.; Bergey, E. J.; Prasad, P. N. *Chem. Mater.* **2002**, *14*, 3715.
- (4) Haukanes, B.-I.; Kvam, C. *Nat Biotech* **1993**, *11*, 60.
- (5) Bruce, I. J.; Taylor, J.; Todd, M.; Davies, M. J.; Borioni, E.; Sangregorio, C.; Sen, T. *J. Magn. Magn. Mater.* **2004**, *284*, 145.
- (6) Liu, X.; Ma, Z.; Xing, J.; Liu, H. *J. Magn. Magn. Mater.* **2004**, *270*, 1.
- (7) Santra, S.; Tapecc, R.; Theodoropoulou, N.; Dobson, J.; Hebard, A.; Tan, W. *Langmuir* **2001**, *17*, 2900.
- (8) Sun, S.; Zeng, H. *J. Am. Chem. Soc.* **2002**, *124*, 8204.
- (9) Xu, C.; Xu, K.; Gu, H.; Zheng, R.; Liu, H.; Zhang, X.; Guo, Z.; Xu, B. *J. Am. Chem. Soc.* **2004**, *126*, 9938.
- (10) Qu, H.; Ma, H.; Zhou, W.; O'Connor, C. J. *Inorg. Chim. Acta* **2012**, *389*, 60.
- (11) Mukhopadhyay, A.; Joshi, N.; Chattopadhyay, K.; De, G. *ACS Appl. Mater. Inter* **2011**, *4*, 142.
- (12) Mikhaylova, M.; Kim, D. K.; Bobrysheva, N.; Osmolowsky, M.; Semenov, V.; Tsakalakos, T.; Muhammed, M. *Langmuir* **2004**, *20*, 2472.
- (13) Chang, Y.-C.; Chen, D.-H. *J. Colloid Interface Sci.* **2005**, *283*, 446.
- (14) Ramírez, L. P.; Landfester, K. *Macromol. Chem. Phys.* **2003**, *204*, 22.
- (15) Li, Y.; Xu, X.; Qi, D.; Deng, C.; Yang, P.; Zhang, X. *J. Proteome Res.* **2008**, *7*, 2526.
- (16) Ma, D.; Veres, T.; Clime, L.; Normandin, F.; Guan, J.; Kingston, D.; Simard, B. *J. Phys. Chem. C* **2007**, *111*, 1999.
- (17) Yufang, Z.; Jianlin, S.; Weihua, S.; Hangrong, C.; Xiaoping, D.; Meilin, R. *Nanotechnology* **2005**, *16*, 2633.
- (18) Zhu, Y.; Shi, J.; Chen, H.; Shen, W.; Dong, X. *Microporous Mesoporous Mater.* **2005**, *84*, 218.
- (19) Zhu, Y.; Ikoma, T.; Hanagata, N.; Kaskel, S. *Small* **2010**, *6*, 471.
- (20) Chen, J.-F.; Ding, H.-M.; Wang, J.-X.; Shao, L. *Biomaterials* **2004**, *25*, 723.
- (21) Doadrio, A. L.; Sousa, E. M. B.; Doadrio, J. C.; Pérez Pariente, J.; Izquierdo-Barba, I.; Vallet-Regí, M. *J. Control Release* **2004**, *97*, 125.

- (22) Doadrio, J. C.; Sousa, E. M. B.; Izquierdo-Barba, I.; Doadrio, A. L.; Perez-Pariente, J.; Vallet-Regi, M. *J. Mater. Chem.* **2006**, *16*, 462.
- (23) Horcajada, P.; Rámila, A.; Pérez-Pariente, J.; Vallet, R.; amp; x; M. *Microporous Mesoporous Mater.* **2004**, *68*, 105.
- (24) Zhou, J.; Wu, W.; Caruntu, D.; Yu, M. H.; Martin, A.; Chen, J. F.; O'Connor, C. J.; Zhou, W. L. *J. Phys. Chem. C* **2007**, *111*, 17473.
- (25) Shao, L.; Caruntu, D.; Chen, J. F.; O'Connor, C. J.; Zhou, W. L. *J. Appl. Phys.* **2005**, *97*, 10Q908.
- (26) Wu, W.; DeCoster, M. A.; Daniel, B. M.; Chen, J. F.; Yu, M. H.; Cruntu, D.; O'Connor, C. J.; Zhou, W. L. *J. Appl. Phys.* **2006**, *99*, 08H104.
- (27) Caruntu, D.; Caruntu, G.; Chen, Y.; O'Connor, C. J.; Goloverda, G.; Kolesnichenko, V. L. *Chem. Mater.* **2004**, *16*, 5527.
- (28) Lu, Y.; Yang, Y.; Sellinger, A.; Lu, M.; Huang, J.; Fan, H.; Haddad, R.; Lopez, G.; Burns, A. R.; Sasaki, D. Y.; Shelnutt, J.; Brinker, C. J. *Nature* **2001**, *410*, 913.
- (29) Wang, D.; Zhou, W. L.; McCaughy, B. F.; Hampsey, J. E.; Ji, X.; Jiang, Y. B.; Xu, H.; Tang, J.; Schmehl, R. H.; O'Connor, C.; Brinker, C. J.; Lu, Y. *Adv. Mater.* **2003**, *15*, 130.
- (30) Lu, Y. *Angew. Chem. Int. Ed.* **2006**, *45*, 7664.
- (31) Monnier, A.; Schüth, F.; Huo, Q.; Kumar, D.; Margolese, D.; Maxwell, R. S.; Stucky, G. D.; Krishnamurty, M.; Petroff, P.; Firouzi, A.; Janicke, M.; Chmelka, B. F. *Science* **1993**, *261*, 1299.
- (32) DeCoster, M. A.; Lambeau, G.; Lazdunski, M.; Bazan, N. G. *J. Neurosci. Res.* **2002**, *67*, 634.

## **Chapter III: Magnetic porous hollow silica nanospheres (MPHSNs) templated from polystyrene beads**

### **3.1 Introduction**

Superparamagnetic iron oxide nanoparticles (SPIONs) possess the unique feature of zero coercivity which allows the particles to move toward and stay at a desired area under the existence of an external magnetic field and leaves no residual magnetization upon removal of the magnetic field.<sup>1</sup> This characteristic is significantly beneficial for magnetic targeted drug delivery which is in high demand for the treatment of infections and tumors nowadays. In recent years, numerous efforts have been made on the efficient and convenient integration of SPIONs on mesoporous silica to combine the benefits of superparamagnetism, large surface area and good bio-compatibility as the platform for various bio-medicine applications such as targeted drug delivery, multimodal imaging, hyperthermia treatment and bio-separation.<sup>2,3</sup> So far, many strategies have been developed for this purpose, including SPION/silica core-shell structures,<sup>4-6</sup> rattle type structures,<sup>7-9</sup> as well as embedded composite structures in which the SPIONs are grown inside silica mesoporous framework.<sup>10-12</sup> One of the most direct approaches is covalently conjugating SPIONs on a silica surface through linkage reactions such as amine-carboxyl,<sup>13</sup> amine-thiol<sup>14</sup> and amine-bromine.<sup>15,16</sup> Being as straight forward as it is, this method invites complexities of relatively low crosslinking efficiency, complicated preparations of both silica and SPION, and sophisticated ligand exchange processes of magnetic particles, which makes it time consuming and less scalable. Therefore, a more facile approach with higher efficiency of the decoration of SPIONs on silica with an additional advantage of availability for further functionalization is highly preferred.

In this chapter, two different pathways were used to synthesize magnetic porous hollow silica nanospheres (MPHSNs) for the application of drug delivery. In the first approach, PS nanoparticles with carboxylic group functionality were prepared by introducing acrylic acid as a comonomer, and then attached with Fe<sub>3</sub>O<sub>4</sub> nanoparticles through either covalent bindings or in-situ growth, followed by silica coating and PS template removal to achieve the hollow structure. In the second approach, mesoporous hollow silica nanospheres were first synthesized basing on the PS nanoparticle templating, then the in-situ growth of Fe<sub>3</sub>O<sub>4</sub> nanoparticles was conducted in a mixed polyamine-polyalcohol media to obtain magnetic decorated hollow sphere with amine functionality. The resulted product from the latter procedure reserved the mesoporous structure from the original silica nanospheres and exhibited strong superparamagnetism properties at room temperature. And the reactive amine groups were available for further modification and functionalization such as fluorescence conjugation.

## 3.2 Experimental

**3.2.1 Material and chemicals.** Styrene (99.0%), 2,2'-Azobis(2-methylpropionamidine) dihydrochloride (V-50, 97.0%), polyvinylpyrrolidone (PVP40, 99.5%), hexadecyltrimethylammonium bromide (CTAB, 99.0%), [2-(acryloyloxy)ethyl] trimethylammonium chloride (AETAC, 80 wt % in water), tetraethoxysilane (TEOS, 99.9%), potassium persulfate (K<sub>2</sub>S<sub>2</sub>O<sub>8</sub>, 99%), sodium dodecyl sulfate (SDS, 99%), sodium bicarbonate (NaHCO<sub>3</sub>, 99.5%), acrylic acid (99%), allylamine (99%), divinyl benzene (80%, mixture of isomers), (3-Aminopropyl)triethoxysilane (APTES, 98%), diethylene glycol (DEG, 99%), triethylene glycol (TREG, 99%), tetraethylene glycol (TEG, 99%), triethylenetetramine (TETA, 97%), tetraethylenepentamine (TEPA, technical grade), iron(III) acetylacetonate

(Fe(acac)<sub>3</sub>, 97%), iron(II) chloride tetrahydrate (FeCl<sub>2</sub>•4H<sub>2</sub>O, 99%), Iron(III) chloride hexahydrate (FeCl<sub>3</sub>•6H<sub>2</sub>O, 99%), sodium hydroxide (NaOH, 99%), *N*-(3-Dimethylaminopropyl)-*N'*-ethylcarbodiimide hydrochloride (EDC, 99%), *N*-Hydroxysuccinimide (NHS, 98%) were purchased from Sigma-Aldrich. Absolute ethanol was purchased from AAPer Alcohol and Chemical Co. and used as received. Ammonium hydroxide solution (28 wt%) was purchased from J.T. Baker. Amicon Ultra centrifuge filter (regenerate cellulose 30K MWCO) was purchased from Millipore for spin dialysis. Water soluble CdSe/ZnS core/shell quantum dots with 595 nm emission peak and carboxyl functionality were purchase from Ocean Nanotech.

**3.2.2 Synthesis of polystyrene nanoparticles.** The synthesis procedures described below are based on published work<sup>17-22</sup> with modification using our limited apparatus set-up: round bottom three-neck flask, hotplate, sandbath and condenser connected with cooling water.

**PVP method:** In a 250 ml round bottom three-neck flask, 0.224 g of PVP40 was dissolved in 158 ml of distilled water, and kept stirring at 1200 rpm on a hotplate for 20 min. Then 17.0 ml/15.5 g of styrene was added in the solution and the emulsion was purged with nitrogen and stirred for another 30 min. After heated to 70 °C with a sand bath, 2.4 ml of V-50 (10 wt % in water) was added to induce the polymerization and the reaction mixture was refluxed at 70 °C for 24 hours under constant nitrogen flow.

**Divinyl benzene method:** In a 250 ml round bottom flask, 3.0 ml of styrene and 0.030 ml of divinyl benzene was injected into 100 ml of H<sub>2</sub>O under vigorous stirring and nitrogen purge. An AALABORG GFM17 mass flow meter was used to monitor the flow rate of nitrogen. After heated to 70 °C, 6.0 ml of 37 mM K<sub>2</sub>S<sub>2</sub>O<sub>8</sub> aqueous solution was injected to initiate the polymerization. At the same time, various amount of acrylic acid was also added to provide



functional carboxyl group for the purpose of further surface modification. The reaction was kept under reflux and nitrogen for 24 h and the mixture was introduced to reduced pressure filtration to remove the large agglomeration that caused by insufficient stirring.

***3.2.3 Synthesis of amine-ended  $\text{Fe}_3\text{O}_4$  nanoparticles, linkage to carboxyl-ended PS beads and formation of magnetic porous hollow silica nanospheres (MPHSNs).***  $\text{Fe}_3\text{O}_4$  nanoparticles with reactive amine surface functionality were first prepared based on a published method with modification.<sup>23</sup> In a 50 ml three-neck flask, 0.177 g (0.5 mmol) of  $\text{Fe}(\text{acac})_3$  was mixed with 10 g of TETA via magnetic stirring under a flow of nitrogen, and the mixture was first heated to 200 °C for 30 min, then eventually heated to 260 °C for another 1.5 h. The obtained  $\text{Fe}_3\text{O}_4$  nanoparticles with water solubility were magnetically collected, washed 5 times with acetone and then redispersed in 10 ml of  $\text{H}_2\text{O}$ .

Through spin dialysis, 10 mg of PS beads with carboxyl functional group from the divinyl benzene method was collected and redispersed in 2 ml of  $\text{H}_2\text{O}$ . Then 100 mg of zero-length crosslinker EDC and 10 mg of NHS were dissolved in the PS beads dispersion to have the carboxyl group activated for 15 min, followed by mixing with 0.5 ml of  $\text{Fe}_3\text{O}_4$  nanoparticle aqueous solution described above and 7.5 ml of  $\text{H}_2\text{O}$ . The reaction lasted 4 h before washed with ethanol for 5 times and redispersed in 10 ml of ethanol.

At last, 2 ml of the magnetic nanoparticles linked PS beads obtained above was diluted with 10 ml of ethanol and dispersed under ultrasonic for 30 min, followed by adding 0.020 g of PVP and moved to magnetic stirring at 1200 rpm at room temperature. Then 0.3 ml of TEOS and 1.0 ml of APTES was applied as precursor of silica and the reaction mixture was stirred for 12 h.

**3.2.4 In-situ growth of  $Fe_3O_4$  nanoparticles on PS beads.** The synthesis and in-situ attach of  $Fe_3O_4$  nanoparticles to PS beads was carried out through a polyol mediate synthesis method<sup>24</sup> with modification. In a typical procedure, 0.16 g of NaOH (40 mmol) was first dissolved in 10 g of DEG by stirring overnight. Then 15 mg of PS beads, which was separated from original reaction solution by spin dialysis, as well as 25 mg of  $FeCl_2 \cdot 4H_2O$  (0.125 mmol) and 67.5 mg of  $FeCl_3 \cdot 6H_2O$  (0.25 mmol) was dispersed in 20 g of DEG and stirred for 1 h. Under a flow of nitrogen, the two solutions were then mixed together and stirred for another 3 h, followed by heating to 220 °C via controlled ramp (room temperature (RT) to 150 °C at 3 °C/min, then heat to 220 °C at 1 °C/min). After naturally cooled down to room RT, the sample was collected through magnet and washed 5 times in acetone, then dispersed in ethanol.

**3.2.5 Synthesis of mesoporous hollow silica nanospheres (MHSN).** In a typical experiment, 5 mg of PS beads was first separated from original reaction solution by spin dialysis, and then ultrasonically dispersed in a mixture of 8 ml ethanol and 2 ml of  $H_2O$  in a 20 ml vial. Appropriate amount of CTAB which serves as surfactant was added to direct the formation of porous structure during 1 h of magnetic stirring. Then the solution was heated to 50 °C and certain amount of TEOS was dropwisely applied, followed by addition of concentrated ammonium hydroxide to initiate the hydrolysis of TEOS. The reaction was kept at elevated temperature for 24 hours and the product was washed with ethanol and dried in air. At last, the dried product was calcined at 600 °C for 6 h to remove the PS and CTAB templates, and the mesoporous hollow silica nanospheres was achieved. Synthesis using  $H_2O$  only, ethanol only, different  $H_2O$ /ethanol ratios, and 10 times large scale were also studied.

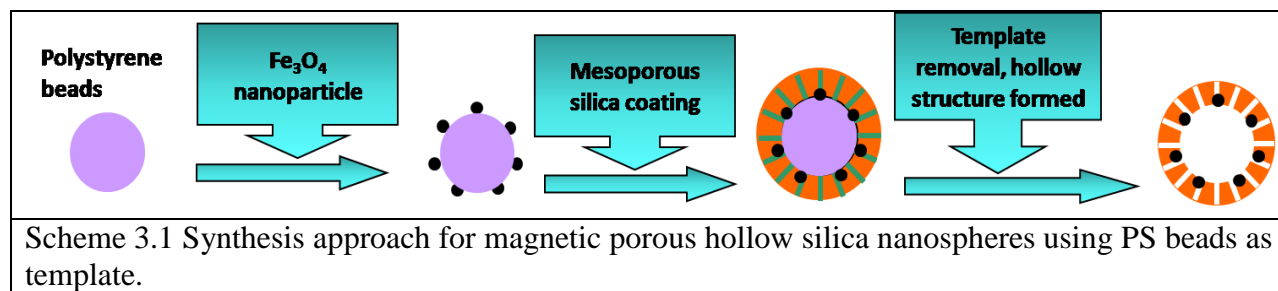
**3.2.6 In situ growth of  $Fe_3O_4$  nanoparticles on mesoporous hollow silica nanospheres.** Based on a typical thermal decomposition method,  $Fe_3O_4$  nanoparticles were synthesized and attached to the surface of MHSNs through a one-pot procedure.<sup>23,25,26</sup> Briefly, 40 mg of MHSN was dispersed in 2 ml of water for 20 min in ultrasonic bath, then mixed with x g of TEG, y g of TETA or TEPA, (x+y=10) and 0.177 g (0.5 mmol) of  $Fe(acac)_3$  in a 50 ml three-neck flask connected with nitrogen inlet, condenser and temperature controller. Under a flow of nitrogen and magnetic stirring, the reaction mixture was first heated to 120-150 °C for about 30 min to remove the water through evaporation. The temperature was then raised to 220 °C for 2 h during which the  $Fe(acac)_3$  started to decomposes. Eventually, the mixture was heat to 300 °C for various amount of time and the product was magnetically collected, washed 5 times with acetone and re-dispersed in ethanol.

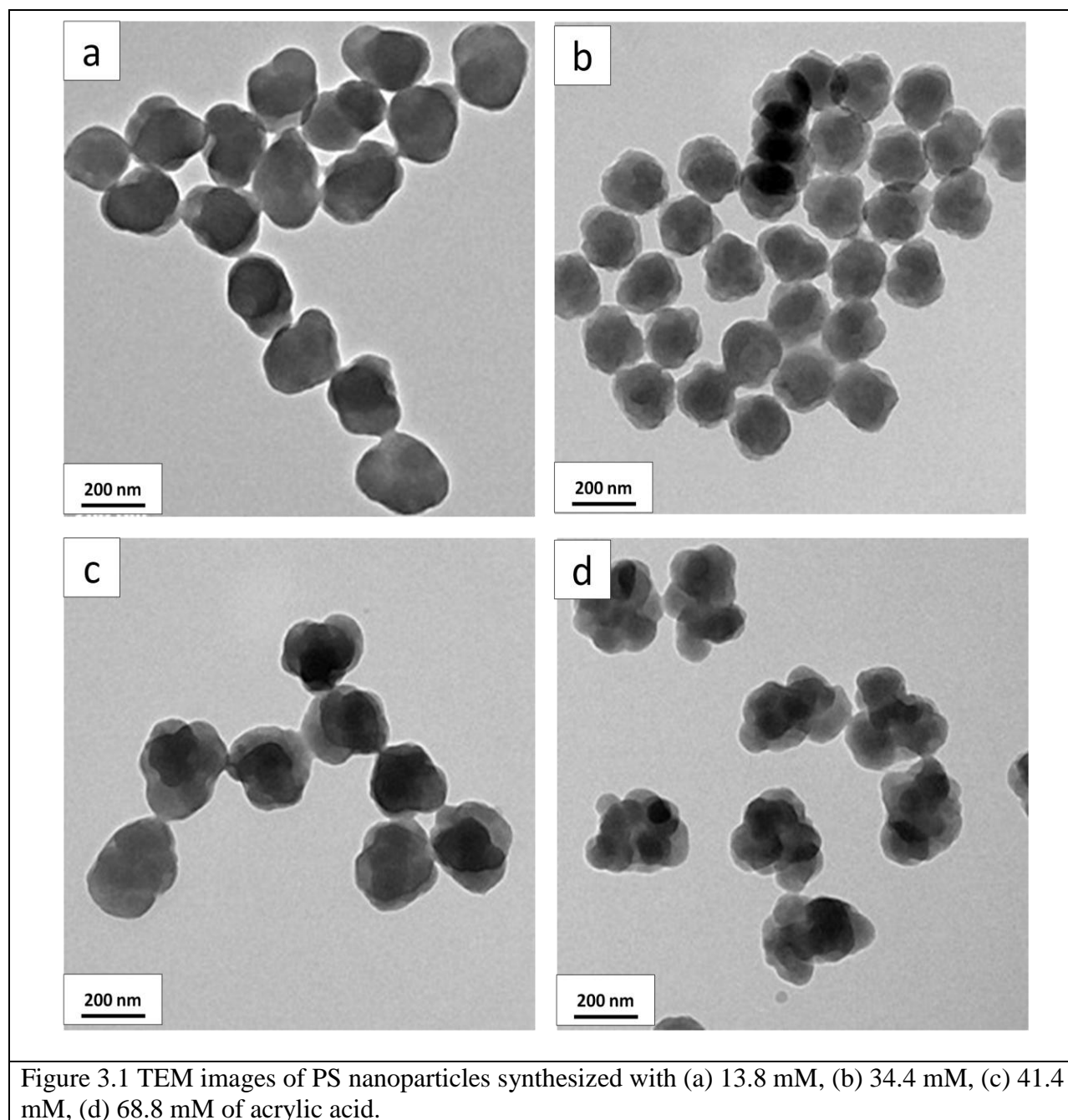
**3.2.7 Fluorescence conjugation on in situ  $Fe_3O_4$  decorated mesoporous silica nanospheres.** First, 5 mg of as-prepared magnetic silica nanospheres was sonically dispersed in 2 ml of PBS. Meanwhile, 5  $\mu$ l of water soluble CdSe/ZnS core/shell quantum dots (8 nM) with 600 nm emission peak and carboxyl functionality was activated with 20 mg EDC in 2 ml of PBS for 15 min, then react with the silica dispersion in a sonication bath for 3 h. The product was then magnetically separated and washed with de-ionized water for multiple times (>5) until the upper clear solution not showing fluorescence under UV lamp. Fluorescence imaging was performed using a digital fluorescence imaging microscopy system that consisted of an inverted fluorescence microscope (Olympus IX70) equipped with a 100-W mercury lamp as a light source.

**3.2.8 Characterizations.** A Carl Zeiss 1530 VP field emission scanning electron microscope (FESEM) and JEOL 2010 LaB6 transmission electron microscope (TEM) at an accelerating voltage of 200kv was used to examine the morphologies and sizes of the particles. Attached EDAX Genesis analyzer energy dispersive spectroscopy (EDS) was used to determine the composition of nanoparticles. ASAP2010 Surface Area Analyzer was applied to measure the pore size distribution of the magnetic porous hollow silica. The magnetic properties were measured with a Quantum Design MPMS-5S SQUID magnetometer. X-ray powder diffraction (XRD) data was obtained on a Philips X'Pert-MPD diffractometer equipped with a graphite monochromator and Cu K $\alpha$  (1.5418 Å) radiation. Surface composition of the samples was examined by Thermo Nicolet Nexus 670 FT-IR machine.

### 3.3 Result and discussion:

In order to achieve MPHSN using polystyrene nanoparticles as a sacrificial template, we proposed a synthesis route as shown in Scheme 3.1. PS particles with carboxyl modification are first synthesized then linked with amine-functionalized Fe<sub>3</sub>O<sub>4</sub> nanoparticles under EDC catalysis. After that, surfactant CTAB guided silica coating can be applied to achieve mesoporous shells with Fe<sub>3</sub>O<sub>4</sub> embedded in it, and both the templates are removed through calcination to obtain the hollow construction.



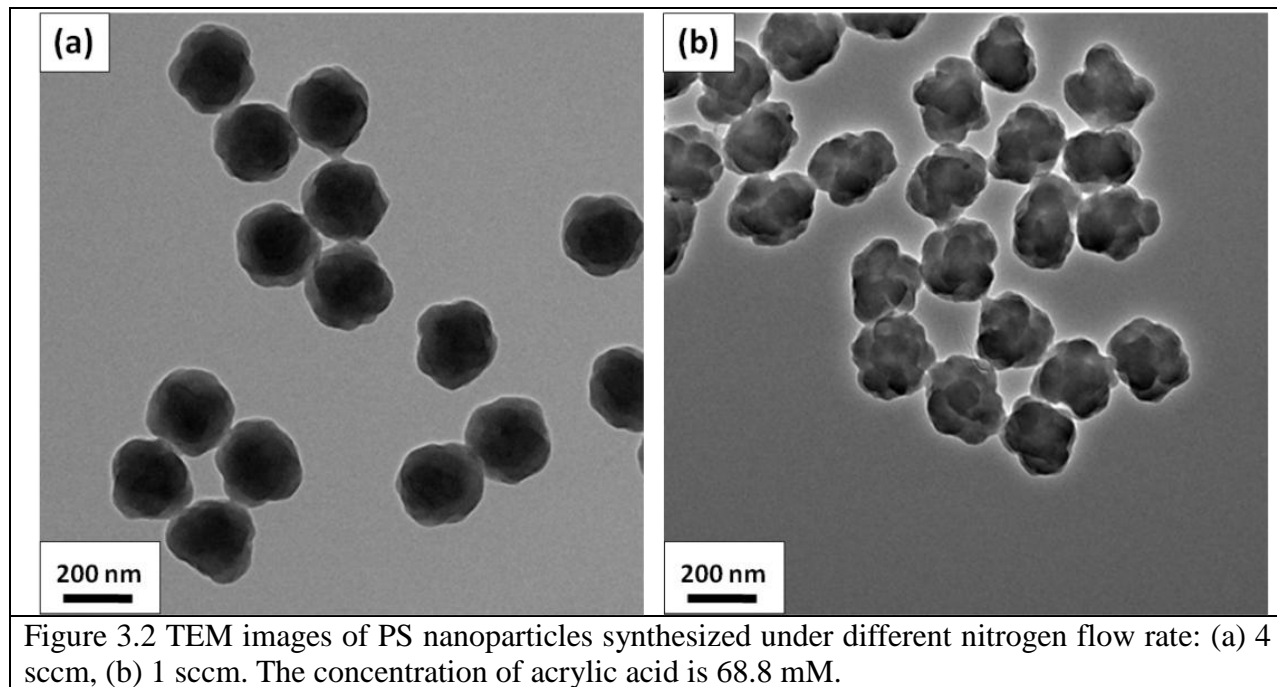


**3.3.1 PS nanoparticle synthesis with acrylic acid as comonomer.** In favor of having functional carboxyl groups on the surface of PS nanoparticles for the purpose of improving dispersity and further modification, a series of syntheses with acrylic acid as the comonomer were also conducted using an emulsifier-free method. Generally, this system consists of styrene as the

monomer, potassium persulfate ( $\text{K}_2\text{S}_2\text{O}_8$ ) as the polymerization initiator, and divinyl benzene as the crosslinker.<sup>18</sup> In addition, water soluble comonomers such as acrylic acid have been used for controlling the size distribution and surface functionality of the particles.<sup>27-29</sup> Also, the surface charge that was introduced by the use of the comonomer would protect the particles from aggregation and increase the mono-dispersity.<sup>18</sup> Herein, different concentrations of acrylic acid were applied in the synthesis.

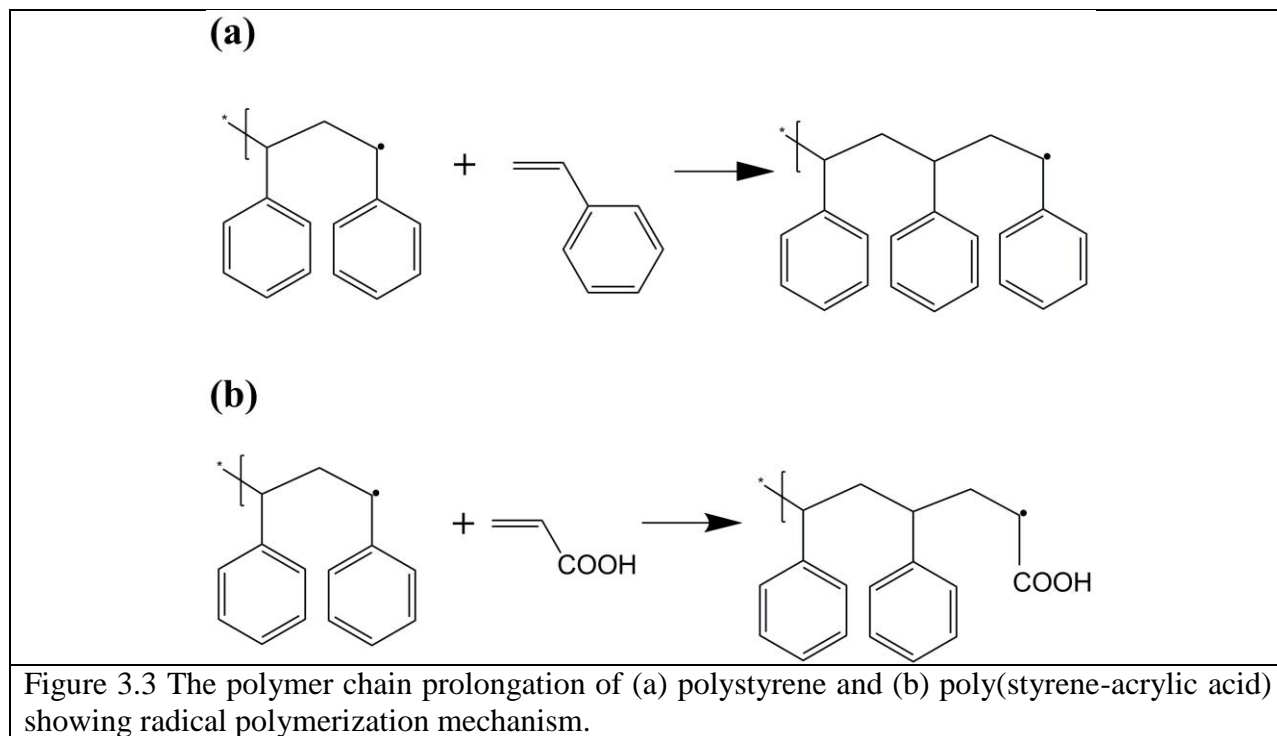
TEM images in Figure 3.1 represent the morphology of the PS nanoparticles obtained in different acrylic acid concentrations, from 13.8 to 68.8 mM. It can be clearly seen that a higher acrylic acid concentration leads to a more irregular surface on the particle. In low concentration (13.8 mM, Figure 3.1 (a)), although the particles are not in ideal spherical shape, the surface tends to be smooth. Also, the existence of a contrast difference within each individual particle indicates the possibility of a two-stage polymerization, in which a core was formed first during the reaction, followed by a second layer of polymerization, and led to a more obviously wrinkled surface as the concentration of acrylic acid increased. According to the cited literature, there are two pathways of PS nanoparticle formation in this emulsifier-free synthesis, one is the droplet formed from the stirring of insoluble monomer, and the other is the monomer that dissolved in the solvent. Before the polymerization was initiated, styrene formed the droplet from the vigorous stirring, while the majority of the acrylic acid was dissolved in water because of good solubility, and a small part of it could be blended in the styrene droplets through diffusion. Upon the injection of the polymerization initiator, the inner part of the particles as seen in TEM images was first formed from the droplets of styrene until nearly depleted during the first several hours. Subsequently, the dissolved acrylic acid started to get more involved and polymerized in the form of either outer layer or small particles that depositing on the surface of styrene

nanoparticles, or even caused crosslinking between smaller particles resulting in the cluster shape as seen in Figure 3.1 (d). The reaction was terminated while all the monomers, styrene and acrylic acid, were consumed eventually.<sup>18,27,30</sup> The final concentration of PS nanoparticles is about 10 mg/ml after the filtration to remove the large agglomerations.



In this synthesis, the flow rate of nitrogen which bubbles into the solution through the entire reaction is also considered as a key factor that influenced the morphology of PS nanoparticles. As seen in Figure 3.2, particles synthesized under higher nitrogen flow rate (4 sccm) possess a smoother, spherical appearance compared to the one under low nitrogen flow rate (1 sccm). To the best of our knowledge, so far there is no published work that has discussed the influence of nitrogen flow rate on the synthesis of PS nanoparticles in the presence of acrylic acid. Based on our limited results, here, we generated a possible explanation. As shown in Figure 3.3, the polymerization of styrene with or without acrylic acid is following a radical polymerization

mechanism.<sup>31,32</sup> Upon a radical becoming available, the carbon-carbon double bond in styrene or acrylic acid breaks to reach the radical and form a new single bond, therefore the polymer chain will grow. As the nitrogen flow bubbles in the reaction mixture, it can be a disturbance factor that delays or blocks the formation of radicals; hence the reaction rate is decreased as the flow rate increases. A slower reaction rate allows each step of the polymer chain prolongation with another acrylic acid or styrene molecule to happen at a more thermodynamic-kinetic-balanced site, which leads to relatively, smooth particle surfaces, while fast reactions drive each polymerization to take place at the closest site, determined primarily by kinetic preference over thermodynamic, which results in irregular particle surfaces. In order to deeply explore the relationship between nitrogen flow rate and PS particle morphology, a more systematic study focused on its thermodynamic and kinetic mechanism of the reaction with the use of a more accurate gas inlet control system will be required.





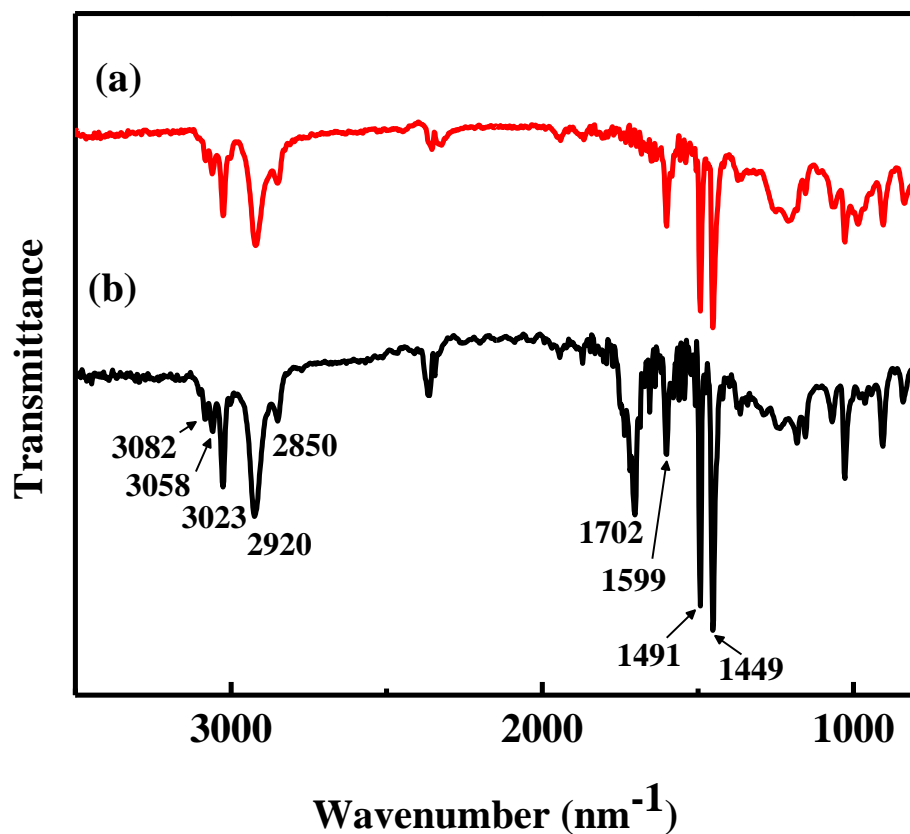


Figure 3.4 FT-IR spectra of (a) plain PS nanoparticle and (b) PS nanoparticles with  $\text{-COOH}$  functionality.

The carboxyl group functionality of the PS nanoparticle was first confirmed by FT-IR as shown in Figure 3.4. The peaks at  $2920\text{ cm}^{-1}$  to  $2850\text{ cm}^{-1}$  region are corresponded to the asymmetric and symmetric  $\text{CH}_2$  stretching, respectively, which is numerous in polymerized styrene. The series of peaks within  $3100\text{-}3000\text{ cm}^{-1}$  region can be assigned to CH stretching in the benzene ring, while the peaks at 1599, 1491 and 1449 represent phenyl nucleus. The most significant difference between Figure 3.4 (a) and (b) is the  $1702\text{ cm}^{-1}$  peak which is attributed to the C=O stretching vibration in the carboxyl group of acrylic acid, therefore implying the successful functionalization of the PS nanoparticles.<sup>33,34</sup>

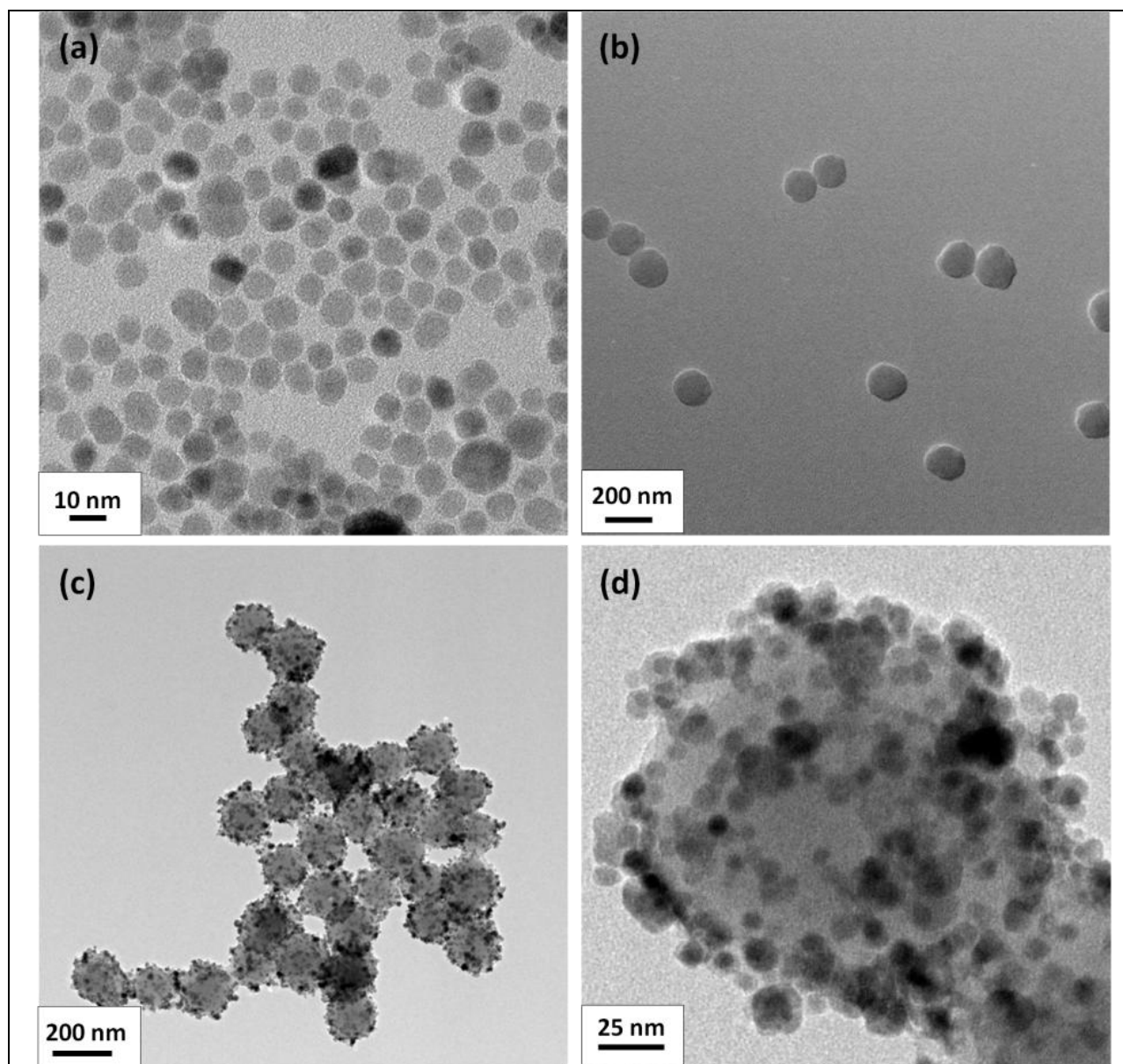
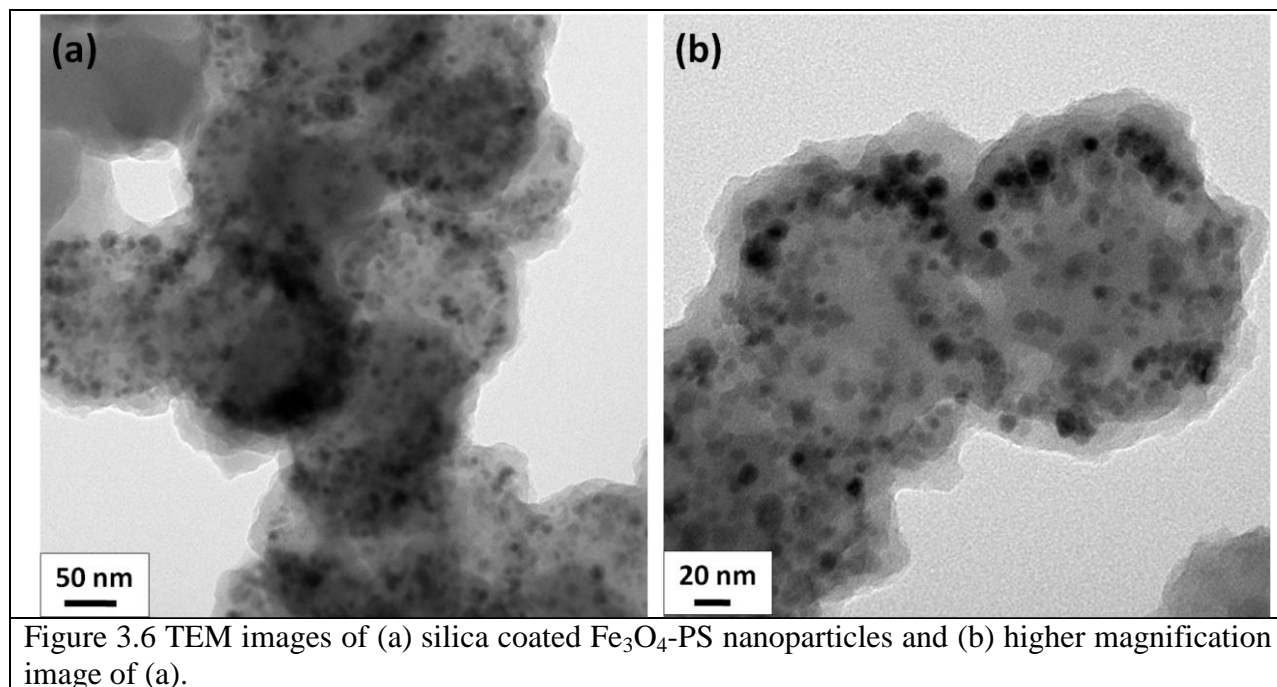


Figure 3.5 TEM images of (a) as-synthesized  $\text{Fe}_3\text{O}_4$  nanoparticles with amine functionality, (b) Carboxyl group modified PS nanoparticles, (c) PS nanoparticles with  $\text{Fe}_3\text{O}_4$  nanoparticles linked on surface, (d) higher magnification image of (c) showing detailed morphology.

**3.3.2 Synthesis of amine-ended  $\text{Fe}_3\text{O}_4$  nanoparticles, linkage to carboxyl-ended PS beads and formation of magnetic porous hollow silica nanospheres (MPHSNs).** To further confirm the present and reactivity of carboxyl group in as-prepared PS nanoparticle, amine-ended  $\text{Fe}_3\text{O}_4$  nanoparticles (shown in Figure 3.5 (a)) with an average diameter of 10 nm were synthesized in polyamine media based on a method published elsewhere,<sup>23</sup> then linked to PS nanoparticles

(shown in Figure (b)) through amine-carboxyl crosslinking under the catalysis of EDC. And this achieved structure can be also used as a template for the synthesis of magnetic hollow silica nanospheres as described in Scheme 3.1. As shown in TEM image in Figure 3.5 (c), the PS nanoparticles are uniformly coated with  $\text{Fe}_3\text{O}_4$  particles, suggesting the carboxyl groups can be utilized in further reactions. However, due to this amine-carboxyl crosslinking, each  $\text{Fe}_3\text{O}_4$  particle can end up with linkages to multiple PS particles; therefore, this may cause massive aggregation. By comparing Figure (b) and (c), the relatively well dispersed PS nanoparticles became linked together to form a large conglomeration. This problem can be further accelerated after the formation of silica shell using the sol-gel method as shown in Figure 3.6. The resulted particles with approximately 20 nm thick silica layer on surface formed a large mass with sizes up to several microns which will be unsuitable for drug delivery application. Therefore, an alternative approach for achieving well dispersed, homogeneous magnetic porous hollow silica nanospheres should be considered.



**3.3.3 In-situ growth of  $Fe_3O_4$  nanoparticles on PS particles.** Since the cross-linking method of connecting  $Fe_3O_4$  and PS nanoparticles is not practical for the preparation of MPHSNs, another approach in which  $Fe_3O_4$  nanoparticles is directly in-situ grown on PS particles is considered. Instead of preparing magnetic nanoparticles beforehand, they can be synthesized and attached to PS particles in a simple one-pot reaction. This idea has been successfully delivered on carbon nanotubes,<sup>35</sup> and may also work well on other organic nanostructure such as PS particles. Through a typical polyol mediate synthesis,<sup>24,36</sup>  $FeCl_2$  and  $FeCl_3$  were used as the precursor to form  $Fe_3O_4$  nanoparticles under basic conditions, in DEG, at an elevated temperature. Because of the melting point of PS (240 °C), the reaction must be carried out at a lower temperature (220 °C) than addressed in the cited literature, which may cause reduced yield and decreased size of  $Fe_3O_4$  nanoparticle. As shown in Figure 3.7, considerable amount of  $Fe_3O_4$  nanoparticles with diameters between 5 to 10 nm were obtained after the synthesis. But instead of forming a homogeneous coating on PS surface as preferred, the magnetic nanoparticles were spreading all over the sample, especially filling in the space between PS particles. And only small portion of the magnetic particles is closely attached to PS surface. This may be explained as a lack of electrostatic attraction<sup>37</sup> or affinity preference driven by surface energy<sup>35</sup> between the anionic carboxyl-modified PS and  $Fe_3O_4$ . It is reasonable and logical to assume that the sample will result in large size mass after silica coating, which is still a derivation from our original goal of magnetic silica drug carriers with good dispersity, so the strategy needs to be reconsidered.

Effort was also made to achieve cationic PS by substituting acrylic acid with allylamine but resulted in aggregated PS particles with no presence of amine functionality, according to FT-IR spectrum study. Although there are other approaches to cationic PS which involve layer-by-layer self-assembling of poly(allylamine hydrochloride) on PS latex, it will cause excessive particle

size increase and mostly used on PS in the micron size range<sup>38</sup>, which is too big for cell intake during drug delivery.

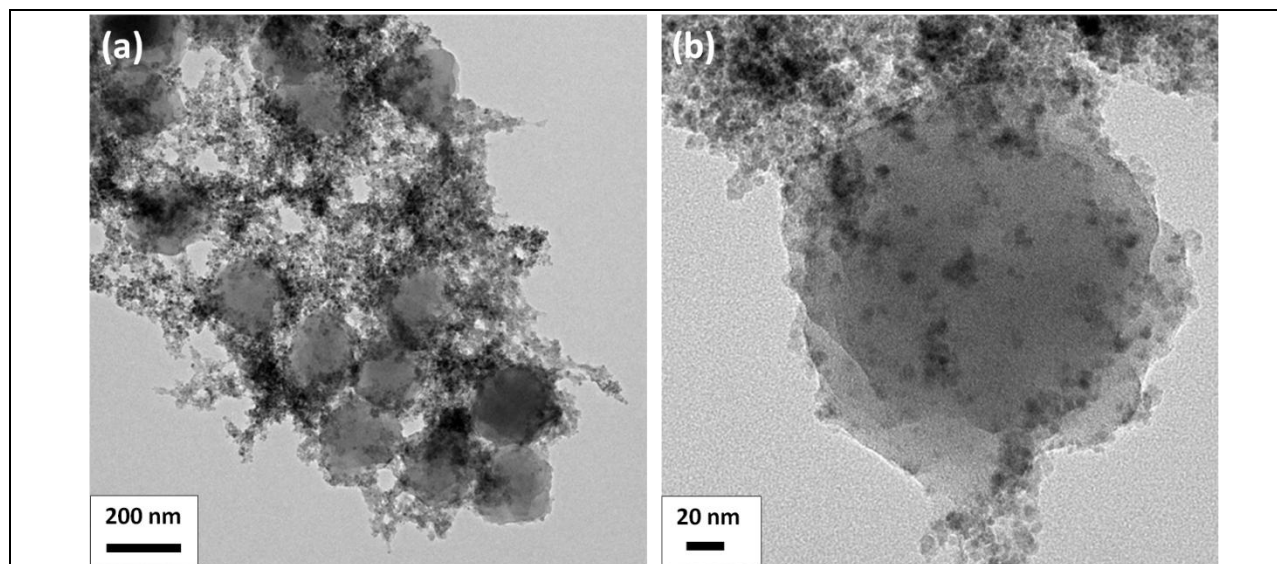
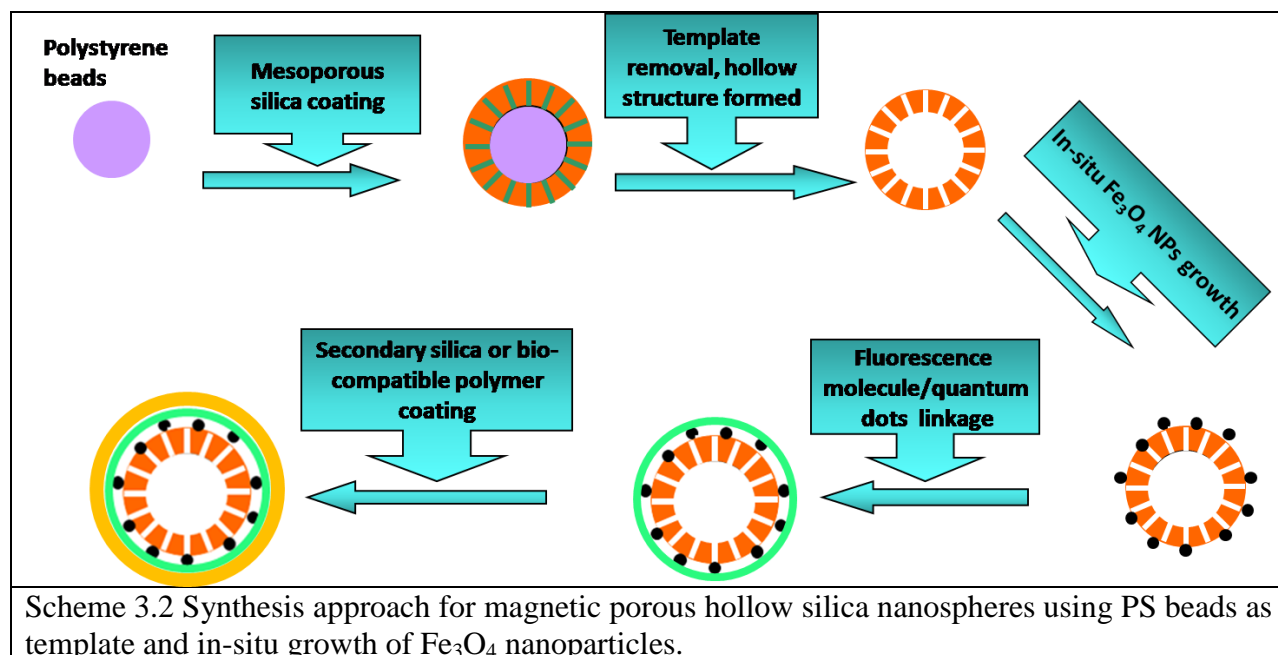


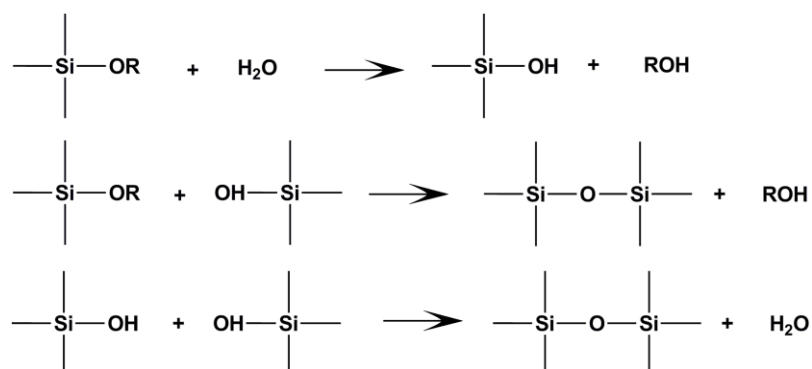
Figure 3.7 TEM images of (a)  $\text{Fe}_3\text{O}_4$  nanoparticles in-situ grown on PS particles, (b) higher magnification of (a) showing surface detail of single PS particle.

**3.3.4 Preparation of mesoporous silica nanospheres based on PS templating.** Since neither crosslinking nor in-situ growth of  $\text{Fe}_3\text{O}_4$  nanoparticles on PS particles would work for synthesizing MPHSN with good dispersity, an alternative route should be taken as described in Scheme 3.2. The PS particles are first coated with mesoporous silica and the template is removed, then the  $\text{Fe}_3\text{O}_4$  nanoparticles are in-situ grown on the silica surface through thermal decomposition of  $\text{Fe}(\text{acac})_3$  in polyamine included reaction media at elevated temperatures. One bonus feature of this method is that the presence of polyamine enabled the synthesized particles to have amine functionality which can be utilized for further modification such as fluorescence linkage. And a secondary mesoporous silica layer or bio-degradable polymer such as polyethylene glycol (PEG) can be applied to reduce the toxicity and increase bio-compatibility.



The coating of silica on PS particles should be considered as a well-established technique that has been addressed in numerous literatures. However, our experience shows that a lot of small technical details, which are easily neglected for unimportance in this process, can be crucial for the success of the experiment, as discussed below.

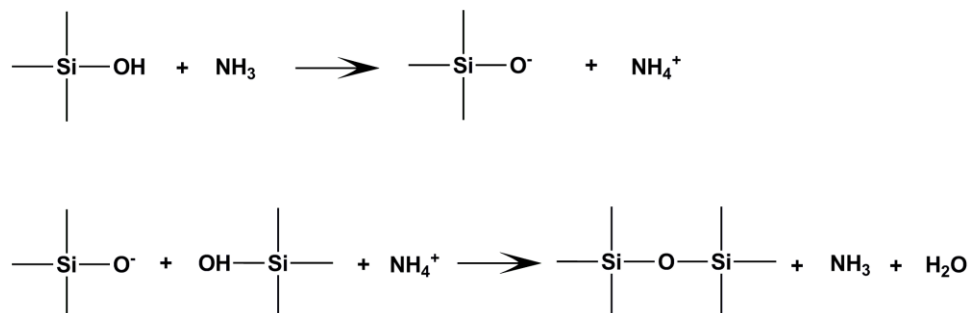
The mechanism of hydrolysis and condensation of alkoxysilane can be described in the following three reactions:<sup>39</sup>



R represents an alkyl group, which is  $\text{CH}_2\text{CH}_3$  in TEOS. Under basic condition, water dissociates to generate hydroxyl anion through a rapid process in order to initiate the first hydrolysis of

alkoxide group (OR), which is generally accepted as the limited step. After that, the hydrolysis of the remaining alkoxide group will be in a spontaneous manner.<sup>39</sup>

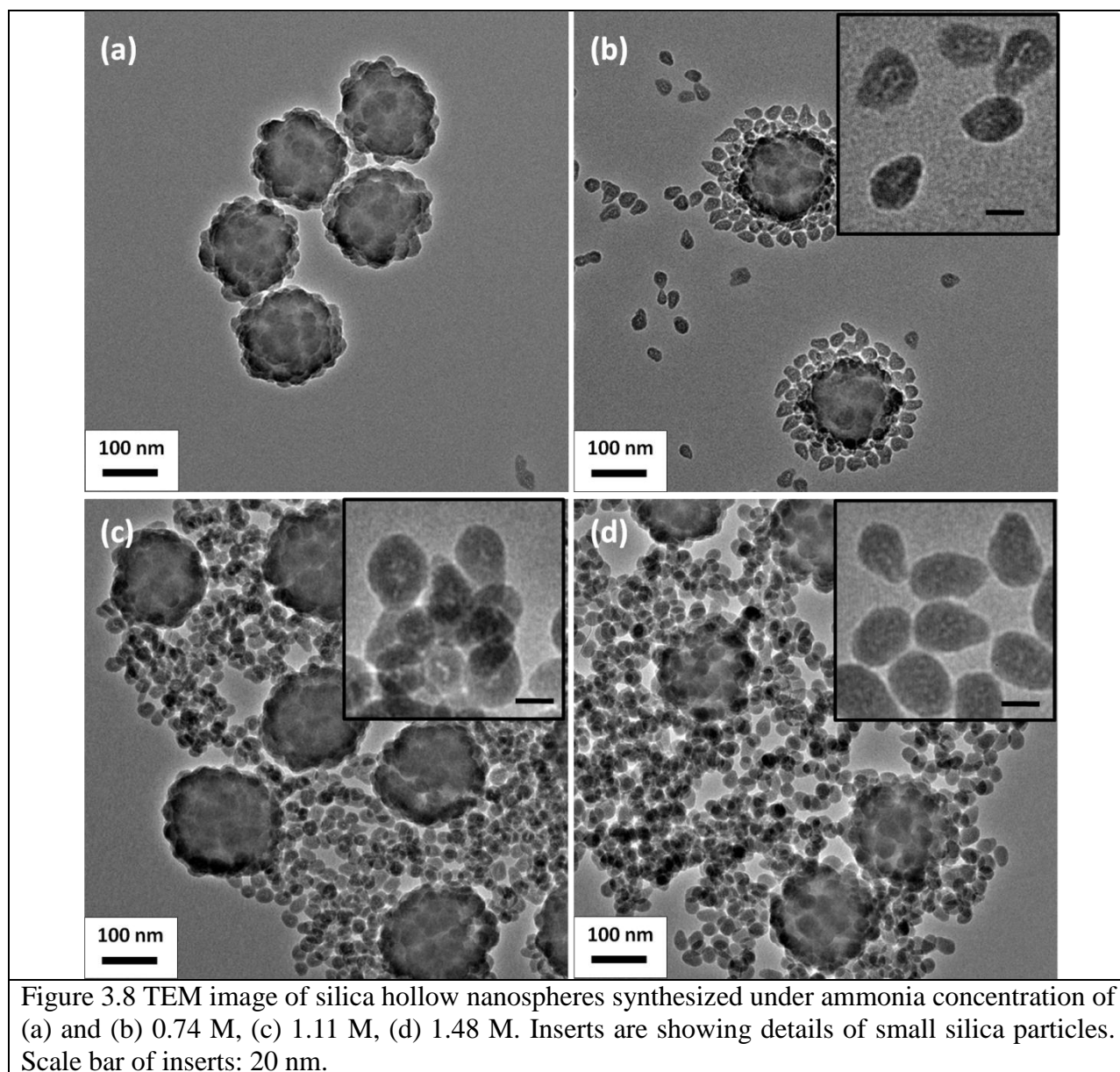
Ammonia is generally used in our experiment to provide the basic condition for the hydrolysis of TEOS. It acts as the catalyst which increases the hydrolysis rate of OR; the mechanism is shown below.<sup>39</sup>



Therefore, in the hydrolysis of alkoxysilane, water amount and pH (in form of ammonia amount) are considered as the key parameters for the formation of amorphous silica. Here, ethanol-only medium as well as an ethanol-water mixture are used in the silica coating on the PS process, and the effect of ammonia, surfactant CTAB, TEOS, temperature and other experimental details will be discussed.

**3.3.4.1 Ethanol-only medium for silica coating on PS nanoparticle.** For the formation of silica shells on certain sacrificial templates, using ethanol-only reaction medium has been a widely applied approach. In this method, ethanol is the majority part as solvent and the limited amount of water comes from the concentrated ammonia solution. Reduced water amounts result in slower hydrolysis and condensation rates of TEOS, which can eventually keep crosslinking and aggregation of the silica product under control.<sup>21,40</sup> In our experiments, PS nanoparticles were first harvested and washed through spin-dialysis, then dispersed in ethanol ultrasonically. Then CTAB was added to form self assembly on PS surface with enough time of stirring, followed by

TEOS injection and mixture was heated to 50 °C. Ammonia was introduced, at last, to trigger the hydrolysis reaction.



First, several syntheses without CTAB were conducted with different amounts of ammonia hydroxide solution, (0.5, 0.75 and 1.0 ml of 14.8 M stock solution), to achieve an ammonia concentration of 0.74, 1.11 and 1.48 M, respectively. As shown in Figure 3.8, instead of forming a homogeneous layer of silica on PS, numerous small silica particles were first generated then



assembled on the PS surface. The possible reason is that TEOS molecules have a low affinity with PS without the present of a proper surfactant, so they only accumulate and hydrolyze within the water droplets generated from stirring which eventually resulted in small silica particles. In the case of lower ammonia and water concentration shown in Figure 3.8 (a) and (b), fewer silica particles were formed due to insufficient basic conditions and water which leads to incomplete hydrolysis of TEOS. In addition to the silica particles coating on PS surface, a multilayer (1~6 layers, observed under TEM microscopy) of well-separated particles was spontaneously arranged around the PS particle, which is an absent phenomenon in synthesis with higher ammonia concentrations, probably due to relatively stronger electrostatic attraction between silica particles that overpowers the ionic strength of the reaction solution with less ammonia added. In higher ammonia concentrations, as shown in Figure 3.8 (c) and (d), more silica particles were formed and aggregated in an irregular manner under higher pH and water concentration.

Besides the effect of ammonia solution, the ultrasonic treatment of PS particle with CTAB in ethanol at the beginning of the experiments was also found to be important for the morphology of the product. PS nanoparticles were first added to ethanol with CTAB and introduced to sonication, then magnetically stirred on hotplate before adding other chemicals and heating. The duration of sonication and stirring was 20 min and 10 min for sample shown in Figure 3.9 (a), and 30 and 20 min for sample in Figure 3.9 (b), respectively, while all the other chemicals and operation remained the same between the two samples. Although the silica shell is not successfully formed on the PS surface, TEM images clearly indicate that longer sonication and stirring treatments result in single shape of small silica nanoparticles while significant amount silica nanorods can be observed with short treatments. Experiment pairs with different CTAB concentration were also performed which yielded a similar results trend. One possible

explanation can be that longer treatment allows CTAB to form more uniform assembly to direct the hydrolysis of TEOS, implying that sufficient time is required for this step in all future experiments, especially in high PS concentration condition.

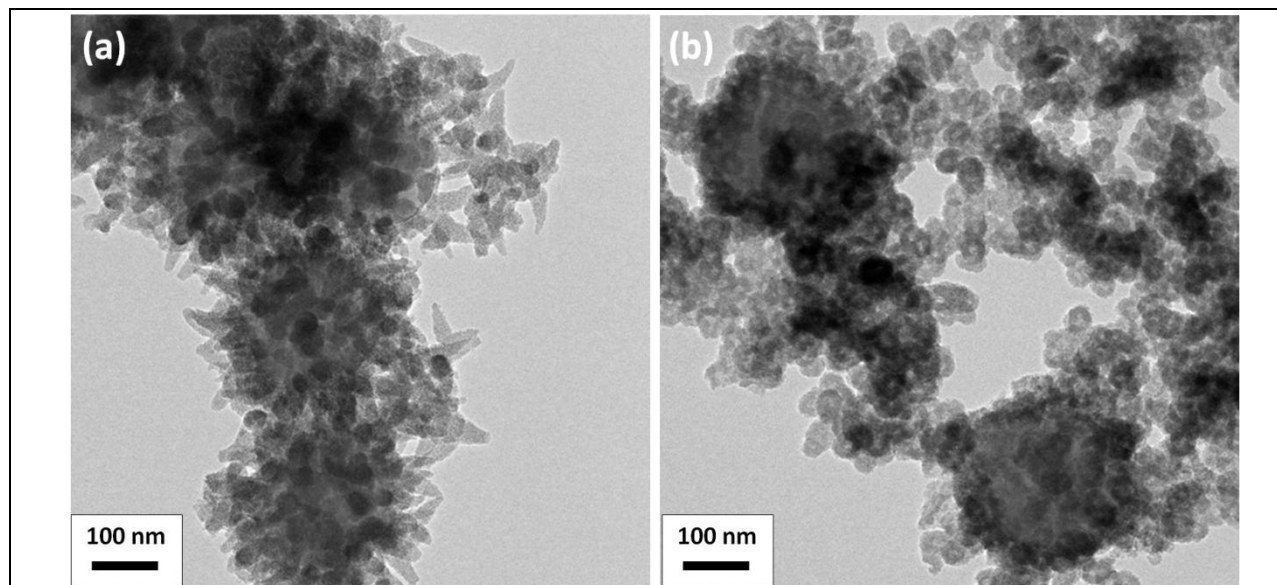


Figure 3.9 TEM image of silica nanospheres synthesized from (a) shorter and (b) longer treatment of sonication and stirring.

**3.3.4.2 Water/ethanol mixed medium for silica coating on PS nanoparticles.** Since using ethanol medium hasn't been successful in our silica coating experiments, a water/ethanol mixed medium is the next candidate. The same water/ethanol ratio (1:4 v/v) as the one for silica coating on  $\text{CaCO}_3$  was applied. Considering the previous experience, the CTAB was stirred together with PS nanoparticles (0.5 mg/ml) for 30 min minimum, and another 20 min after TEOS was added before heating. And the reaction mixture was kept under 50 °C for at least 24 hr to ensure complete hydrolysis and condensation. After calcination, as shown in Figure 3.10, a uniform layer of silica with mesoporous features was formed, suggesting the successful synthesis of mesoporous silica nanospheres with which can proceed to the next step of in-situ  $\text{Fe}_3\text{O}_4$  growth., although this emulsifier-free method provided PS nanoparticles with good dispersity, the yield

from each synthesis (10 mg/ml, 100 ml) is relatively low. Therefore, another approach of PS nanoparticle synthesis using microemulsion method was used to achieve well dispersed particle with higher yield and no surface functionality.

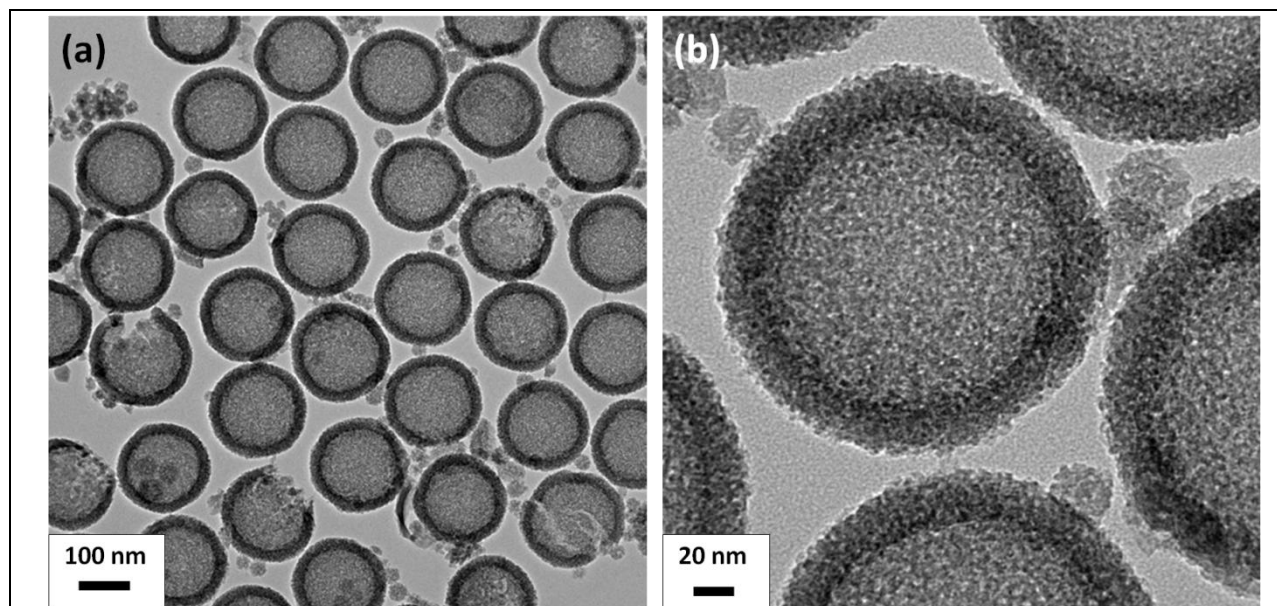
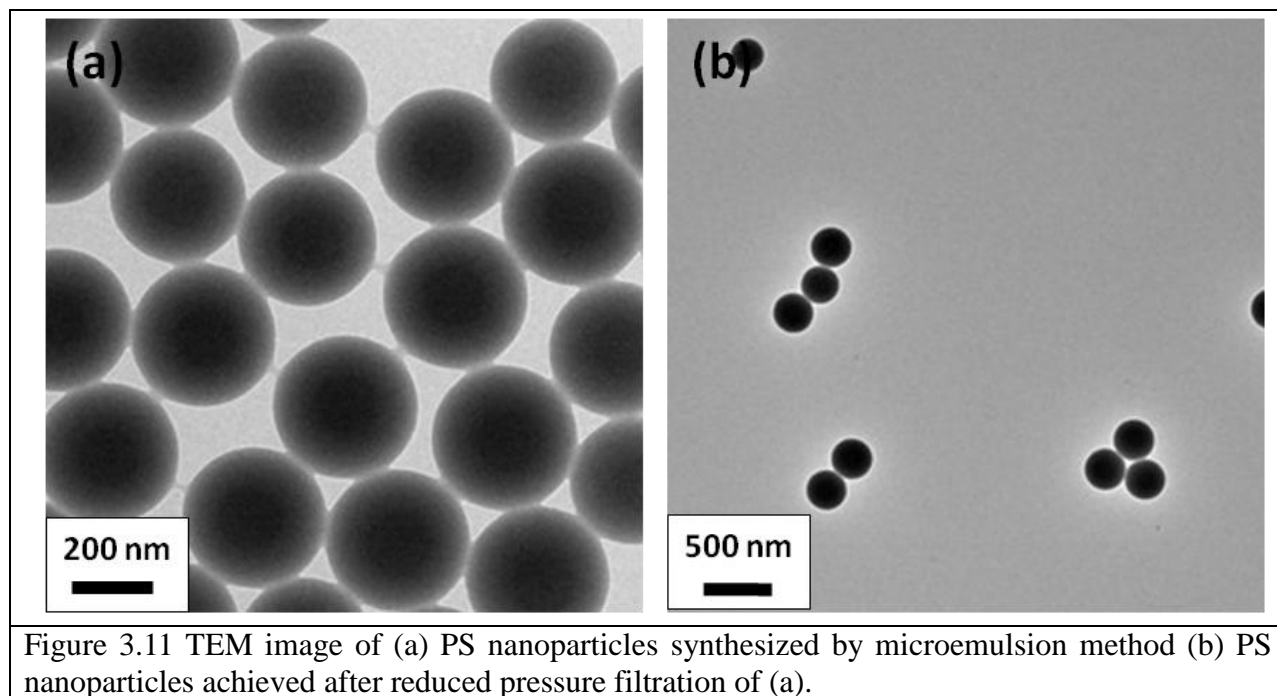


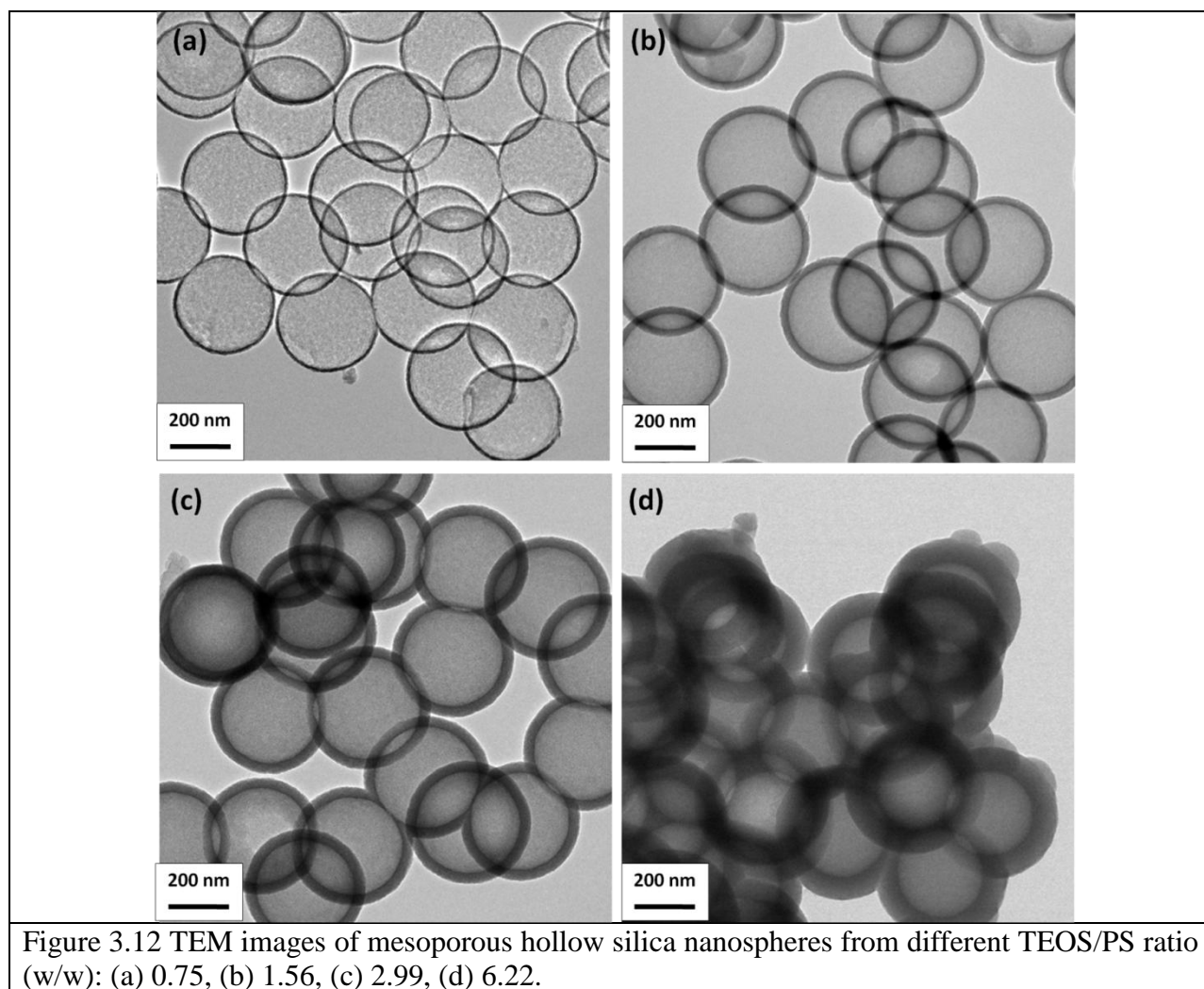
Figure 3.10 TEM images of mesoporous silica nanospheres from water/ethanol ration of 1:4 v/v at (a) low and (b) high magnification.

**3.3.5 Microemulsion method using PVP as stabilizer for preparation of PS beads with large yield.** During the microemulsion synthesis, the stabilizer must possess significant differences in solution property comparing to styrene in order to form the micelle.<sup>41</sup> And polyvinylpyrrolidone (PVP) has been studied and used as a qualified stabilizer in the synthesis of PS nanoparticles for decades. According to the cited literature, PVP40 (average mol wt 40000 ) was selected to synthesized PS nanoparticle with diameter range from 200 to 500 nm, good dispersity and no surface functionality.<sup>20</sup> In a round-bottom flask, styrene was injected in PVP40 aqueous solution under vigorous magnetic stirring and nitrogen purging, then the polymerization inducer was added at an elevated temperature to start the reaction. As shown in Figure 3.11 (a), the resulted PS nanoparticles are not as well dispersed as indicated in the literature, but highly crosslinked,

and sized around 300 nm. We believe the reason of this crosslinking is due to the insufficient force of stirring; since, the micelles formed were not completely separated before the polymerization was triggered. The reduced size of the particles may have been caused by a different flask capacity and stirring conditions from the literature. However, the major aggregated portion of the particles can be removed by allowing the sediment to settle in 2% ethanol and removed through reduced pressure filtration, and the majority of the particles present relatively good dispersity as shown in Figure 3.11 (b). Although there is still some aggregation in a smaller scale (2-3 particles in each cluster), it can be considered as a great improvement compared to the  $\text{CaCO}_3$  nanoparticle templates mentioned in the previous chapter, which makes it a good candidate for the synthesis of hollow silica nanospheres. The theoretical concentration of the PS nanoparticles was 100 mg/ml. But due to the mass loss during filtration, the actual obtained concentration is about 50 mg/ml, which is still high enough for further experiments.



**3.3.6 Mesoporous silica coating on PS nanoparticles.** By using the same method of part 3.3.4.2, mesoporous silica nanospheres were prepared by using a 1:4 (v/v) water/ethanol ratio under heated conditions with tunable shell thickness from 5 to 80 nm as shown in Figure 3.12. The dispersity is much better comparing to the one achieved from  $\text{CaCO}_3$  template in previous chapters. And the yield is good enough due to concentrated PS nanoparticles with easy preparation as a template. The nanosphere with 30-50 nm silica shell was selected for in-situ growth of  $\text{Fe}_3\text{O}_4$  nanoparticles due to medium thickness, relatively good dispersity, and proper resistance against ultrasonic treatment during the synthesis.



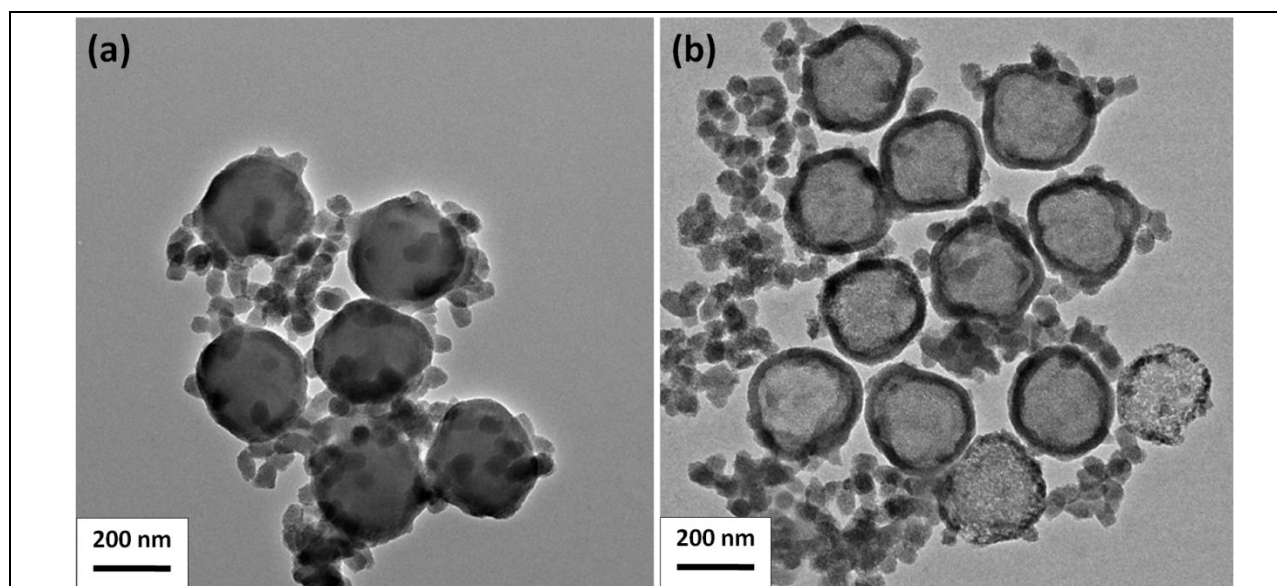


Figure 3.13 TEM images of silica coated PS nanoparticle (a) before and (b) after calcination treatment for template removal.

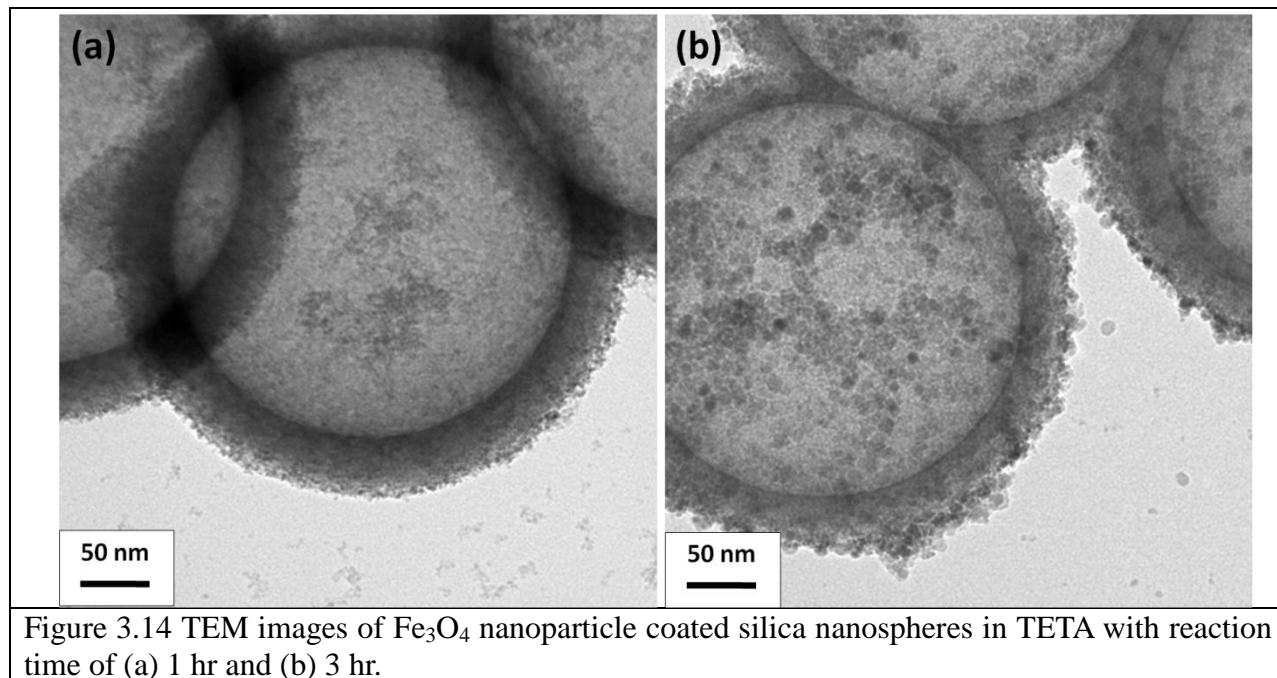
In this silica coating procedure, we also found out that under the absence of TEOS, ammonia hydroxide cannot co-exist with CTAB. No matter which one of these two was added first into the reaction mixture, the addition of the other one will cause visible aggregation of PS particles which turns the lightly milky dispersion of PS to millimeter size pieces in clear solution within one minute. Upon this discovery, the order of chemicals should always be CTAB→TEOS→ammonia, in which ammonia hydroxide is applied last, to simply initiate the hydrolysis of TEOS while all other chemicals and heating condition have been ready. In addition, for the removal of both templates, CTAB and PS, calcination in air can be more convenient and effective than first dissolving away CTAB in refluxing ethanol then organic solvent (toluene, dichloromethane, chloroform, and acetone) treatment for PS removal. The heat during calcination does not damage the morphology and dispersity of the hollow silica nanospheres as we expected.<sup>42-44</sup> To support this point, TEM images of silica coated PS particles before and after 6 hr 600 °C calcination are shown in Figure 3.13. By comparing Figure 3.13 (a) and (b), besides some small silica particles caused by overdosed TEOS, all the hollow silica nanospheres are very

well separated from each other, ignoring the few broken nanospheres, most likely caused by the sonication during TEM sample preparation. The dispersity of the nanospheres is not affected by calcination treatment.

**3.3.7 In-situ growth of  $\text{Fe}_3\text{O}_4$  nanoparticles on mesoporous silica nanospheres, synthesis and XRD study.** As  $\text{Fe}_3\text{O}_4$  nanoparticles can be prepared through thermal decomposition of iron(III) acetylacetonate ( $\text{Fe}(\text{acac})_3$ ) as the precursor in an amine-rich polyamine medium,<sup>23</sup> which serves as the solvent, reducing agent and capping ligand, a similar method was adapted here for the purpose of in-situ growth of  $\text{Fe}_3\text{O}_4$  nanoparticles on the surface of silica nanospheres with amine functionality. The silica nanospheres were, first, dispersed in water under sonication, then mixed with  $\text{Fe}(\text{acac})_3$  and polyamine reaction solvent, and subjected to controlled heating. The first heating segment was set at 120 °C for at least 20 min for complete evaporation of water, then various heating curves were explored to obtain uniform magnetic particle coating with a relatively large particle size and stable superparamagnetism property. The product was washed with acetone using magnetic separation, and then dried under vacuum.

First TETA with boiling point of 266 °C was used as the solvent. After the evaporation of water, the reaction mixture was first heated to 210 °C to start the decomposition of  $\text{Fe}(\text{acac})_3$  then kept at 260 °C for various amounts of time. As seen in the TEM images in Figure 3.14 (a) and (b), a layer of  $\text{Fe}_3\text{O}_4$  nanoparticles were successfully formed on the silica shell, with similar coating density. In addition, it is clear that samples synthesized from longer reaction time (Figure 3.14 (b)) presents  $\text{Fe}_3\text{O}_4$  nanoparticles with larger diameters, therefore stronger superparamagnetism property, compared to the sample from shorter reaction time (Figure 3.14 (a)). Both samples can be easily attracted by bench magnet during the first several cycles of washing, but the magnetic

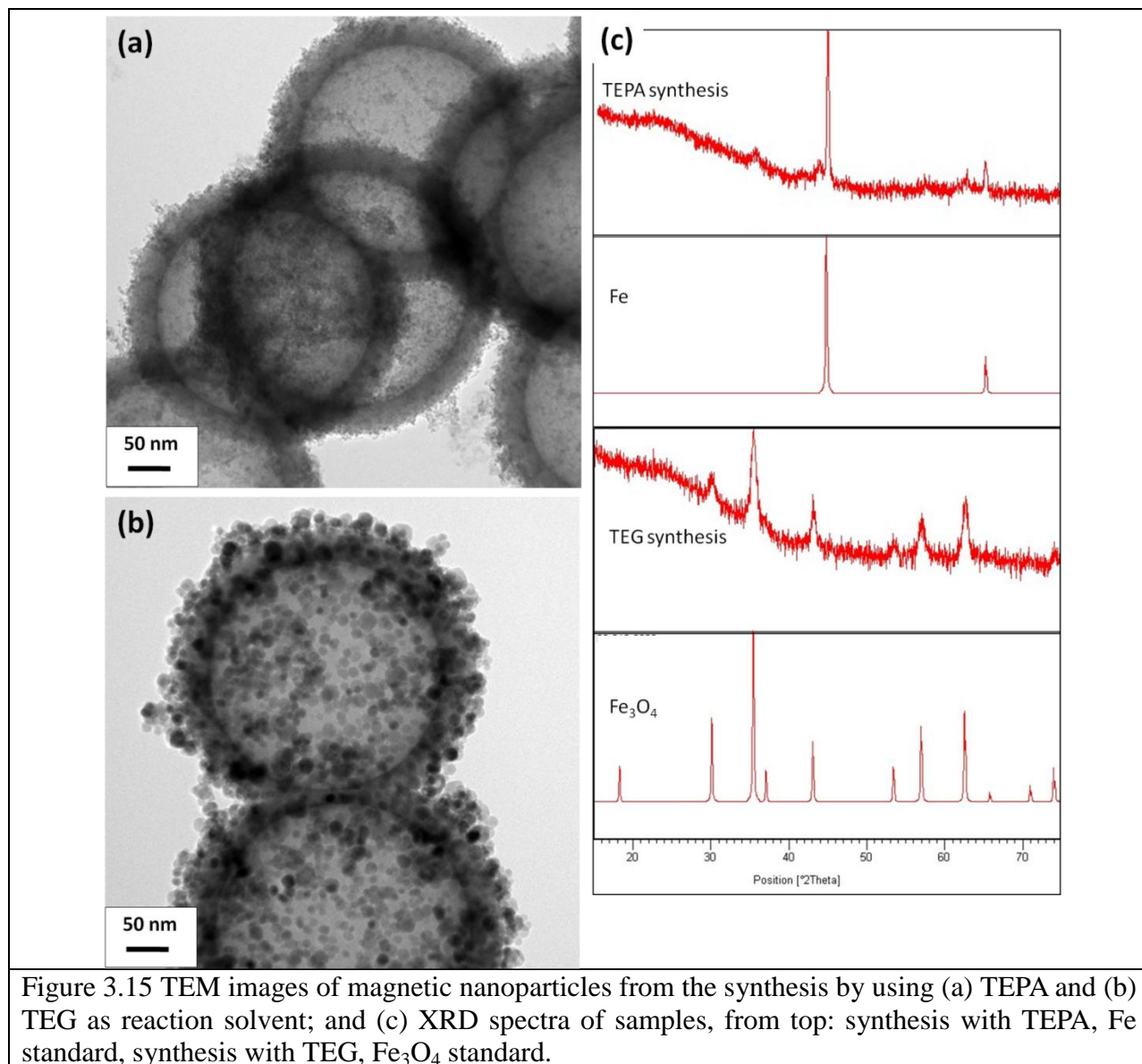
property diminished after being immersed in acetone for more than 24 hr. The XRD spectrum shows no obvious lattice, indicating defective crystals. It may be explained that the reaction temperature is not high enough for complete decomposition of the precursor and formation of indefective  $\text{Fe}_3\text{O}_4$  crystals through TETA reduction. Proper polyamine solvent with higher boiling point shall be required.



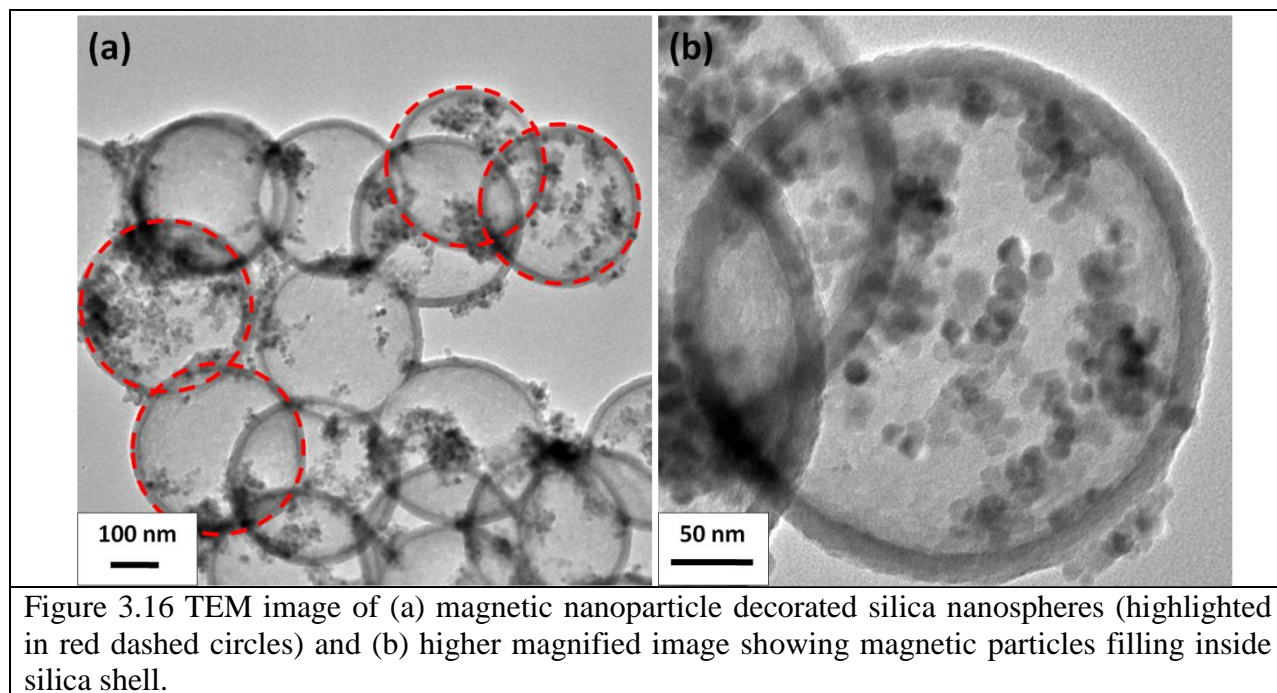
Therefore, TEPA with boiling point of  $340^\circ\text{C}$  and higher density of imine ( $-\text{NH}-$ ) group as reducing agent was then used for the reaction of in-situ  $\text{Fe}_3\text{O}_4$  nanoparticle formation to achieve higher reaction temperature. After 1 hr of reaction under  $300^\circ\text{C}$ , numerous magnetic particles were formed (Figure 3.15 (a)) and the sample can be attracted by a bench magnet after being soaked in acetone for days. However, the XRD spectrum (Figure 3.15 (c)) reflected the majority of the magnetic particles as Fe instead of  $\text{Fe}_3\text{O}_4$ , and will only present ferromagnetism property, which is not preferred for drug delivery purposes. The possible reason can be that the reduction ability of TEPA at  $300^\circ\text{C}$  is so strong that  $\text{Fe}^{3+}$  is directly reduced to  $\text{Fe}^0$  without forming  $\text{Fe}^{2+}$ .



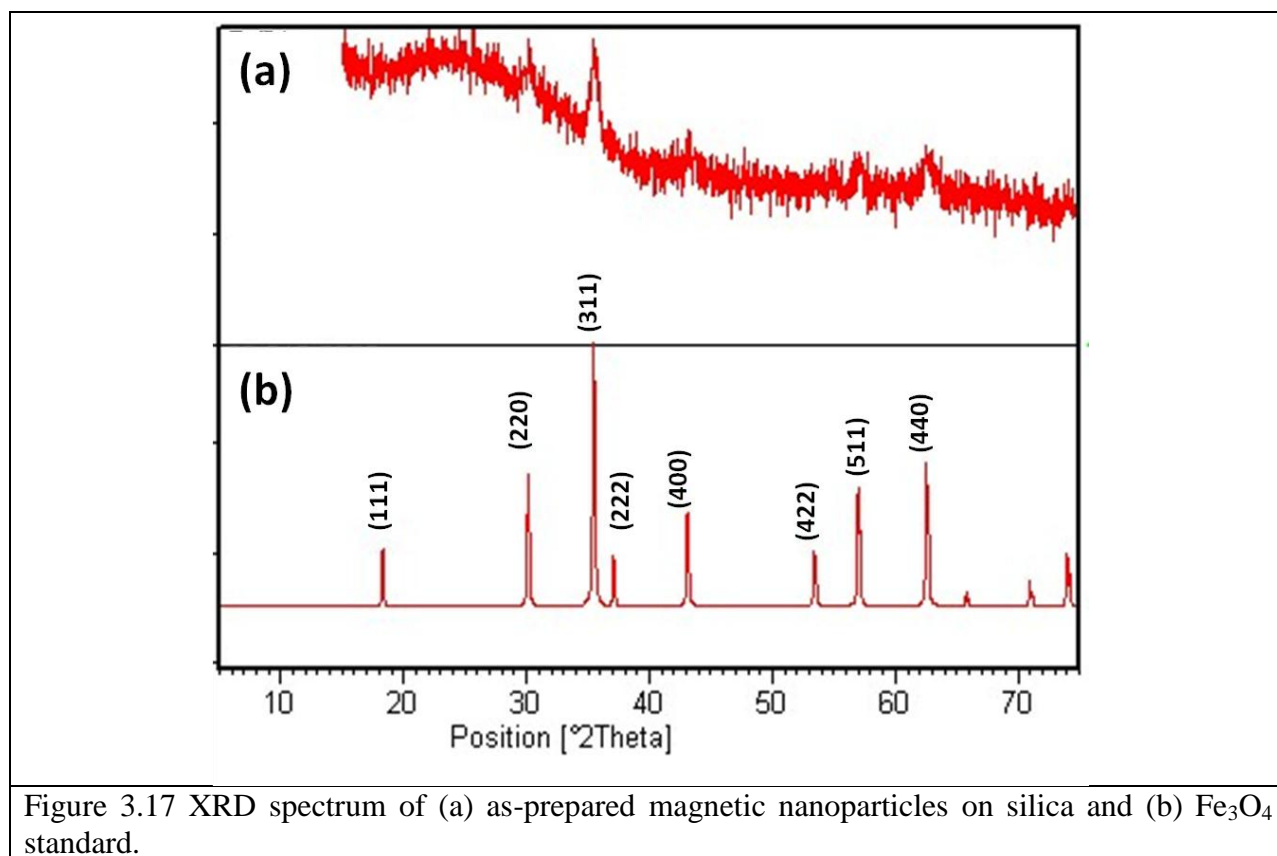
On the another hand, TEG with boiling point 314 °C can also be used for the in-situ growth of magnetic nanoparticles with a much larger diameter (Figure 3.15 (b)) and stable  $\text{Fe}_3\text{O}_4$  crystal structure (Figure 3.15 (c)) through the same experimental procedure at 300 °C. These results inspired the idea of combining the two solvents, TEPA and TEG, in a certain ratio in order to partially weaken the reducing power of TEPA and therefore achieve  $\text{Fe}_3\text{O}_4$  particles with larger diameter and amine functionality.



First, TEPA/TEG=1:1 (v/v) ratio was used and the reaction was kept at 300 °C for 1 hr which only resulted in Fe nanoparticles, confirmed under XRD, indicating not enough dilution of TEPA. By further reducing the proportion of TEPA down to 10~20% (v/v), Fe<sub>3</sub>O<sub>4</sub> particles can be eventually achieved. It was also discovered that the first heating stage, in which was set between 110 °C and 150 °C to allow the evaporation of water, was very important for the yield of magnetic nanoparticles. By increasing time duration of this segment at the temperature which is still not high enough for formation of Fe<sub>3</sub>O<sub>4</sub> nanoparticles, more of the Fe(acac)<sub>3</sub> precursor molecules can be dissolved and integrated to the mesoporous surface of silica, and even diffuse into the hollow space through porous channels and form magnetic particles inside the shell. As seen in Figure 3.16 in which the sample was heated at 120 °C for 3 hr before ramping to the next segment, the outer surface of the silica nanospheres, especially for the highlighted ones, is comparatively smooth while most of the magnetic nanoparticles are filled inside the silica shell.



Meanwhile, a combination of TETA and TEG was also applied to a series of experiments under 280 °C, which is the highest temperature that the mixed solvent can get. The obtained magnetic nanoparticles were confirmed to be  $\text{Fe}_3\text{O}_4$  through XRD. However, due to the same reason of relatively low reaction temperature, the magnetic nanocrystals were defective and the magnetic property was significantly reduced after several days. Thus so far the combination of TEPA and TEG is still the better solvent for in-situ growth of superparamagnetic  $\text{Fe}_3\text{O}_4$  nanoparticles with amine functionality on mesoporous hollow silica nanospheres.



The crystalline structure of as-prepared  $\text{Fe}_3\text{O}_4$  nanoparticles on silica was examined by XRD. By comparing the two spectra in Figure 3.17, the peaks of  $\text{Fe}_3\text{O}_4$  nanoparticles on mesoporous silica nanospheres synthesized from TEPA/TEG combined solvent (a) match the standard

spectrum of  $\text{Fe}_3\text{O}_4$  crystal (b), confirms that the achieved magnetic nanoparticles are indeed  $\text{Fe}_3\text{O}_4$ .

**3.3.8 Magnetic property of as-prepared magnetic hollow silica nanospheres.** The magnetic properties of the silica with in-situ growth of  $\text{Fe}_3\text{O}_4$  nanoparticles were measured by SQUID. Zero-field-cooled (ZFC) and field-cooled (FC) magnetization data were measured in the temperature range of 5–300 K, as shown in Figure 3.18 (a). In the ZFC measurement, the initial field was set to zero when cooling the sample from 300 to 5 K. A field of 50 Oe was applied and the magnetization was measured as the sample was heated from 5 to 300 K. In FC measurement, a field of 50 Oe was applied as the sample was cooled from 300 to 5 K and the magnetization was measured as the sample was heated from 5 to 300 K in the field of 50 Oe. The ZFC curve shows a maximum at 73.3 K, which is the blocking temperature ( $T_B$ ) of the magnetic nanoparticles in the sample. The sample exhibits superparamagnetism properties at temperatures above  $T_B$ , meaning it they can be attracted by a magnetic field but retain no residual magnetism when the magnetic field is removed. To ensure these features, the field-dependent hysteresis loop was measured at room temperature, which is close to the condition that most nano-medicine applications would carry out, as shown in Figure 3.18 (b). The hysteresis loop at 300 K shows a saturation magnetization of 9.78 emu/g (at the field of 20 000 Oe) and absence of coercivity, which confirms superparamagnetic behavior. The absence of coercivity in the hysteresis loop at 300 K indicates a superparamagnetic behavior.

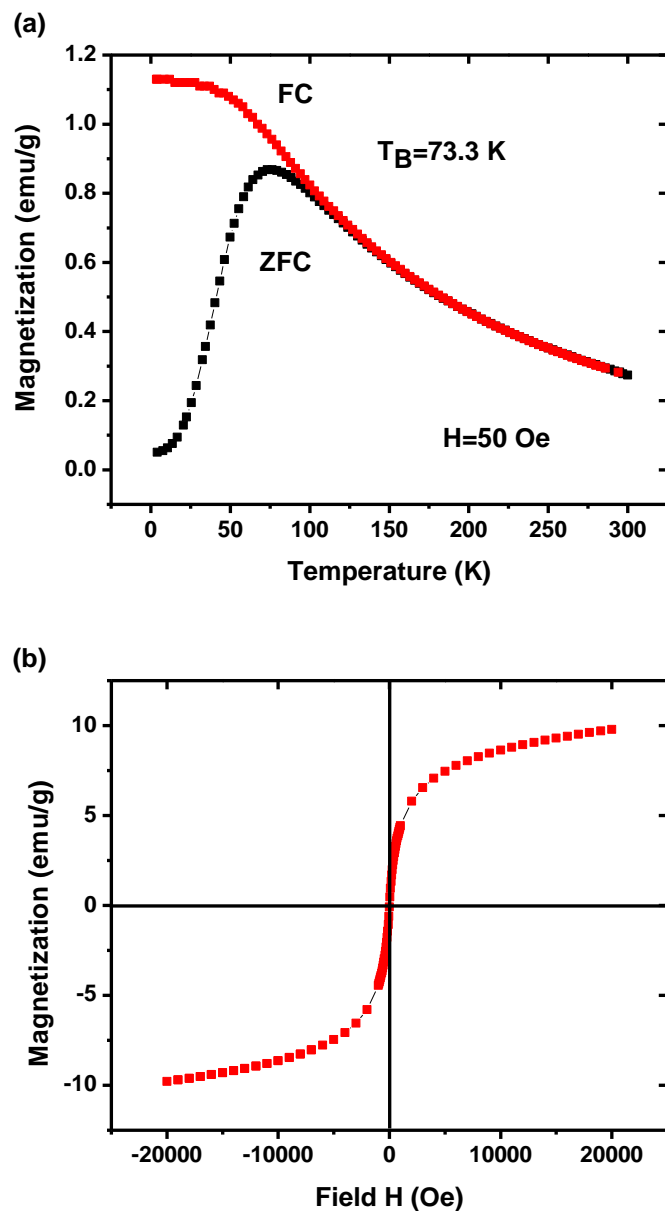
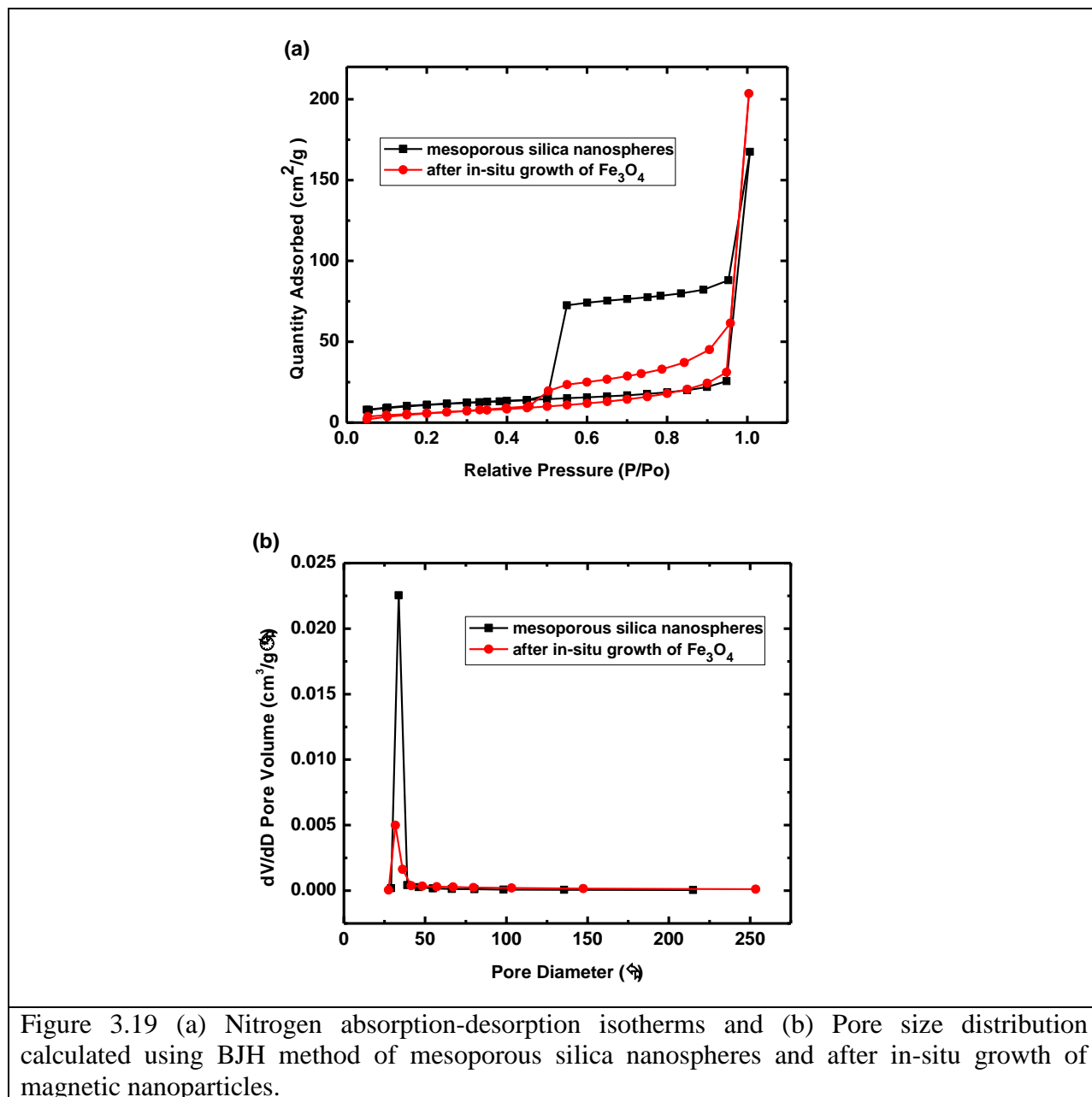


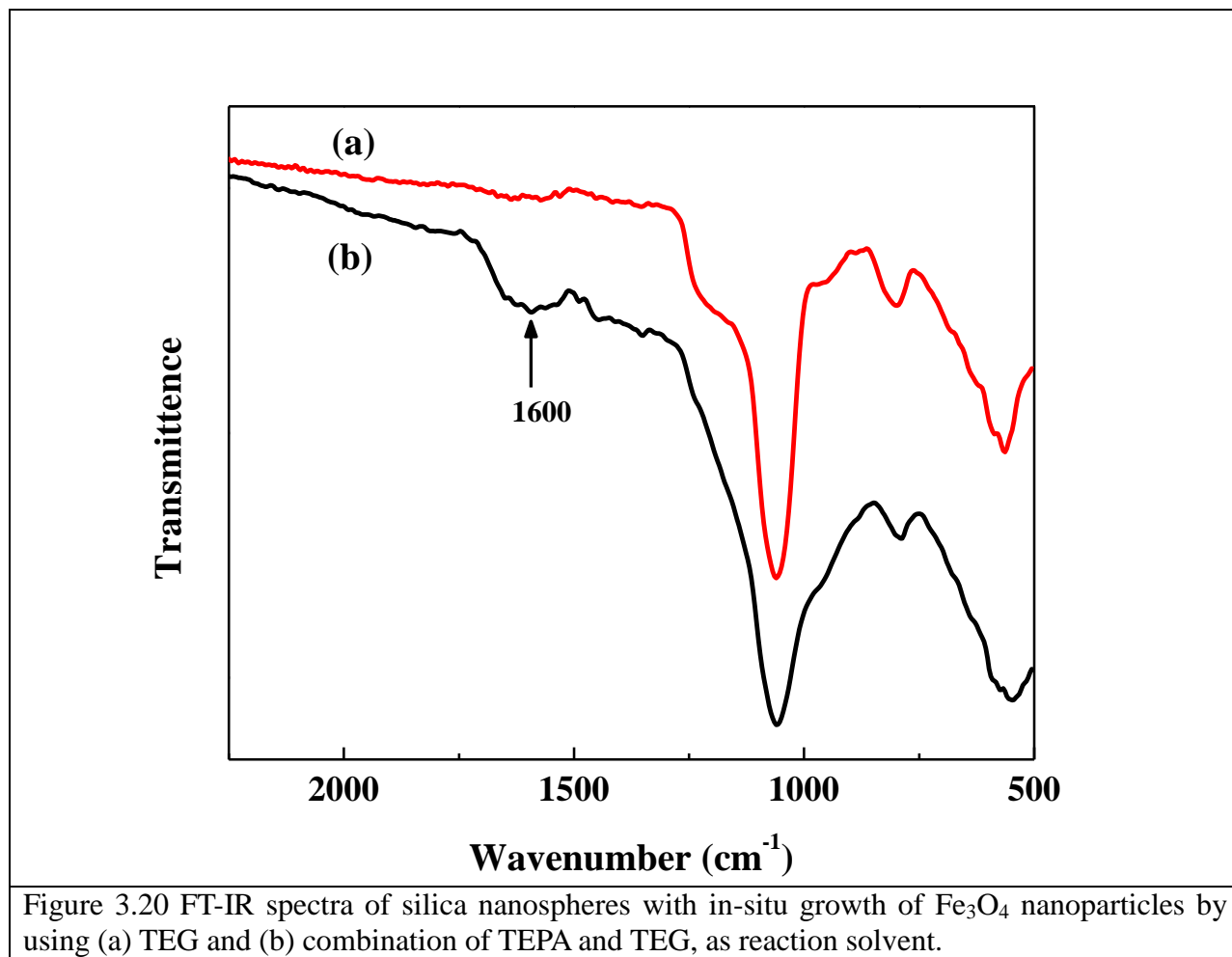
Figure 3.18 Magnetic properties of the Fe<sub>3</sub>O<sub>4</sub> decorated silica: (a) temperature dependence of magnetization at ZFC and FC conditions; (b) hysteresis loops 300 K.

**3.3.9 BET analysis.** Information regarding surface areas and pore volume for the silica nanospheres before and after in situ decoration of Fe<sub>3</sub>O<sub>4</sub> was obtained by measuring N<sub>2</sub> adsorption-desorption isotherms and pore size distribution was calculated by BJH method. As seen in Figure 3.19 (a), both the isotherms have sharp inflection, indicating the sample was able

to maintain a uniform porous structure after the decoration of  $\text{Fe}_3\text{O}_4$ . The loop area is smaller for the sample with  $\text{Fe}_3\text{O}_4$  because the small particles are occupying the porous space on the silica surface and, therefore, reduce the pore volume. Furthermore, the peak pore diameter is 3.37 nm for pure silica nanospheres and 3.17 nm for  $\text{Fe}_3\text{O}_4$ -silica, indicating the BJH pore size distribution in Figure 3.19 (b) shows that the in-situ growth of  $\text{Fe}_3\text{O}_4$  doesn't significantly change the size of the pore, but only reduces porous volume.



**3.3.10 FT-IR spectrum.** The amine functionality of as-prepared silica nanospheres with in-situ growth of  $\text{Fe}_3\text{O}_4$  nanoparticles was confirmed by FT-IR. By comparing the sample synthesized from TEG and TEPA/TEG as shown in Figure 3.20, the peak at  $1600\text{ nm}^{-1}$  is corresponded to the bending vibration of N-H bond,<sup>32,34</sup> confirming the existence of amine group for further modification and functionalization.



**3.3.11 Fluorescence modification using water soluble quantum dots.** Hydrophilic CdSe/ZnS quantum dots with carboxyl functionality were successfully conjugated on the  $\text{Fe}_3\text{O}_4$  decorated mesoporous silica prepared from TEPA/TEG mixed media through carboxyl-amine reaction

under the catalysis of zero-length crosslinker EDC. As shown in Figure 3.21, after thorough washing in order to remove excess and physically adsorbed quantum dots on the MPHSNs, the nanoparticle presents bright fluorescence comparing to the dark background, indicating solid covalent binding between MPHSN and quantum dot, therefore confirms the availability of the amine groups on the magnetic silica after the in situ decoration of  $\text{Fe}_3\text{O}_4$ .

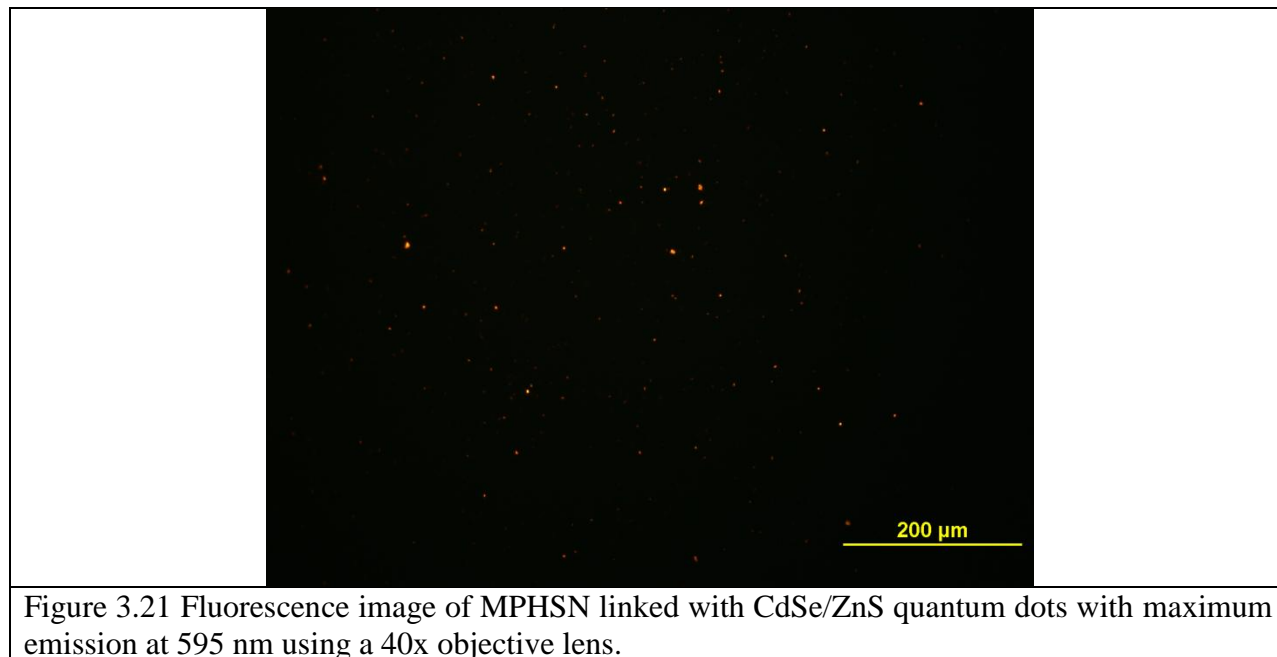


Figure 3.21 Fluorescence image of MPHSN linked with CdSe/ZnS quantum dots with maximum emission at 595 nm using a 40x objective lens.

### 3.4 Conclusion

In this chapter, two different approaches were employed to synthesize magnetic porous hollow silica nanospheres based on PS template for the void interior. Carboxylic functionalized PS nanoparticles were synthesized for the attachment of amine-modified magnetite nanoparticles, followed by mesoporous silica coating and template removal. In the other approach, hollow mesoporous silica nanospheres were first prepared based on PS templating and in situ growth of magnetite nanoparticles was successfully achieved using thermal decomposition of organic iron precursor in polyamine/polyalcohol mixed media. After this convenient, one-pot synthesis, the resulted product exhibited good superparamagnetism properties and available amine groups for



further functionalization, such as fluorescence conjugation using quantum dots, indicating promising potential for multi-functional drug delivery and imaging.

### 3.5 References

- (1) Lu, A.-H.; Salabas, E. L.; Schüth, F. *Angew. Chem. Int. Ed.* **2007**, *46*, 1222.
- (2) Yang, P.; Gai, S.; Lin, J. *Chem. Soc. Rev.* **2012**, *41*, 3679.
- (3) Tang, F.; Li, L.; Chen, D. *Adv. Mater.* **2012**, *24*, 1504.
- (4) Feng, J.; Song, S.-Y.; Deng, R.-P.; Fan, W.-Q.; Zhang, H.-J. *Langmuir* **2009**, *26*, 3596.
- (5) Gai, S.; Yang, P.; Ma, P. a.; Wang, D.; Li, C.; Li, X.; Niu, N.; Lin, J. *J. Mater. Chem.* **2011**, *21*, 16420.
- (6) Feng, J.; Fan, W.-Q.; Song, S.-Y.; Yu, Y.-N.; Deng, R.-P.; Zhang, H.-J. *Dalton Transactions* **2010**, *39*, 5166.
- (7) Zhao, W.; Chen, H.; Li, Y.; Li, L.; Lang, M.; Shi, J. *Adv. Funct. Mater.* **2008**, *18*, 2780.
- (8) Liu, J.; Qiao, S. Z.; Budi Hartono, S.; Lu, G. Q. *Angew. Chem. Int. Ed.* **2010**, *49*, 4981.
- (9) Zhu, Y.; Fang, Y.; Kaskel, S. J. *Phys. Chem. C* **2010**, *114*, 16382.
- (10) Huang, S.; Yang, P.; Cheng, Z.; Li, C.; Fan, Y.; Kong, D.; Lin, J. *J. Phys. Chem. C* **2008**, *112*, 7130.
- (11) Martín-Saavedra, F. M.; Ruiz-Hernández, E.; Boré A.; Arcos, D.; Vallet-Regí M.; Vilaboa, N. *Acta Biomater.* **2010**, *6*, 4522.
- (12) Yiu, H. H. P.; Niu, H.-j.; Biermans, E.; van Tendeloo, G.; Rosseinsky, M. J. *Adv. Funct. Mater.* **2010**, *20*, 1599.
- (13) Giri, S.; Trewyn, B. G.; Stellmaker, M. P.; Lin, V. S. Y. *Angew. Chem. Int. Ed.* **2005**, *44*, 5038.
- (14) Lee, J.-H.; Jun, Y.-w.; Yeon, S.-I.; Shin, J.-S.; Cheon, J. *Angew. Chem. Int. Ed.* **2006**, *45*, 8160.
- (15) Lee, J. E.; Lee, N.; Kim, H.; Kim, J.; Choi, S. H.; Kim, J. H.; Kim, T.; Song, I. C.; Park, S. P.; Moon, W. K.; Hyeon, T. *J. Am. Chem. Soc.* **2009**, *132*, 552.
- (16) Lee, J. E.; Lee, D. J.; Lee, N.; Kim, B. H.; Choi, S. H.; Hyeon, T. *J. Mater. Chem.* **2011**, *21*, 16869.
- (17) Chang, C. H.; Son, P. S.; Yoon, J.-A.; Choi, S.-H. *J. Nanomater.* **2010**, 2010.
- (18) Dong, H.; Lee, S.-Y.; Yi, G.-R. *Macromol. Res.* **2009**, *17*, 397.
- (19) Hsiao, S.-C.; Ou, J.-L.; Sung, Y.; Chang, C.-P.; Ger, M.-D. *Colloid. Polym. Sci.* **2010**, *288*, 787.
- (20) Qi, G.; Wang, Y.; Estevez, L.; Switzer, A. K.; Duan, X.; Yang, X.; Giannelis, E. P. *Chem. Mater.* **2010**, *22*, 2693.
- (21) Yuan, J.; Wan, D.; Yang, Z. *J. Phys. Chem. C* **2008**, *112*, 17156.
- (22) Li, J.-M.; Ma, W.-F.; Wei, C.; Guo, J.; Hu, J.; Wang, C.-C. *J. Mater. Chem.* **2011**, *21*, 5992.
- (23) Qu, H.; Ma, H.; Riviere, A.; Zhou, W.; O'Connor, C. J. *J. Mater. Chem.* **2012**, *22*, 3311.
- (24) Feldmann, C.; Jungk, H.-O. *Angew. Chem. Int. Ed.* **2001**, *40*, 359.
- (25) Maity, D.; Kale, S. N.; Kaul-Ghanekar, R.; Xue, J.-M.; Ding, J. *J. Magn. Magn. Mater.* **2009**, *321*, 3093.

- (26) Wan, J.; Cai, W.; Meng, X.; Liu, E. *Chem. Commun.* **2007**, 5004.
- (27) Wang, P. H.; Pan, C. Y. *Colloid. Polym. Sci.* **2002**, 280, 152.
- (28) Musyanovych, A.; Rossmanith, R.; Tontsch, C.; Landfester, K. *Langmuir* **2007**, 23, 5367.
- (29) Holzapfel, V.; Musyanovych, A.; Landfester, K.; Lorenz, M. R.; Mailänder, V. *Macromol. Chem. Phys.* **2005**, 206, 2440.
- (30) Yamamoto, T.; Nakayama, M.; Kanda, Y.; Higashitani, K. *J. Colloid Interface Sci.* **2006**, 297, 112.
- (31) Pojman, J. A.; Willis, J.; Fortenberry, D.; Ilyashenko, V.; Khan, A. M. *J. Polym. Sci., Part A: Polym. Chem.* **1995**, 33, 643.
- (32) McMurry, J. *Organic Chemistry*; Fifth ed.; Brooks/Cole, 2000.
- (33) Silverstein, R. M.; Webster, F. X. *Spectrometric identification of organic compounds*; 6th ed.; John Wiley & Sons, Inc., 1997.
- (34) Nakannishi, K. *Infrared absorption spectroscopy - practical*; Holden-Day, Inc., San Francisco and Nankodo Company Limited, Tokyo, 1962.
- (35) Wan, J.; Cai, W.; Feng, J.; Meng, X.; Liu, E. *J. Mater. Chem.* **2007**, 17, 1188.
- (36) Cai, W.; Wan, J. *J. Colloid Interface Sci.* **2007**, 305, 366.
- (37) Gao, C.; Li, W.; Morimoto, H.; Nagaoka, Y.; Maekawa, T. *J. Phys. Chem. B* **2006**, 110, 7213.
- (38) Kato, N.; Schuetz, P.; Fery, A.; Caruso, F. *Macromolecules* **2002**, 35, 9780.
- (39) Chen, S.-L.; Dong, P.; Yang, G.-H.; Yang, J.-J. *Industrial & Engineering Chemistry Research* **1996**, 35, 4487.
- (40) Cao, S.; Jin, X.; Yuan, X.; Wu, W.; Hu, J.; Sheng, W. *J. Polym. Sci., Part A: Polym. Chem.* **2010**, 48, 1332.
- (41) Antonietti, M.; Heinz, S.; Schmidt, M.; Rosenauer, C. *Macromolecules* **1994**, 27, 3276.
- (42) Lee, K. K.; Kang, Y. C.; Jung, K. Y.; Kim, J. H. *J. Alloys Compd.* **2005**, 395, 280.
- (43) Cui, H.; Zayat, M.; Levy, D. *J. Sol-Gel Sci. Technol.* **2007**, 41, 313.
- (44) Balencie, J.; Levy, L.; Hocheplied, J. F. *Mater. Chem. Phys.* **2008**, 112, 546.

## **Part II: Semiconductive nanostructure for biosensor application**

### **Chapter IV: Introduction**

During the latest years, the demand of prompt and accurate detection method for biological molecule has become more and more significant for the purpose of biological study, medicine application and safety inspection. Numerous of conventional methods have been developed and used for detection and analysis of molecules such as DNA, enzyme, structural protein and lipid for decades, but with drawbacks of high equipment expense, long analysis time or sensitivity limitation. Meanwhile, since most of the biological molecules and complex are in nanometer scale, the studies of nanomaterials and biology/biomedicine have been sharing a lot of common interest and interaction with each other, therefore the new class of nano-biosensor is being derived. As being within the same size range, nanomaterials based sensing devices are more capable of picking up the signal of biological analyte with higher sensitivity upon contact, thank to the high surface-to-volume ration. Also, the vast development of nanoscience and nanotechnology has built solid foundation for designing the nanomaterial and device structure to suit our need for the detection of different analyte. So far, nanomaterials based biosensor has been an extremely active research field in the past decade that various nanomaterials, including nanowire, nanoparticle and other more sophisticated combined structure, are employed for the detection of biological materials through different pathways according to their structure and function, and generate various formats of output signal simultaneously, including magnetic, fluorescent, electrochemical and so on. Among all the materials, semiconductive nanowire with field-effect property is one of the most frequently studied candidates for biosensing detection

based on electric signal generated from biological molecules with charge. The device is immobilized on circuit chip with highly designable structure and easy for handling and observation. Also, the integration with microfluidic channel makes it more convenient for the detection of solution/dispersion samples, and therefore greatly enhances the potential for practical application.

In this chapter, a comprehensive introduction of biosensors based on nanomaterials is provided, categorized by material structures including nanoparticle and nanowire. First several nanoparticle base biosensors are introduced. Then we focus on semiconductive nanowire field-effect transistors for biosensor in the aspects of different materials and their modification as well as applications in biosensing.

## **4.1 Nanoparticles based biosensors**

The applications of nanoparticles for biosensors have been extensively studied, including fluorescence, colorimetric, electrochemical sensing and so on. Besides, there are numerous works about fabrication of multifunctional platform that combines the feature of drug delivery, bio-targeting and sensing, fluorescence imaging, and even magnetic property all together in single nanoparticle, but will be beyond the content of this chapter.

### **4.1.1 Fluorescence sensing**

Quantum dots are semiconductive nanocrystals with size below 10 nm and high quality fluorescence property. Comparing to conventional organic fluorescent dyes, quantum dots have been famous for the easy excitation, tunable, narrow and symmetric emission spectrum<sup>1</sup>, which are all preferable character for serving as fluorescence probe in bio-detection. One of the earliest

reported works of using nanomaterials for bio-sensing purpose was reported in 1998. Both Nie<sup>2</sup> and Alivisatos's<sup>3</sup> groups used different color emitting core-shell quantum dots conjugated with selected surface functionality to detect the location of targeted protein through either electrostatic force/hydrogen bond or ligand-receptor interactions such as biotin-avidin and antibody-antigen, and multicolor dye images under single excitation were presented. These studies exhibited the outstanding advantage of quantum dots for fluorescence labeling and detection, also demonstrated the photochemical stability of quantum dot in biological environment. As water solubility being vital for biological application, the as-prepared hydrophobic quantum dot was converted to hydrophilic by silica coating<sup>3</sup> or mercaptoacetic acid capping<sup>2</sup> to increase biocompatibility. Soon the research of quantum dot bio-labeling has been developing significantly, majorly focused on the surface functionalization that is adaptable to the target molecules while enhancing biological buffer compatibility of the quantum dots, including ligand exchange<sup>4</sup> and amphiphilic polymer encapsulation<sup>5</sup> after which further functionality will take place through crosslinkers to complete bio-molecule modification. So far, quantum dot has been conjugated with antibody and peptide for the imaging and detection of virus infection,<sup>6</sup> cancer cell<sup>5,7,8</sup> and cell membrane proteins.<sup>9,10</sup> In addition, ssDNA-quantum dots conjugation has been widely explored for fluorescence resonance energy transfer (FRET) biosensor<sup>11-13</sup> in which hybridization of the targeted DNA triggers the fluorescence of quantum dots that is originally quenched.

However, being highly capable of different surface functionalization also presents drawback for bio-sensing application. Since quantum dot is multivalent which means the category and number of linked molecules varies, it is hard to control the stoichiometry, orientation and conformation of the conjugation. So the relationship between analyte concentration and output

signal strength is difficult to determine. Therefore it is more suitable for qualitative imaging rather than quantitative sensing and analysis.<sup>14</sup>

#### **4.1.2 Colorimetric sensing**

The principle of colorimetric sensor is the recognizable color change of metal nanoparticle, mostly gold or silver, under different aggregation states.<sup>15,16</sup> Metal nanoparticles are first linked with either oligonucleotide, aptamer or other organic complex that specifically interact with targeted molecules and then result in aggregation and the change of color can be quantified through spectrophotometer. This sensing approach was first applied to lead ion detection<sup>17,18</sup> by using “DNAzyme” which is literally a DNA strand with  $Pb^{2+}$  binding site that cleaves into two parts upon contact with  $Pb^{2+}$ . The resulted DNA strands hybridize with complementary sequence from neighboring particles and eventually cause aggregation. Colorimetric cocaine detection was also carried out by using cocaine aptamer linked gold nanoparticles. The nanoparticles were originally aggregated because of the pairing of conjugated oligonucleotide, but became disassembled with the present of cocaine as the aptamers binding to cocaine molecules and releasing the nanoparticles from each other, inducing color change of blue to red, of which the rate of change increased with cocaine concentration in the range of 50 to 500  $\mu M$ . Recently, the application colorimetric nanoparticle sensors has been widely expanded to the detection of multiple heavy metal and other hazardous ions, including, but not limited to, copper,<sup>19</sup> mercury,<sup>20</sup> silver,<sup>21</sup> cobalt,<sup>22</sup> arsenic<sup>23</sup> and cyanide<sup>24</sup>. This nanoparticle based sensor has also been investigated for detection of peptides such as enzyme and biomarker,<sup>25</sup> as well as targeted DNA/RNA sequence without amplified through PCR (polymerase chain reaction) for genetic

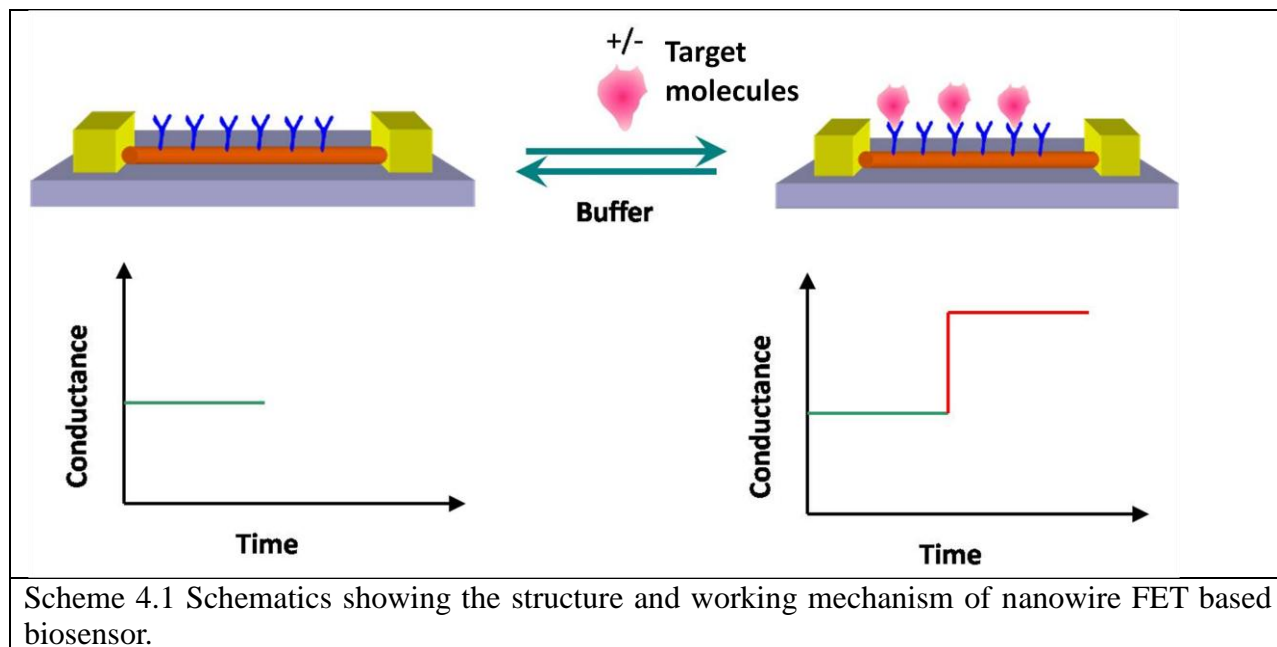
diagnosis of disease and pathogen, such as cancerous cell,<sup>26,27</sup> *Escherichia coli*,<sup>28</sup> and *Salmonella* bacteria.<sup>29</sup>

#### 4.1.3 Electrochemical sensing

Metallic and semiconductive nanoparticles can be immobilized on electrode and perform as electrochemical sensor through the specific interaction between particle surface functionality and analyte that causes conductivity change. The increased surface area comparing to conventional electrodes remarkably enhances the efficiency of electron transfer from analyte and improves detection sensitivity.<sup>30-32</sup> Numerous studies have been reported about using nanoparticle electrochemical sensor for the detection of nucleic acid. Mirkin et al<sup>33</sup> developed a DNA array detection method started with short oligonucleotide functionalized SiO<sub>2</sub> film deposited between two electrodes. Colloidal gold nanoparticles modified with oligonucleotide were then applied and bind to the SiO<sub>2</sub> film with the present of target DNA sequence through hybridization since both oligonucleotides were designed to be complementary with part of target DNA. Subsequently, silver deposition on the colloidal gold was introduced, functioned as signal amplifier to achieve detection sensitivity down to 500 fM with a point mutation selectivity of about 100000:1.<sup>33</sup> Detections of proteins or peptides have also been realized by using antibody<sup>34,35</sup> or aptamer<sup>36-38</sup> based on similar principle. Nanoparticle electrochemical sensor is also adapted to enzyme based sensing by immobilizing enzyme molecules on particles for the detection of substrate concentration or enzyme activity. One popular application is test of glucose concentration by using glucose oxidase functionalized particles, including platinum,<sup>39</sup> gold<sup>40,41</sup>, magnetite<sup>42</sup> and so on. As redox reaction, the oxidation of glucose triggers electron transfer in the enzyme-nanoparticle complex and the signal is recorded by voltametric analyzer.<sup>32</sup>

## 4.2 Nanowire based biosensors

Semiconductive nanowire (NW) has been widely employed in various applications involving solar cell, piezoelectric, nanophotonic, supercapacitor, chemical/ biological sensing and so on. The investigation of using nanowire for biosensing is one of the most appealing topics in both nanoscience and biomedicine, and became thrived with the fast development of other micro-fabrication techniques such as high-precision lithography and microfluidic channel, as well as multi-probe/multi-channel source meter and recording system. NW based field effect transistor (FET) has been demonstrated to be a powerful weapon with promising potential for the detection of different biological agents, including peptide/protein, nucleic acid, enzyme, toxin, bacteria and virus.



### 4.2.1 Principle of nanowire field effect transistor (FET) in biosensing

As shown in Figure 4.1, a typical NW FET can be described as semiconductive NW connected to two metal electrodes, source (S) and drain (D), which are connected to sourcemeter



to form a circuit; A third electrode, gate (G), is capacitively coupled with NW through a thin dielectric layer.<sup>43</sup> The conductance of the NW can be switch on/off, and enhanced in “on” direction by the bias applied on the gate electrode controls. For n-type semiconductor in which electron is the charge carrier, depletion of carriers happens under negative gate voltage and therefore conductance is reduced, while applying positive gate voltage generates accumulation of carrier and increases the conductance. And p-type semiconductor using vacancy as charge carrier behaves in the exact opposite way. An FET device should exhibit immediate response in conductance with high sensitivity against the change of gate voltage to be qualified as biosensor candidate. Hence measurements of source-drain conductance/current ( $I_{ds}$ ) vs. gate voltage ( $V_g$ ) are necessary for the evaluation of each device in order to locate the high  $I_{ds}/V_g$  sensitivity region which is ideal for biosensing detection. Since bio-molecules usually carry characteristic charges, for example, the charge of protein molecules can be predetermined by the amino acid composition and pH of buffer environment, and DNA carries negative charge of which the value is proportion to the chain length, these charge carrying molecules function as gate voltage on NW during detection. In addition, some FETs naturally stays in “off” status or low sensitivity zone under zero gate voltage and external gate bias will be required to ensure the device is working at the best performance.<sup>43</sup>

Besides the electric property of the FET device, another fundamental issue for biosensing is the specific binding between the nanowire and analyte molecule in solution environment; so that the nanowire is only picking up the signal from target molecules, not other agents in the solution. This binding is always realized by immobilizing molecular receptors such as antibody, aptamer and nucleic acid chain with complementary sequence on nanowire surface modified with appropriate linker to capture only the targeted molecule in solution. Therefore choosing the right

linker according to the nanowire material and functionality of receptor molecule has been the key factor in the preparation of nanowire biosensor.<sup>44</sup>

#### **4.2.2 Semiconductive nanowires for biosensing**

Semiconductor nanowire is one of the largest families of material in nanoscience with rapidly expanding territory. A huge selection of material being semiconductive in bulk state can be prepared in nanowire with nanoscale diameter and high aspect ratio through either top-down or bottom up approach. In top-down approach, nanowires are achieved by applying chemical/physical etching through micro-fabrication lithography on planar substrate to selectively remove atoms or molecules. This approach always results in highly ordered nanowire with designable measurements, but with disadvantage of elevated cost, limited output and extended preparation time, suggesting unsuitability for industrial fabrication. The other approach, bottom up method requires assembly of atom/molecule physically or chemically through vapor deposition, solution based synthesis or template directed synthesis, resulting in substantial yield with high purity and reduced cost, controllable electrochemical property from intentional doping and formation of junction structure, and capability of scaled up synthesis that are favored feature of industrial application.<sup>45</sup>

So far, metal oxide, silicon, carbon nanotube/graphene, conductive polymer and group III/V compounds have all been successfully synthesized in nanowire/belt/tube with various diameter and length for the device fabrication of biological sensing.<sup>46</sup>

##### **4.2.2.1 Indium Oxide ( $\text{In}_2\text{O}_3$ ) nanowire based biosensor**

Indium oxide nanowire always exhibits excellent transistor behavior with strong gate dependence that makes it qualified candidate for chemical and biological sensing.<sup>47</sup> Single crystalline  $\text{In}_2\text{O}_3$  nanowire is usually prepared by either thermal evaporation or chemical vapor deposition (CVD) method that use ultra high purity (99.9999%)  $\text{In}_2\text{O}_3$  and indium metal powder as precursor, respectively. Typically, the precursor and is placed in a ceramic boat located in the heating center of a horizontal tubular furnace. Silicon substrate, seeded with nanosized indium particle<sup>48</sup> or not<sup>49,50</sup>, deposited with noble metal nanoparticle as catalyst,<sup>51-53</sup> is put downstream of the precursor to collect product. Effective evaporation of the precursor requires temperature above 1000 °C and the nucleation and deposition happens between 750-800 °C for nanowire growth on substrate under argon flow as the mass transport media. And the residual amount of oxygen in the gas system is essential for the oxidization of indium and the initiation of nanowire growth.<sup>48</sup> An alternative of preparing  $\text{In}_2\text{O}_3$  nanowire in CVD method is introducing InAs as the source material which results in Arsenic-doped bi-crystalline nanobelt through a fast-heating-vapor-trapping method. In this method, silicon substrate with Au catalyst is placed close on the top of source material instead of downstream, and highly concentrated vapor from source material is generated upon a steep temperature rise to 550 °C, which increase the nanowire yield.<sup>54</sup> In addition, laser ablation approach is an improved CVD method for the synthesis of  $\text{In}_2\text{O}_3$  nanowire. Au nanoparticle in diluted aqueous solution is deposited on silicon substrate, serves as catalyst for the laser ablation promoted  $\text{In}_2\text{O}_3$  nanowire growth using InAs target as source material.<sup>55-57</sup>

In order to covalently link receptor molecules to the surface of  $\text{In}_2\text{O}_3$  nanowire for biosensing, bi-functional linkers with phosphonic acid group on one end and conventional functionality such as carboxylic acid on the other end is suggested.<sup>58</sup> It has already been demonstrated by studying

4-(1,4-dihydroxybenzene)butyl phosphonic acid (HQ-PA) modified  $\text{In}_2\text{O}_3$  in cyclic voltammetric and chronoamperometric measurements that phosphonic acid group is able to form robust covalent bond with  $\text{In}_2\text{O}_3$  through room temperature incubation and remain stable under various conditions.<sup>59</sup> Based on this functionalization platform,  $\text{In}_2\text{O}_3$  nanowire based FET that conjugated with specified antibodies has been utilized for the detection against a variety of bio-species, including prostate-specific antigen<sup>58</sup> and virus capsid protein<sup>55</sup>, as well as distinguishing detection of multiple cancer biomarkers.<sup>60</sup>

#### **4.2.2.2 Zinc oxide (ZnO) nanowire based biosensor**

Comparing to  $\text{In}_2\text{O}_3$ , ZnO is a much more common and dominant material in both nanoscience research and commercialized product. Semiconductive ZnO with a wide band gap of 3.37 eV possess great electronic and optical property with promising potential applications such as gas sensor, solar cell, photodetector and FET.<sup>61</sup> One dimensional nanostructure ZnO can be prepared through either gas phase or solution phase growth and resulted in various structure, including nanosized belt, wire, rod, whisker and tube.<sup>62</sup> Thermal evaporation,<sup>63-65</sup> metal-organic vapor-phase epitaxy,<sup>66-68</sup> chemical vapor deposition<sup>69-71</sup> and pulse laser deposition<sup>72-74</sup> are all efficient gas phase approaches using zinc, ZnO or organic zinc precursors for ZnO nanowire and nanorod growth with different promoting energy source and substrate. In solution phase approaches, hydrothermal is the most common method that using Zn(II) salt aqueous solution as the precursor and growth environment to achieve well-aligned ZnO nanowire. The density of nanowire can be adjusted by solution concentration and substrate patterning using e-beam lithography.<sup>75</sup> Template directed electrodeposition is another functional solution method by using anodic aluminum oxide (AAO) membrane as template to obtain ordered ZnO nanowire array.

Usually, Zn nanowire is first achieved through the deposition procedure in solution and then oxidized to ZnO by heating in air after template removal.<sup>76,77</sup>

The functionalization of ZnO nanowire can be very facile since its high isoelectric point (pI=9.5) allows receptor molecules such as acidic enzymes with much lower pI to stably attach through electrostatic interaction.<sup>78,79</sup> Glucose oxidase (GOD, pI=4.2) is the most studied enzyme that immobilized on ZnO NW surface through this convenient physical adsorption for glucose detection.<sup>78-80</sup> ZnO NW FET present excellent sensitivity against the redox reaction of glucose on attached GOD molecules and detection limit has been pushed down to 1  $\mu$ M at a signal-to-noise ratio of 3.<sup>80</sup> ZnO can also be covalently modified with linker 3-(trimethoxysilyl) propyl aldehyde and conjugated to antibody with hydrazide ends for real time detection of antigen.<sup>81,82</sup> Furthermore, an interesting investigation revealed the high bio-compatibility of ZnO nanowire that the cell remained active and good reproductive ability after cultured with low concentration of NW for 48 h, indicating the potential application of cellular sensing biological engineering of ZnO NW.<sup>83</sup>

#### **4.2.2.3 Silicon nanowire based biosensor**

As the key element for semiconductor material with applications that influence our life from every corner, silicon plays the irreplaceable role in material science and technology. Silicon nanostructures, including thin film, nanocrystals, nanowire/tube/belt and various assembly structures have been exploited and adapted to the research of photovoltaic solar cell, light emission, bio-medicine and sensing.<sup>43,44,84</sup> One dimensional silicon nanowire with FET property can be prepared through multiple approaches. CVD methods using silane, SiH<sub>4</sub> and Si<sub>2</sub>H<sub>6</sub> or halogen substituted silane, SiH<sub>2</sub>Cl<sub>2</sub> and SiCl<sub>4</sub> as precursor is the most commonly used technique

for vertical aligned silicon nanowire synthesis. Under the catalysis of Au nanoparticle on silicon substrate, the nanowire growth follows a vapor-liquid-solid mechanism at elevated temperature which induces the decomposition of the gas phase precursor. The nanowire diameter is primarily determined by the size of catalyst particle and the length is basically proportional to reaction time.<sup>85,86</sup> Nanowire doping can be easily realized by introducing vapor phase dopants like AsCl<sub>3</sub>, PCl<sub>3</sub>, PH<sub>3</sub>, and B<sub>2</sub>H<sub>6</sub> at high temperature to tailor the electric property.<sup>86,87</sup> Besides CVD, other bottom-up growth of silicon nanowire includes laser ablation,<sup>88,89</sup> molecular beam epitaxy<sup>90,91</sup> and silicon monoxide evaporation,<sup>92,93</sup> etc. Another popular silicon nanowire preparation approach that especially beneficial for microelectric application is called “top-down” technique. This is a procedure to accomplish both horizontal nanowire array synthesis and FET device fabrication at the same time with unique features of high uniformity and reproducibility.<sup>94,95</sup> Typically, e-beam lithography (EBL) is performed on a silicon on insulator (SOI) wafer with a 50-80 nm thick silicon layer on the top of a 50-100 nm thick oxide layer to pattern the desired nanowire array structure, then silicon nanowire can be achieved after applying reactive ion etching on unpatterned area deep down to the oxide layer.<sup>94,96</sup> This technique provide a lot of advantages over tradition bottom up nanowire synthesis discussed above, such as elimination of difference of each single nanowire, tunable nanowire length and diameter, and capability of large scale fabrication.

Before the surface modification of silicon nanowire which directs further conjugation of receptor molecules for biosensing, the nanowire is always treated with water-vapor plasma to clean sample surface as well as generate hydroxyl-terminated hydrophilic surface.<sup>96</sup> Then crosslinkers such as 3-mercaptopropyltrimethoxysilane (MPTMS),<sup>96</sup> trimethyloxysilane aldehyde,<sup>94</sup> 3-aminopropyltriethoxysilane (APTES)<sup>97</sup> are applied to expose thiol, aldehyde,

respectively to allow further functionalization. Nucleic acid probe modified nanowire can be applied for detection of DNA and specific gene mutation.<sup>98</sup> The sensitivity of this label-free DNA detection can be reached to one base mismatch discrimination in the concentration range of 1 fM to 1 nM.<sup>96,99</sup> Nanowire FET linked with antibody or aptamer has been exploited for sensing of antigen-specific T-cell immune response,<sup>100,101</sup> cardiac biomarker with antibody,<sup>97</sup> vascular endothelial growth factor,<sup>102</sup> multiple cancer biomarkers from whole blood sample<sup>103</sup> and eventually multiplex detection using nanowire array,<sup>104</sup> and the substitution of the reactive substrate in conventional enzyme-linked immunosorbent assay (ELISA) for quantitative protein sensing.<sup>105</sup> Furthermore, detection of single virus with fluorescence labeling was realized using silicon nanowire FET integrated with microfluidic channel and the whole process was monitored by both electrical recording and optical microscopy, demonstrating the change of electrical signal happens simultaneously upon the contact between virus and nanowire surface.<sup>106</sup> Also, neuronal signal can be collected by simply connecting dendrite and synapse to nanowire<sup>107</sup> and this idea was further developed for mapping neural circuits in acute brain slice using high density array.<sup>108</sup> Based on traditional nanowire FET structure, a unique branch structure with a germanium nanowire probe pointing out from silicon nanowire transistor and vertical to the device plane was fabricated for intracellular recording of action potential.<sup>109</sup> In addition, device fabrication can also be completed on flexible transparent polymer substrate to achieve better contact with sample and employed for continuously recording spontaneous heart beat.<sup>110</sup>

#### **4.2.2.4 Conducting polymer (CP) nanowire based biosensor**

Conducting polymer features in  $sp^2$  hybridized backbone in which  $\pi$ -conjugated structure can improve the band gap of the material towards semiconductor property. Several commonly

studied CPs are Polyaniline (PANI), Polypyrrole (PPy), Polythiophene (PT), Poly(3-hexylthiophene) (P3HT) and Poly(3,4-ethylenedioxythiophene) (PEDOT). Anionic dopants that vary from small spherical to large polyionic which adjusted concentrations are always applied to modulate the conductivity of the polymer. Another factor influencing conductivity is  $\pi$ -conjugation length which may differ from polymer chain length due defects such as improper linkage and branching. Also disorder of polymer formation describing the crystalline status can affect electrical property and sensing performance. Both defect and disorder usually occurs during synthesis and subsequent preparation procedures.<sup>111</sup> There are four popular synthesis techniques for CP,<sup>112</sup> dip-pen nanolithography,<sup>113,114</sup> mechanical stretching,<sup>115</sup> electrospinning<sup>116</sup> and template-directed electrochemical synthesis.<sup>117</sup>

Since CP is rich in surface functionality groups according to the characteristic of different monomers, conjugation of receptor molecules can be relatively easy and direct. Antibody covalently conjugated Ppy and poly (pyrrolepropylic acid) (poly (PPA)) nanowires have been introduced to the detection of cancer marker and human serum albumin for early diagnosis of renal diseases, respectively.<sup>118,119</sup> CP nanowire can also be integrated with other nano or bio material to enhance the immobilization of capturing molecules and sensor performance. For example, PANI nanowire network decorated with peroxidase-conjugated Au nanoparticle was fabricated for in-situ detection of ischemic cell.<sup>120</sup> In addition, PEDOT has been employed to form hybrid nanowire structure with bacteria-infecting virus which can be easily conjugated with engineered recognizing polypeptide for protein detection.<sup>121,122</sup>

#### **4.2.2.5 Others**



Carbon nanostructures with field-effect property, including carbon nanotube (CNT) and graphene, have drawn extensive interest worldwide dramatically during the recent years for the potential application of energy storage, microelectronics, chemical and bio-sensing, and template for other synthesis.<sup>123,124</sup> CNTs are composed entirely from  $sp^2$  carbon bonding and can be divided to single wall (SWNT) and multiwalled (MWNT). The electrical property of CNT is majorly determined by atomic arrangement (chirality) and diameter. Graphene is a two dimensional material with layers consist of carbon atoms in six-member ring arrangement. It can be considered as the fundamental building element for all carbon structures including fullerene, CNT and graphite.<sup>124</sup> During biosensing of CNT and graphene, ssDNA probes can be immobilized on the material surface non-covalently through  $\pi$ -stacking of nucleic acid base and subject to DNA detection.<sup>125,126</sup> Also, the carbon can be oxidized to provide carboxyl groups for further functionalization of receptor molecules such as antibodies for antigen and cell detection.<sup>127,128</sup> In addition, 1-pyrenebutanoic acid succinimidyl ester with large  $\pi$ -conjugation structure is also frequently used as the linker between carbon surface and antibody.<sup>127,129</sup>

Among group III/V compounds, GaN nanowire has been utilized for DNA detection. The nanowire surface was first modified with (3-mercaptopropyl) trimethoxysilane (MPTS) to expose thiol groups, and then covalently linked with DNA probe for detection through nucleic acid hybridization.<sup>130</sup>

### 4.3 References

- (1) Dabbousi, B. O.; Rodriguez-Viejo, J.; Mikulec, F. V.; Heine, J. R.; Mattoussi, H.; Ober, R.; Jensen, K. F.; Bawendi, M. G. *J. Phys. Chem. B* **1997**, *101*, 9463.
- (2) Chan, W. C. W.; Nie, S. *Science* **1998**, *281*, 2016.
- (3) Bruchez, M.; Moronne, M.; Gin, P.; Weiss, S.; Alivisatos, A. P. *Science* **1998**, *281*, 2013.
- (4) Pathak, S.; Choi, S.-K.; Arnheim, N.; Thompson, M. E. *J. Am. Chem. Soc.* **2001**, *123*, 4103.

- (5) Wu, X.; Liu, H.; Liu, J.; Haley, K. N.; Treadway, J. A.; Larson, J. P.; Ge, N.; Peale, F.; Bruchez, M. P. *Nat Biotech* **2003**, *21*, 41.
- (6) Bentzen, E. L.; House, F.; Utley, T. J.; Crowe, J. E.; Wright, D. W. *Nano Lett.* **2005**, *5*, 591.
- (7) Gao, X.; Cui, Y.; Levenson, R. M.; Chung, L. W. K.; Nie, S. *Nat Biotech* **2004**, *22*, 969.
- (8) Tada, H.; Higuchi, H.; Wanatabe, T. M.; Ohuchi, N. *Cancer Res.* **2007**, *67*, 1138.
- (9) Cai, W.; Shin, D.-W.; Chen, K.; Gheysens, O.; Cao, Q.; Wang, S. X.; Gambhir, S. S.; Chen, X. *Nano Lett.* **2006**, *6*, 669.
- (10) Orndorff, R. L.; Rosenthal, S. J. *Nano Lett.* **2009**, *9*, 2589.
- (11) Zhou, D.; Piper, J. D.; Abell, C.; Klenerman, D.; Kang, D.-J.; Ying, L. *Chem. Commun.* **2005**, 4807.
- (12) Zhou, D.; Ying, L.; Hong, X.; Hall, E. A.; Abell, C.; Klenerman, D. *Langmuir* **2008**, *24*, 1659.
- (13) Peng, H.; Zhang, L.; Kjälman, T. H. M.; Soeller, C. *J. Am. Chem. Soc.* **2007**, *129*, 3048.
- (14) Rosenthal, S. J.; Chang, J. C.; Kovtun, O.; McBride, J. R.; Tomlinson, I. D. *Chem. Biol.* **2011**, *18*, 10.
- (15) Murphy, C. J.; Gole, A. M.; Stone, J. W.; Sisco, P. N.; Alkilany, A. M.; Goldsmith, E. C.; Baxter, S. C. *Acc. Chem. Res.* **2008**, *41*, 1721.
- (16) Niemeyer, C. M. *Angew. Chem. Int. Ed.* **2001**, *40*, 4128.
- (17) Liu, J.; Lu, Y. *J. Am. Chem. Soc.* **2003**, *125*, 6642.
- (18) Liu, J.; Lu, Y. *J. Am. Chem. Soc.* **2004**, *126*, 12298.
- (19) He, X.; Liu, H.; Li, Y.; Wang, S.; Wang, N.; Xiao, J.; Xu, X.; Zhu, D. *Adv. Mater.* **2005**, *17*, 2811.
- (20) Huang, C.-C.; Chang, H.-T. *Chem. Commun.* **2007**, 1215.
- (21) Lin, C.-Y.; Yu, C.-J.; Lin, Y.-H.; Tseng, W.-L. *Anal. Chem.* **2010**, *82*, 6830.
- (22) Yao, Y.; Tian, D.; Li, H. *ACS Appl. Mater. Inter* **2010**, *2*, 684.
- (23) Kalluri, J. R.; Arbnesi, T.; Afrin Khan, S.; Neely, A.; Candice, P.; Varisli, B.; Washington, M.; McAfee, S.; Robinson, B.; Banerjee, S.; Singh, A. K.; Senapati, D.; Ray, P. C. *Angew. Chem. Int. Ed.* **2009**, *48*, 9668.
- (24) Liu, C.-Y.; Tseng, W.-L. *Chem. Commun.* **2011**, *47*, 2550.
- (25) De, M.; Ghosh, P. S.; Rotello, V. M. *Adv. Mater.* **2008**, *20*, 4225.
- (26) Medley, C. D.; Smith, J. E.; Tang, Z.; Wu, Y.; Bamrungsap, S.; Tan, W. *Anal. Chem.* **2008**, *80*, 1067.
- (27) Lu, W.; Arumugam, S. R.; Senapati, D.; Singh, A. K.; Arbnesi, T.; Khan, S. A.; Yu, H.; Ray, P. C. *ACS Nano* **2010**, *4*, 1739.
- (28) Yeh, Y.-Q.; Chen, B.-C.; Lin, H.-P.; Tang, C.-Y. *Langmuir* **2005**, *22*, 6.
- (29) Wang, S.; Singh, A. K.; Senapati, D.; Neely, A.; Yu, H.; Ray, P. C. *Chemistry – A European Journal* **2010**, *16*, 5600.
- (30) Katz, E.; Willner, I.; Wang, J. *Electroanalysis* **2004**, *16*, 19.
- (31) Yu, A.; Liang, Z.; Cho, J.; Caruso, F. *Nano Lett.* **2003**, *3*, 1203.
- (32) Fang, W.; Shengshui, H. *Microchimica Acta* **2009**, *165*, 1.
- (33) Park, S.-J.; Taton, T. A.; Mirkin, C. A. *Science* **2002**, *295*, 1503.
- (34) Velev, O. D.; Kaler, E. W. *Langmuir* **1999**, *15*, 3693.
- (35) Tang, D.; Yuan, R.; Chai, Y. *J. Phys. Chem. B* **2006**, *110*, 11640.
- (36) Ikebukuro, K.; Kiyohara, C.; Sode, K. *Anal. Lett.* **2004**, *37*, 2901.

- (37) Zhang, Y.-L.; Huang, Y.; Jiang, J.-H.; Shen, G.-L.; Yu, R.-Q. *J. Am. Chem. Soc.* **2007**, *129*, 15448.
- (38) Numnuam, A.; Chumbimuni-Torres, K. Y.; Xiang, Y.; Bash, R.; Thavarungkul, P.; Kanatharana, P.; Pretsch, E.; Wang, J.; Bakker, E. *Anal. Chem.* **2008**, *80*, 707.
- (39) Wu, H.; Wang, J.; Kang, X.; Wang, C.; Wang, D.; Liu, J.; Aksay, I. A.; Lin, Y. *Talanta* **2009**, *80*, 403.
- (40) Lioubashevski, O.; Chegel, V. I.; Patolsky, F.; Katz, E.; Willner, I. *J. Am. Chem. Soc.* **2004**, *126*, 7133.
- (41) Wu, B.-Y.; Hou, S.-H.; Yin, F.; Li, J.; Zhao, Z.-X.; Huang, J.-D.; Chen, Q. *Biosens. Bioelectron.* **2007**, *22*, 838.
- (42) Rossi, L.; Quach, A.; Rosenzweig, Z. *Analytical & Bioanalytical Chemistry* **2004**, 380, 606.
- (43) Patolsky, F.; Zheng, G.; Lieber, C. M. *Anal. Chem.* **2006**, *78*, 4260.
- (44) Patolsky, F.; Lieber, C. M. *Mater. Today* **2005**, *8*, 20.
- (45) Comini, E.; Baratto, C.; Faglia, G.; Ferroni, M.; Vomiero, A.; Sberveglieri, G. *Prog. Mater. Sci.* **2009**, *54*, 1.
- (46) Barth, S.; Hernandez-Ramirez, F.; Holmes, J. D.; Romano-Rodriguez, A. *Prog. Mater. Sci.* **2010**, *55*, 563.
- (47) Zhang, D.; Liu, Z.; Li, C.; Tang, T.; Liu, X.; Han, S.; Lei, B.; Zhou, C. *Nano Lett.* **2004**, *4*, 1919.
- (48) Vomiero, A.; Bianchi, S.; Comini, E.; Faglia, G.; Ferroni, M.; Sberveglieri, G. *Crystal Growth & Design* **2007**, *7*, 2500.
- (49) Fanhao, Z.; Zhang, X.; Jin, W.; Lisheng, W.; Lina, Z. *Nanotechnology* **2004**, *15*, 596.
- (50) Kam, K. C.; Deepak, F. L.; Cheetham, A. K.; Rao, C. N. R. *Chem. Phys. Lett.* **2004**, 397, 329.
- (51) Johnson, M. C.; Aloni, S.; McCready, D. E.; Bourret-Courchesne, E. D. *Crystal Growth & Design* **2006**, *6*, 1936.
- (52) Youguo, Y.; Ye, Z.; Haibo, Z.; Junxi, Z.; Xueli, C.; Lide, Z. *Nanotechnology* **2007**, *18*, 175601.
- (53) Zhang, J.; Qing, X.; Jiang, F.; Dai, Z. *Chem. Phys. Lett.* **2003**, *371*, 311.
- (54) Shen, G.; Chen, D. *J. Mater. Chem.* **2010**, *20*, 10888.
- (55) Ishikawa, F. N.; Chang, H.-K.; Curreli, M.; Liao, H.-I.; Olson, C. A.; Chen, P.-C.; Zhang, R.; Roberts, R. W.; Sun, R.; Cote, R. J.; Thompson, M. E.; Zhou, C. *ACS Nano* **2009**, *3*, 1219.
- (56) Li, C.; Zhang, D.; Han, S.; Liu, X.; Tang, T.; Zhou, C. *Adv. Mater.* **2003**, *15*, 143.
- (57) Chen, P.-C.; Shen, G.; Chen, H.; Ha, Y.-g.; Wu, C.; Sukcharoenchoke, S.; Fu, Y.; Liu, J.; Facchetti, A.; Marks, T. J.; Thompson, M. E.; Zhou, C. *ACS Nano* **2009**, *3*, 3383.
- (58) Li, C.; Curreli, M.; Lin, H.; Lei, B.; Ishikawa, F. N.; Datar, R.; Cote, R. J.; Thompson, M. E.; Zhou, C. *J. Am. Chem. Soc.* **2005**, *127*, 12484.
- (59) Curreli, M.; Li, C.; Sun, Y.; Lei, B.; Gunderson, M. A.; Thompson, M. E.; Zhou, C. *J. Am. Chem. Soc.* **2005**, *127*, 6922.
- (60) Chang, H.-K.; Ishikawa, F. N.; Zhang, R.; Datar, R.; Cote, R. J.; Thompson, M. E.; Zhou, C. *ACS Nano* **2011**, *5*, 9883.
- (61) Greene, L. E.; Yuhas, B. D.; Law, M.; Zitoun, D.; Yang, P. *Inorg. Chem.* **2006**, *45*, 7535.
- (62) Dai, Z. R.; Pan, Z. W.; Wang, Z. L. *Adv. Funct. Mater.* **2003**, *13*, 9.
- (63) Yao, B. D.; Chan, Y. F.; Wang, N. *Appl. Phys. Lett.* **2002**, *81*, 757.

- (64) Banerjee, D.; Lao, J. Y.; Wang, D. Z.; Huang, J. Y.; Ren, Z. F.; Steeves, D.; Kimball, B.; Sennett, M. *Appl. Phys. Lett.* **2003**, *83*, 2061.
- (65) Kar, S.; Pal, B. N.; Chaudhuri, S.; Chakravorty, D. *J. Phys. Chem. B* **2006**, *110*, 4605.
- (66) Jeong, M.-C.; Oh, B.-Y.; Lee, W.; Myoung, J.-M. *J. Cryst. Growth* **2004**, *268*, 149.
- (67) Baxter, J. B.; Aydil, E. S. *J. Cryst. Growth* **2005**, *274*, 407.
- (68) Park, W. I.; Kim, D. H.; Jung, S. W.; Yi, G.-C. *Appl. Phys. Lett.* **2002**, *80*, 4232.
- (69) Xiang, B.; Wang, P.; Zhang, X.; Dayeh, S. A.; Aplin, D. P. R.; Soci, C.; Yu, D.; Wang, D. *Nano Lett.* **2006**, *7*, 323.
- (70) Chang, P.-C.; Fan, Z.; Wang, D.; Tseng, W.-Y.; Chiou, W.-A.; Hong, J.; Lu, J. G. *Chem. Mater.* **2004**, *16*, 5133.
- (71) Fan, Z.; Wang, D.; Chang, P.-C.; Tseng, W.-Y.; Lu, J. G. *Appl. Phys. Lett.* **2004**, *85*, 5923.
- (72) Guo, R.; Nishimura, J.; Matsumoto, M.; Higashihata, M.; Nakamura, D.; Okada, T. *Applied Physics B: Lasers & Optics* **2009**, *94*, 33.
- (73) Rahm, A.; Lorenz, M.; Nobis, T.; Zimmermann, G.; Grundmann, M.; Fuhrmann, B.; Syrowatka, F. *Applied Physics A: Materials Science & Processing* **2007**, *88*, 31.
- (74) Sun, Y.; Fuge, G. M.; Ashfold, M. N. R. *Chem. Phys. Lett.* **2004**, *396*, 21.
- (75) Wang, Z. L. *Materials Science and Engineering: R: Reports* **2009**, *64*, 33.
- (76) Li, Y.; Cheng, G. S.; Zhang, L. D. *J. Mater. Res.* **2000**, *15*, 2305.
- (77) Li, Y.; Meng, G. W.; Zhang, L. D.; Philipp, F. *Appl. Phys. Lett.* **2000**, *76*, 2011.
- (78) Wang, J. X.; Sun, X. W.; Wei, A.; Lei, Y.; Cai, X. P.; Li, C. M.; Dong, Z. L. *Appl. Phys. Lett.* **2006**, *88*, 233106.
- (79) Zang, J.; Li, C. M.; Cui, X.; Wang, J.; Sun, X.; Dong, H.; Sun, C. Q. *Electroanalysis* **2007**, *19*, 1008.
- (80) Liu, J.; Guo, C.; Li, C. M.; Li, Y.; Chi, Q.; Huang, X.; Liao, L.; Yu, T. *Electrochem. Commun.* **2009**, *11*, 202.
- (81) Jin, L.; Goud, J.; Raj, P. M.; Iyer, M.; Zhonglin, W.; Tummala, R. R. In *Electronic Components and Technology Conference, 2007. ECTC '07. Proceedings. 57th 2007*, p 1971.
- (82) Jin, L.; Goud, J.; Raj, P. M.; Iyer, M.; Zhong Lin, W.; Tummala, R. R. In *Electronic Components and Technology Conference, 2008. ECTC 2008. 58th 2008*, p 1317.
- (83) Li, Z.; Yang, R.; Yu, M.; Bai, F.; Li, C.; Wang, Z. L. *J. Phys. Chem. C* **2008**, *112*, 20114.
- (84) Fang, X.; Bando, Y.; Gautam, U. K.; Ye, C.; Golberg, D. *J. Mater. Chem.* **2008**, *18*, 509.
- (85) Wu, X.; Kulkarni, J. S.; Collins, G.; Petkov, N.; Almécija, D.; Boland, J. J.; Erts, D.; Holmes, J. D. *Chem. Mater.* **2008**, *20*, 5954.
- (86) Schmidt, V.; Wittemann, J. V.; Gösele, U. *Chem. Rev.* **2010**, *110*, 361.
- (87) Givargizov, E. I. *J. Cryst. Growth* **1975**, *31*, 20.
- (88) Morales, A. M.; Lieber, C. M. *Science* **1998**, *279*, 208.
- (89) Zhang, Y. F.; Tang, Y. H.; Wang, N.; Yu, D. P.; Lee, C. S.; Bello, I.; Lee, S. T. *Appl. Phys. Lett.* **1998**, *72*, 1835.
- (90) Schubert, L.; Werner, P.; Zakharov, N. D.; Gerth, G.; Kolb, F. M.; Long, L.; Gosele, U.; Tan, T. Y. *Appl. Phys. Lett.* **2004**, *84*, 4968.
- (91) Zakharov, N.; Werner, P.; Sokolov, L.; Gösele, U. *Physica E: Low-dimensional Systems and Nanostructures* **2007**, *37*, 148.
- (92) Pan, Z. W.; Dai, Z. R.; Xu, L.; Lee, S. T.; Wang, Z. L. *J. Phys. Chem. B* **2001**, *105*, 2507.
- (93) Kolb, F. M.; Hofmeister, H.; Scholz, R.; Zacharias, M.; Gösele, U.; Ma, D. D.; Lee, S.-T. *J. Electrochem. Soc.* **2004**, *151*, G472.

- (94) Gao, Z.; Agarwal, A.; Trigg, A. D.; Singh, N.; Fang, C.; Tung, C.-H.; Fan, Y.; Buddharaju, K. D.; Kong, J. *Anal. Chem.* **2007**, *79*, 3291.
- (95) Patolsky, F.; Zheng, G.; Lieber, C. M. *Nat. Protocols* **2006**, *1*, 1711.
- (96) Li, Z.; Chen, Y.; Li, X.; Kamins, T. I.; Nauka, K.; Williams, R. S. *Nano Lett.* **2004**, *4*, 245.
- (97) Chua, J. H.; Chee, R.-E.; Agarwal, A.; Wong, S. M.; Zhang, G.-J. *Anal. Chem.* **2009**, *81*, 6266.
- (98) Wu, C.-C.; Ko, F.-H.; Yang, Y.-S.; Hsia, D.-L.; Lee, B.-S.; Su, T.-S. *Biosens. Bioelectron.* **2009**, *25*, 820.
- (99) Gao, A.; Lu, N.; Dai, P.; Li, T.; Pei, H.; Gao, X.; Gong, Y.; Wang, Y.; Fan, C. *Nano Lett.* **2011**, *11*, 3974.
- (100) Stern, E.; Klemic, J. F.; Routenberg, D. A.; Wyrembak, P. N.; Turner-Evans, D. B.; Hamilton, A. D.; LaVan, D. A.; Fahmy, T. M.; Reed, M. A. *Nature* **2007**, *445*, 519.
- (101) Stern, E.; Steenblock, E. R.; Reed, M. A.; Fahmy, T. M. *Nano Lett.* **2008**, *8*, 3310.
- (102) Lee, H.-S.; Kim, K. S.; Kim, C.-J.; Hahn, S. K.; Jo, M.-H. *Biosens. Bioelectron.* **2009**, *24*, 1801.
- (103) Stern, E.; Vacic, A.; Rajan, N. K.; Criscione, J. M.; Park, J.; Ilic, B. R.; Mooney, D. J.; Reed, M. A.; Fahmy, T. M. *Nat Nano* **2010**, *5*, 138.
- (104) Zheng, G.; Patolsky, F.; Cui, Y.; Wang, W. U.; Lieber, C. M. *Nat Biotech* **2005**, *23*, 1294.
- (105) Stern, E.; Vacic, A.; Li, C.; Ishikawa, F. N.; Zhou, C.; Reed, M. A.; Fahmy, T. M. *Small* **2010**, *6*, 232.
- (106) Patolsky, F.; Zheng, G.; Hayden, O.; Lakadamyali, M.; Zhuang, X.; Lieber, C. M. *Proceedings of the National Academy of Sciences of the United States of America* **2004**, *101*, 14017.
- (107) Patolsky, F.; Timko, B. P.; Yu, G.; Fang, Y.; Greytak, A. B.; Zheng, G.; Lieber, C. M. *Science* **2006**, *313*, 1100.
- (108) Qing, Q.; Pal, S. K.; Tian, B.; Duan, X.; Timko, B. P.; Cohen-Karni, T.; Murthy, V. N.; Lieber, C. M. *Proceedings of the National Academy of Sciences* **2010**, *107*, 1882.
- (109) Duan, X.; Gao, R.; Xie, P.; Cohen-Karni, T.; Qing, Q.; Choe, H. S.; Tian, B.; Jiang, X.; Lieber, C. M. *Nat Nano* **2012**, *7*, 174.
- (110) Timko, B. P.; Cohen-Karni, T.; Yu, G.; Qing, Q.; Tian, B.; Lieber, C. M. *Nano Lett.* **2009**, *9*, 914.
- (111) Hangarter, C. M.; Bangar, M.; Mulchandani, A.; Myung, N. V. *J. Mater. Chem.* **2010**, *20*, 3131.
- (112) Wanekaya, A. K.; Chen, W.; Myung, N. V.; Mulchandani, A. *Electroanalysis* **2006**, *18*, 533.
- (113) Lim, J. H.; Mirkin, C. A. *Adv. Mater.* **2002**, *14*, 1474.
- (114) Maynor, B. W.; Filocamo, S. F.; Grinstaff, M. W.; Liu, J. *J. Am. Chem. Soc.* **2001**, *124*, 522.
- (115) He, H. X.; Li, C. Z.; Tao, N. J. *Appl. Phys. Lett.* **2001**, *78*, 811.
- (116) Liu, H.; Kameoka, J.; Czaplewski, D. A.; Craighead, H. G. *Nano Lett.* **2004**, *4*, 671.
- (117) Jérôme, C.; Jérôme, R. *Angew. Chem. Int. Ed.* **1998**, *37*, 2488.
- (118) Bangar, M. A.; Shirale, D. J.; Chen, W.; Myung, N. V.; Mulchandani, A. *Anal. Chem.* **2009**, *81*, 2168.
- (119) Tolani, S.; Craig, M.; DeLong, R.; Ghosh, K.; Wanekaya, A. *Analytical and Bioanalytical Chemistry* **2009**, *393*, 1225.

- (120) Guo, C. X.; Zheng, X. T.; Ng, S. R.; Lai, Y.; Lei, Y.; Li, C. M. *Chem. Commun.* **2011**, 47, 2652.
- (121) Arter, J. A.; Taggart, D. K.; McIntire, T. M.; Penner, R. M.; Weiss, G. A. *Nano Lett.* **2010**, 10, 4858.
- (122) Arter, J. A.; Diaz, J. E.; Donavan, K. C.; Yuan, T.; Penner, R. M.; Weiss, G. A. *Anal. Chem.* **2012**, 84, 2776.
- (123) Ajayan, P.; Zhou, O.; Dresselhaus, M., Dresselhaus, G., Avouris, P., Eds.; Springer Berlin / Heidelberg: 2001; Vol. 80, p 391.
- (124) Hu, P.; Zhang, J.; Li, L.; Wang, Z.; O'Neill, W.; Estrela, P. *Sensors* **2010**, 10, 5133.
- (125) Ajayan, P. M. *Chem. Rev.* **1999**, 99, 1787.
- (126) Varghese, N.; Mogera, U.; Govindaraj, A.; Das, A.; Maiti, P. K.; Sood, A. K.; Rao, C. N. R. *ChemPhysChem* **2009**, 10, 206.
- (127) Jiang, K.; Eitan, A.; Schadler, L. S.; Ajayan, P. M.; Siegel, R. W.; Grobert, N.; Mayne, M.; Reyes-Reyes, M.; Terrones, H.; Terrones, M. *Nano Lett.* **2003**, 3, 275.
- (128) Tsai, C.-C.; Yang, C.-C.; Shih, P.-Y.; Wu, C.-S.; Chen, C.-D.; Pan, C.-Y.; Chen, Y.-T. *J. Phys. Chem. B* **2008**, 112, 9165.
- (129) Ning, S.; Eric, W.; Balaji, P. *Nanotechnology* **2008**, 19, 465101.
- (130) Chen, C.-P.; Ganguly, A.; Lu, C.-Y.; Chen, T.-Y.; Kuo, C.-C.; Chen, R.-S.; Tu, W.-H.; Fischer, W. B.; Chen, K.-H.; Chen, L.-C. *Anal. Chem.* **2011**, 83, 1938.

## **Chapter V: Indium Oxide Nanowire Based Field-Effect Transistor for Biosensing**

### **5.1 Introduction**

In recent years, field-effect devices, such as semiconductor nanowire based transistors for highly selective and ultrasensitive biological detections, have been extensively studied.<sup>1-7</sup> These devices are designed to capture targeting agents and their field effect property which allows the detection of bio-agents with minimized unspecific binding and noise-signal ratio through antibody-antigen interaction, enzyme-substrate interaction, hydrogen bond between nucleic acid chain, and other specific binding reactions available among bio-molecules. These interactions on the surface of transistors play the role of gate voltage change and therefore result in conductance differences which can be easily recorded using a conventional source meter. The captured agents in biosensors include antibodies, oligonucleotides, enzymes, small ligands, etc.

As one of the most widely used semiconducting nanomaterials, indium oxide ( $\text{In}_2\text{O}_3$ ) nanowire has shown its promising chemical-gating capacity in gas-sensing for toxic gases such as nitrogen dioxide and ammonia.<sup>8</sup> Later, this gate-effect phenomenon was further demonstrated by conjugating small organic molecules and bio-agents<sup>9,10</sup> and performed a series detection of single-strand DNA sequence,<sup>11</sup> prostate-specific antigen,<sup>12</sup> and virus capsid protein<sup>13</sup>, which indicate  $\text{In}_2\text{O}_3$  nanowires as a very promising semiconductor nanomaterial for practical applications in biological sensing.

In this chapter, we fabricated and characterized  $\text{In}_2\text{O}_3$  nanowires as field effect biological sensors. A toxic protein ricin, known as inducing severe allergic reactions and death, is detected by our transistors through its engineered antibody. The FETs can be employed to build a

potential platform for biosensors for ricin detection with high sensitivity and selectivity. Also, to the best of our knowledge, so far, no study has been reported about using fluorescence imaging to investigate the binding between antibody and nanowire to ensure the binding efficiency and blocking agent efficiency, as well as to eliminate the non-specific interaction between antigen and nanowire surface. Herein, a series of experiments were conducted using engineered antibody to capture fluorescence labeled ricin and the laser confocal microscopy images were subjected to qualification analysis.

## **5.2 Experimental**

**5.2.1 Material and chemicals.** Indium arsenide (InAs, 99.9999%) was purchased from Alfa Aesar. Acetone (99.5%) and isopropyl alcohol (99.5%) were purchased from EMD Chemical. Absolute ethanol was purchased from AAPER Alcohol and Chemical Co. Positive electron beam resist Poly(methyl methacrylate) 495 PMMA A4 and MIBK/IPA 1:3 developer were purchased from MICROCHEM. Silicon wafer with (100) orientation was purchased from University Wafer. Phosphate buffer saline (PBS, 10x stock solution), Tween-20, bovine serum albumin (BSA, 96%) were purchased from Sigma-Aldrich. Fluorescence labeled transferrin, ricin and antihuman IgG, and engineered antibodies were all obtained from Dr. Seth Pincus's laboratory in Research Institute for Children at Children's Hospital New Orleans, and freshly diluted to target concentration with PBS prior to use. Aqua-mount slide mounting media was purchased from Thermo Scientific.

**5.2.2 Synthesis of semiconductive  $\text{In}_2\text{O}_3$  nanowire.**  $\text{In}_2\text{O}_3$  nanowires were synthesized through chemical vapor deposition (CVD) approach which was modified based on a fast-heating-vapor-



trapping method.<sup>14</sup> The silicon substrate for nanowire growth was prepared by depositing a layer of gold nanoparticles, with approximate thickness of 5 nm, by using the Cressington 308R coating system. The InAs pieces were first gently ground into fine powder, and then transferred to an alumina crucible boat, with silicon substrate placing close to the top with the gold nanoparticle layer facing downward. The crucible boat was then placed in a small quartz test with a closed end, and the whole assembly was settled in a 2-inch quartz tube which was installed in a Lindburg/Blue tube furnace with vacuum pump and argon connection, but outside the heating area. The tube was pumped down to vacuum lower than 1 torr and filled with argon. This pump-fill process was repeated for several cycles to completely remove the oxygen in the system. Then the argon flow was reduced to 100 sccm, and the tube was heated to 550 °C. Under a pressure of 1 atm, the crucible boat was moved to the center of the heating area via a magnet, and the reaction started immediately. After the reaction, the tube furnace was naturally cooled down, and the nanowire sample was examined by Carl Zeiss 1530 VP field emission scanning electron microscope (FESEM)) and JEOL 2010 transmission electron microscope (TEM).

**5.2.3 Single  $\text{In}_2\text{O}_3$  nanowire device fabrication using bottom-up procedure.** Silicon wafer with 400-nm-thick thermal oxide film, which served as a substrate and back-gate in the device fabrication, was patterned with electrodes and diced into chips. The as-grown nanowires were carefully scratched off from the growth substrate and suspended in ethanol by sonication, then deposited on the silicon chip. After coated by PMMA through spin-coating (P6700 spin coater), electrodes on both ends of the nanowires were patterned through *e*-beam nanolithography (converted *e*-beam writing system using Carl Zeiss 1530 VP field emission scanning electron microscope (FESEM)), and the Ti/Au electrodes (source-S and drain-D) were deposited through

a Lesker PVD 75 electron beam evaporation system. Lastly, the chip was immersed in acetone overnight to remove the PMMA and lift-off metallic film.

**5.2.4 Device measurement.** Copper leads were applied to the as-fabricated nanowire device using silver paste, and source and drain electrodes were connected to a Keithley 2400-C sourcemeter to obtain current-voltage (I-V) curve. BK Precision DC regulated power supply was used to provide gate voltage in the investigation of field-effect transistor property.

**5.2.5 Biological detection of ricin.** Phosphate buffer saline (PBS, pH=7.4, 10 mM phosphates, 137 mM NaCl, 2 mM KCl) and high purity water (HPLC grade) were purchased from Aldrich. Surface cleaning of  $\text{In}_2\text{O}_3$  NW devices was achieved by submerging in acetone, ethanol, and hot water for 5 min each and then dried with nitrogen. The ricin samples with different concentration (maximum concentration is: antibody 0.03 mg/ml, and antigen 0.01 mg/ml) were made in PBS buffer solution. During the measurements, water, PBS buffer, and ricin samples were introduced into microfluidic channel through inlet and outlet in sequence, and the conductance of the NW was recorded under ambient conditions.

**5.2.6 Incubation procedure of  $\text{In}_2\text{O}_3$  nanowire with biological species.** As described in the previous chapter,  $\text{In}_2\text{O}_3$  nanowire was first synthesized using CVD method then scratched off from the substrate and dispersed in water. An identical volume of the nanowire dispersion was dropped on cover slips with 8 mm diameter and 0.150 mm thickness and dried in air. Then the cover slips were transferred to a 48-well plate, facing up, and rinsed with 1 ml of 1x PBS one time before the first chemical/bio-species solution was applied. Solutions were then added in the

indicated order with four times of rinsing (water, PBS or PBS with 0.1% Tween-20, 1 ml/rinse) in between. After the last step and washing using PBS, the cover slips are sealed on glass slides using Aqua-mount and dried in the dark.

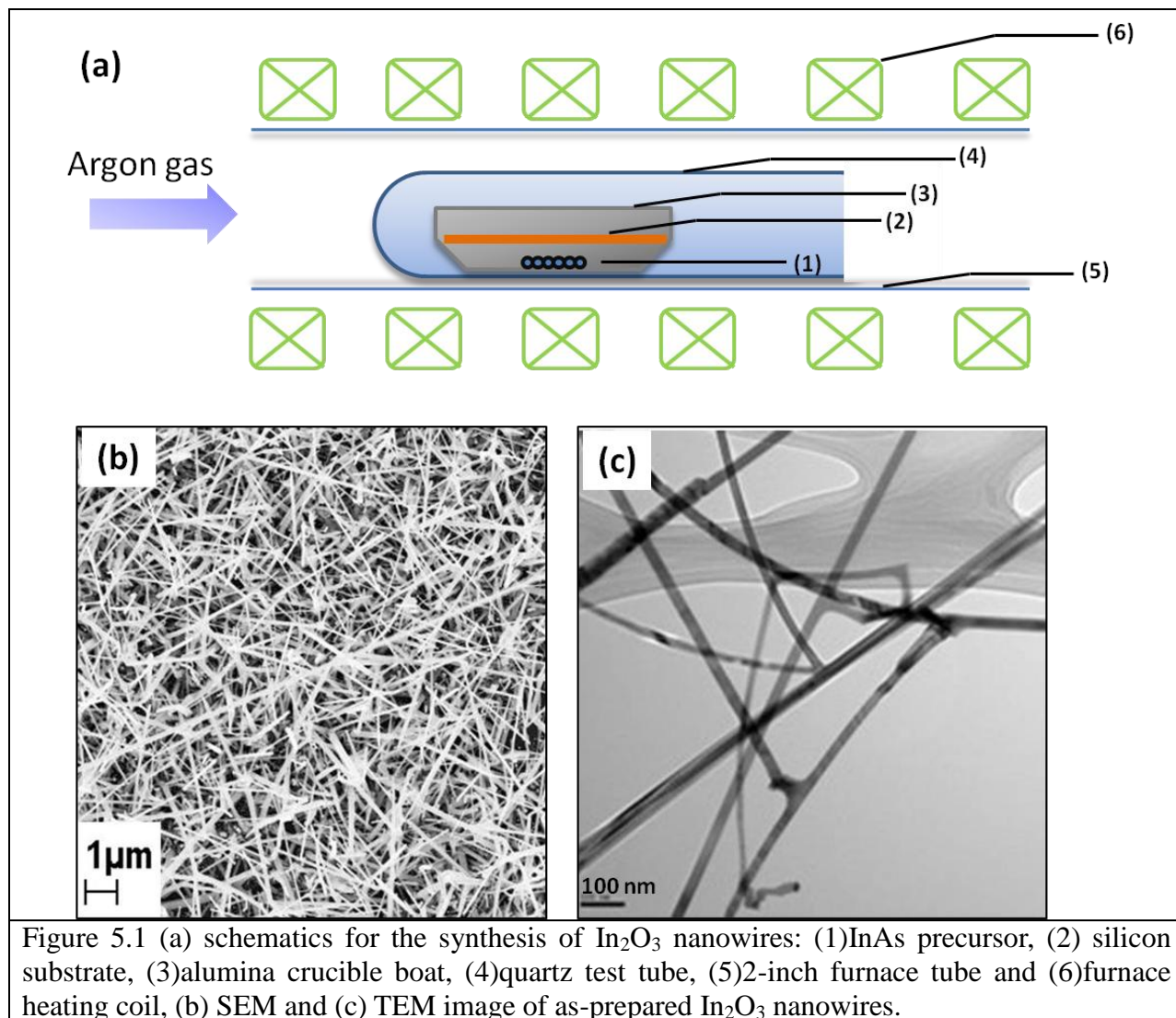
**5.2.7 Characterizations.** A Carl Zeiss 1530 VP field emission scanning electron microscope (FESEM) and JEOL 2010 LaB6 transmission electron microscope (TEM) at an accelerating voltage of 200kv was used to examine the morphologies and sizes of the nanowire.

## **5.3 Result and discussion**

### **5.3.1 Device fabrication of $\text{In}_2\text{O}_3$ nanowire based field-effect transistor**

**5.3.1.1  $\text{In}_2\text{O}_3$  nanowire synthesis.** The synthesis of semiconducting  $\text{In}_2\text{O}_3$  nanowires was performed using chemical vapor evaporation method (CVD).<sup>14</sup> As shown in Figure 5.1 (a), the reaction assembly consisted of precursor, substrate, crucible boat, and quartz test tube. The purpose of using this relatively complicated setup comparing to conventional CVD is to concentrate the InAs and  $\text{In}_2\text{O}_3$  vapor as much as possible and prevent it from being disturbed and diluted by argon flow, therefore the density and yield of nanowires can be increased. The furnace tube was first pumped to vacuum and inflated with argon. This pump-inflate cycle was repeated multiple times in order to remove all other gas. After temperature rise to 550 °C, the reaction assembly (part (1)-(4) in Figure (a)) was pushed to the central heating area. High purity InAs was selected as the reaction precursor under 1 atm argon environment. It vaporized rapidly due to the sudden heat, reacted with trace amounts of oxygen in the furnace tube, oxidized into  $\text{In}_2\text{O}_3$ , and eventually formed nanowires upon contact with the silicon substrate which was deposited with Au nanoparticle as the catalyst. Minority part of InAs stayed unoxidized and

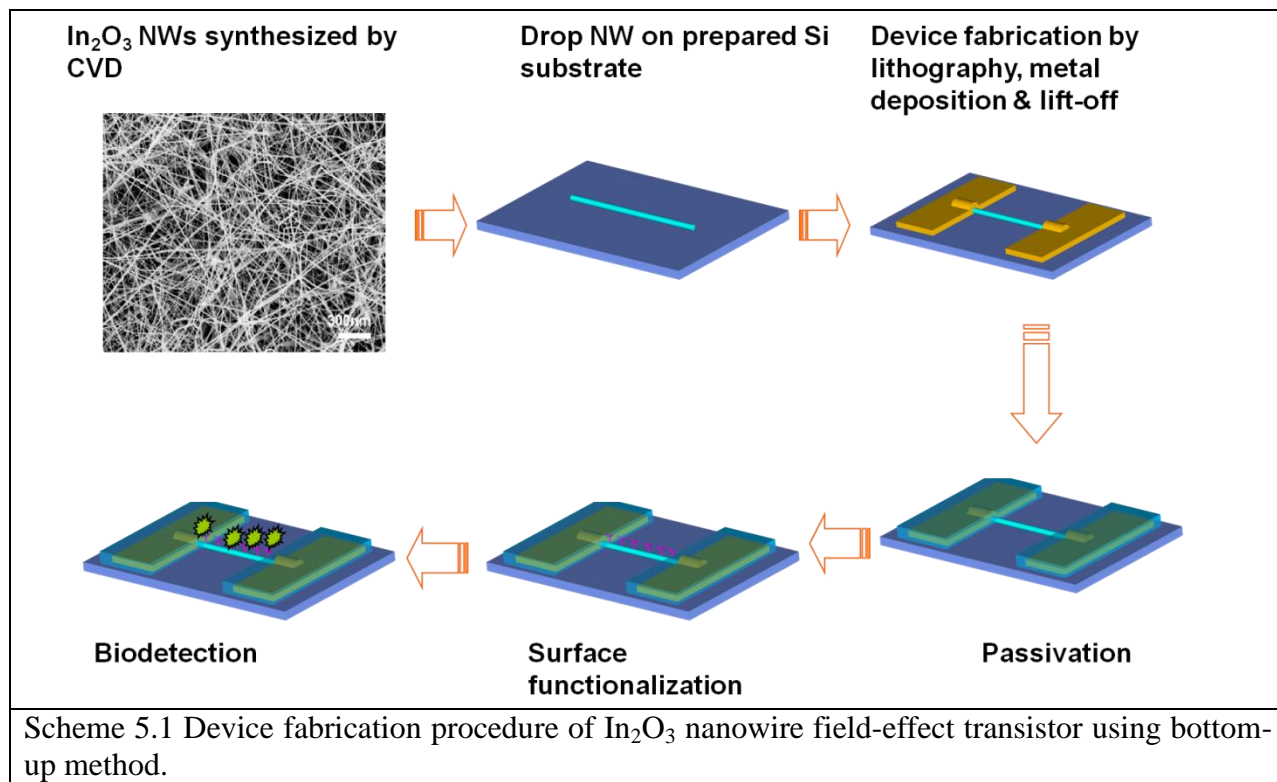
remained in the product, while the arsenic served as a dopant in the n-type semiconducting nanowire. The amount of dopant was primarily controlled by the concentration of oxygen in the furnace tube. More cycles of pump-inflate of argon before the rising of furnace temperature can help further reduce the oxygen and increase degree of doping, which is favorable for obtaining semiconductors with higher conductivity.



As longer nanowires are more convenient for e-beam lithography during the device fabrication process, the synthesis of  $\text{In}_2\text{O}_3$  nanowires was conducted for at least 12 hrs to achieve better length. The nanowire was then directly examined by SEM on the original growth substrate

as shown in Figure 5.1 (b). Average length was around 5 microns with some of them above 10 microns, and the diameter varies from 20 to 50 nm (Figure 5.1 (c)). Also, the nanowire growth exhibited high density which is also preferred for device fabrication.

**5.3.1.2 Device fabrication.** As-synthesized  $\text{In}_2\text{O}_3$  nanowire (NW) was removed from the growth substrate, suspended in ethanol by sonication and deposited onto doped Si wafers with 600-nm-thick thermal oxide film and electrode pattern. Then Ti/Au electrodes were deposited on the ends of the NWs by electron beam lithography, metal evaporation, and liftoff process. For the purpose of bio-sensing application, the NW device was passivated with PMMA which only exposed the FET channel. Then the device was integrated with microfluidic channels for convenient bio-agent injection and detection. The procedure is illustrated in Scheme 5.1.



An SEM image of as-fabricated NW device after metal deposition and lift-off is shown in Figure 5.2 (a). Single NW is bonded between two electrodes about 2  $\mu\text{m}$  apart through e-beam lithography. After being connected to the sourcemeter, the UV response of the semiconductor device was investigated and recorded in a dark room. As a characteristic property of semiconducting materials, UV exposure can increase the density of charge carriers, therefore enhancing the conductivity. As seen in Figure 5.2 (b), under source-drain voltage  $V_{\text{ds}}=1.0\text{ V}$ , the current, which representing conductivity of nanowire, increases simultaneously upon the application of UV light and reduces in a steep manner while UV is removed. The current is able to recover close to the original status and the procedure is repeatable multiple times. This sensitive UV response confirms that the as-synthesized  $\text{In}_2\text{O}_3$  nanowire is indeed a semiconductor.

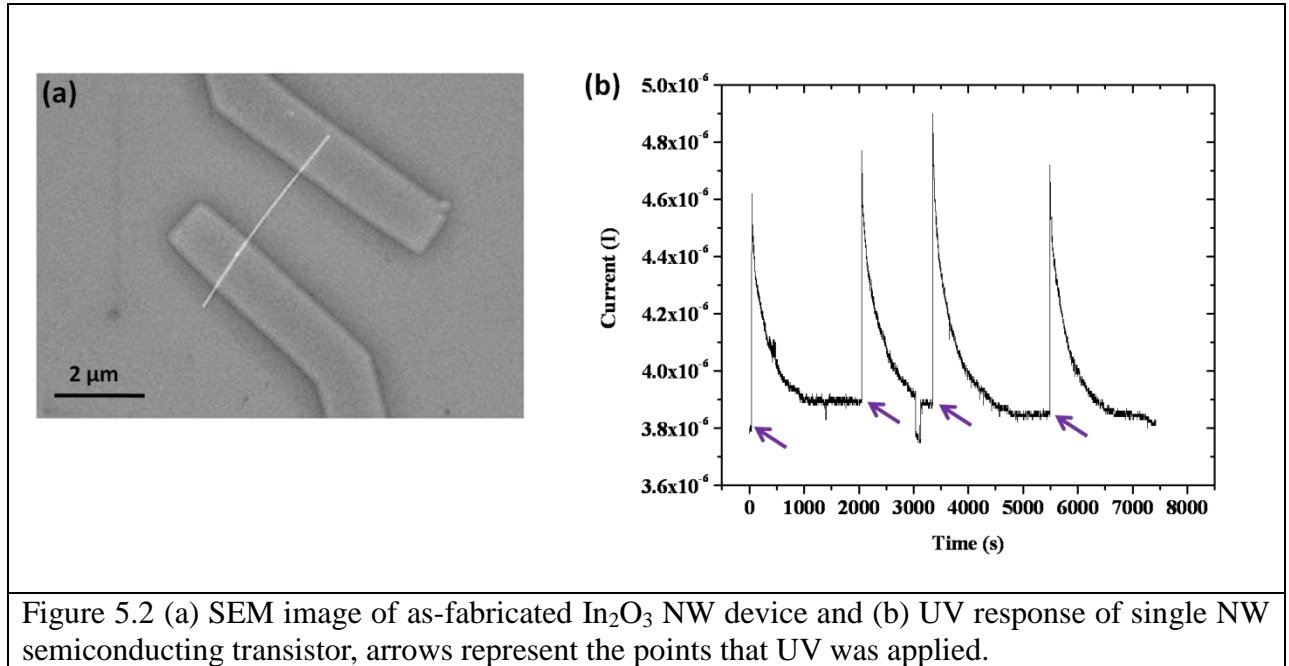


Figure 5.2 (a) SEM image of as-fabricated  $\text{In}_2\text{O}_3$  NW device and (b) UV response of single NW semiconducting transistor, arrows represent the points that UV was applied.

**5.3.1.3 Device measurement.** The field-effect transistor property of the  $\text{In}_2\text{O}_3$  NW was studied. Different biases were applied through the back-gate at the bottom of the device and a series of

current-voltage (I-V) curves between the source and drain were recorded in dry air conditions. Being an n-type semiconductor which has electrons as charge carriers, the  $\text{In}_2\text{O}_3$  nanowire shall respond to gate voltage change in a positive manner. Positive gate voltage can attract negative charge carriers (electrons) to move and concentrate as the gate area, therefore forming a conductive channel between the source and drain, while negative gate voltage repels the electrons and doesn't significantly change the distribution of the electrons. As shown in Figure 5.3 (a), the slope of the I-V curves, which represents the conductivity of the NW, increases gradually as the gate voltage changes from -14.9 V to 24.9 V. The result can be exhibited more clearly by extracting the current under a fixed source-drain voltage ( $V_{ds}=1.0$  V) of all the I-V curves to generate an  $I_{ds}$  (source-drain current)- $V_{gs}$  (gate-source voltage) curve as seen in Figure 5.3 (b). The current of the NW device is lower than  $10^{-8}$  A under negative gate voltage, and increases in a linear behavior under positive gate voltage with an improvement of an order as gate voltage changed from 0 to 24.9 V, suggesting an excellent transistor behavior in dry air.

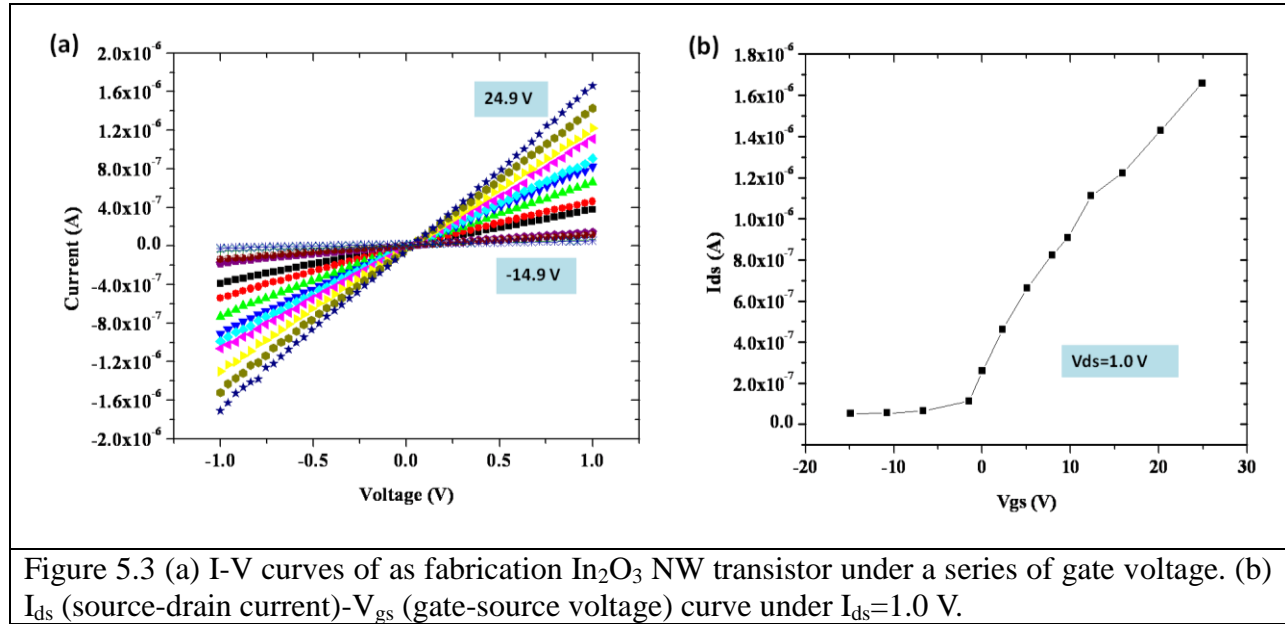
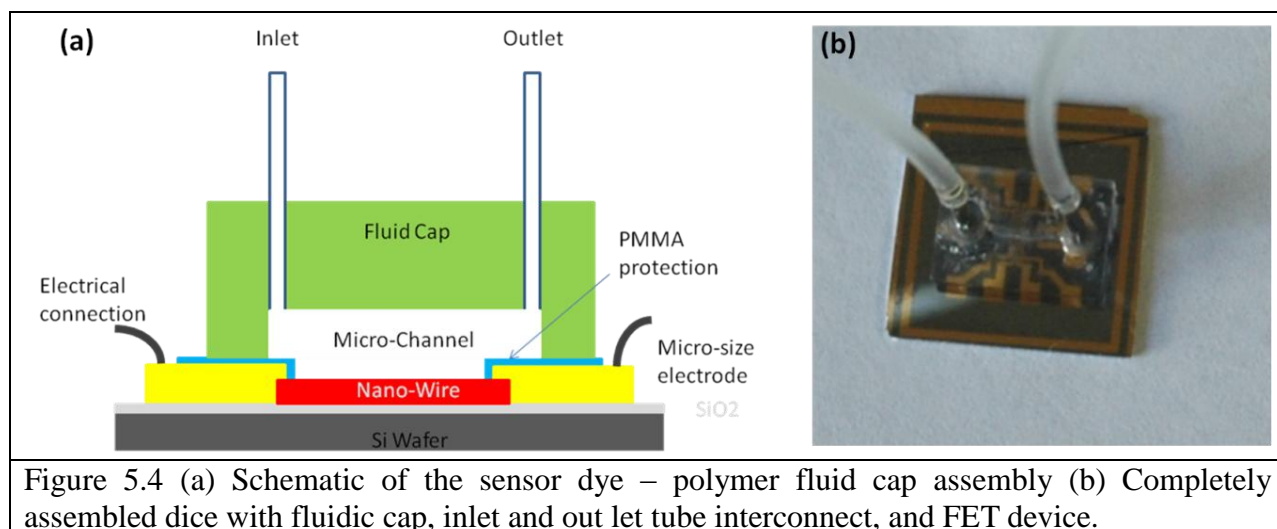


Figure 5.3 (a) I-V curves of as fabrication  $\text{In}_2\text{O}_3$  NW transistor under a series of gate voltage. (b)  $I_{ds}$  (source-drain current)- $V_{gs}$  (gate-source voltage) curve under  $I_{ds}=1.0$  V.

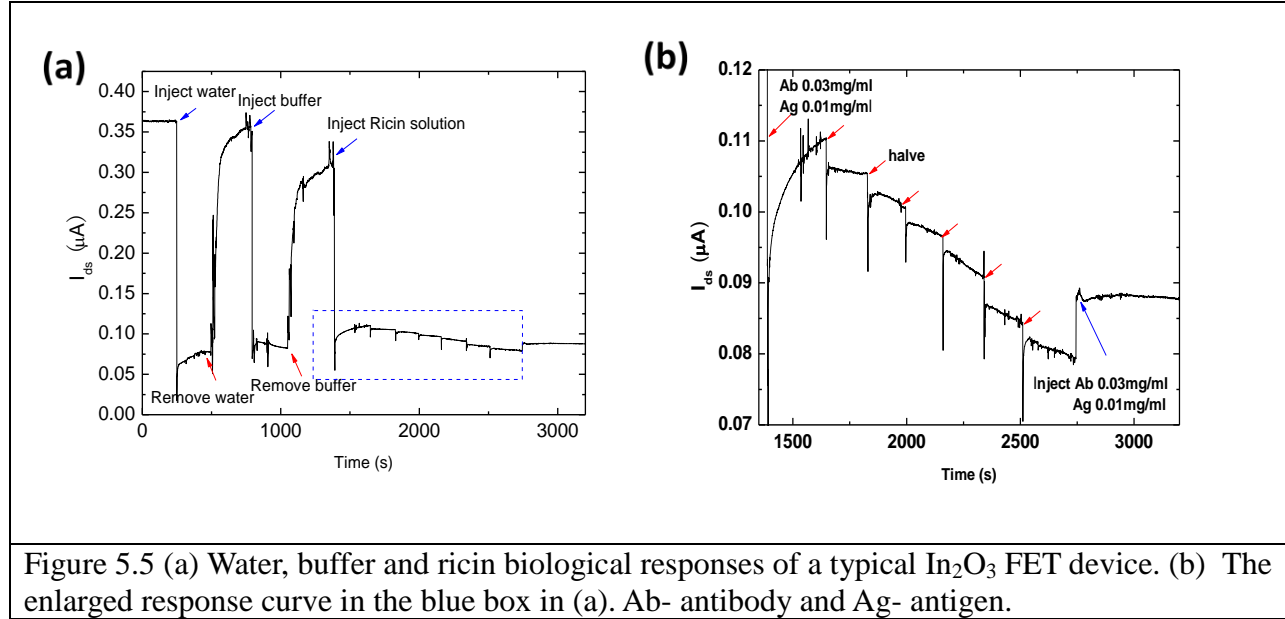


**5.3.1.4 Microfluidic channel integration.** Figure 5.4 (a) illustrates the principle arrangement of the FET biosensor device integrated with the microfluidic channel. The Si-based nanowire electrode chip is sealed with a polymer fluidic cap which allows for introduction of sample fluid into the cavity. Through selective binding targeting bio-agents such as antigens to the nanowires, a change in electrical signal from the nanowires can be induced, which can be registered for the presence of specific molecules in the fluid. The electrode pattern is covered with PMMA layer, leaving only an  $\text{In}_2\text{O}_3$  nanowire window area accessible to fluids carrying biological samples across the electrode area. Figure 5.4 (b) is a top view of the integrated device, showing the assembled microfluidic-channel-on-transistor chip with the sample inlet and outlet pipes ready for surface modification and bio-detection.

**5.3.1.5 Preliminary detection of ricin.** Prior to biological detection, an I-V property test was performed under 1.0 V source-drain voltage in dry air and the source-drain current remained stable during a 16-hour-test, which verified that the transistor was robust and suitable for long term continuous usage. The bio-agents, ricin-A-chain (RAC) and its antibody were then



introduced to test the performance by monitoring the conductance of the FET device. The antibody used here is modified by adding 6X-Histidine tag for metal chelation to the C-terminus of the antibody heavy chains to get better affinity with the nanowire surface.



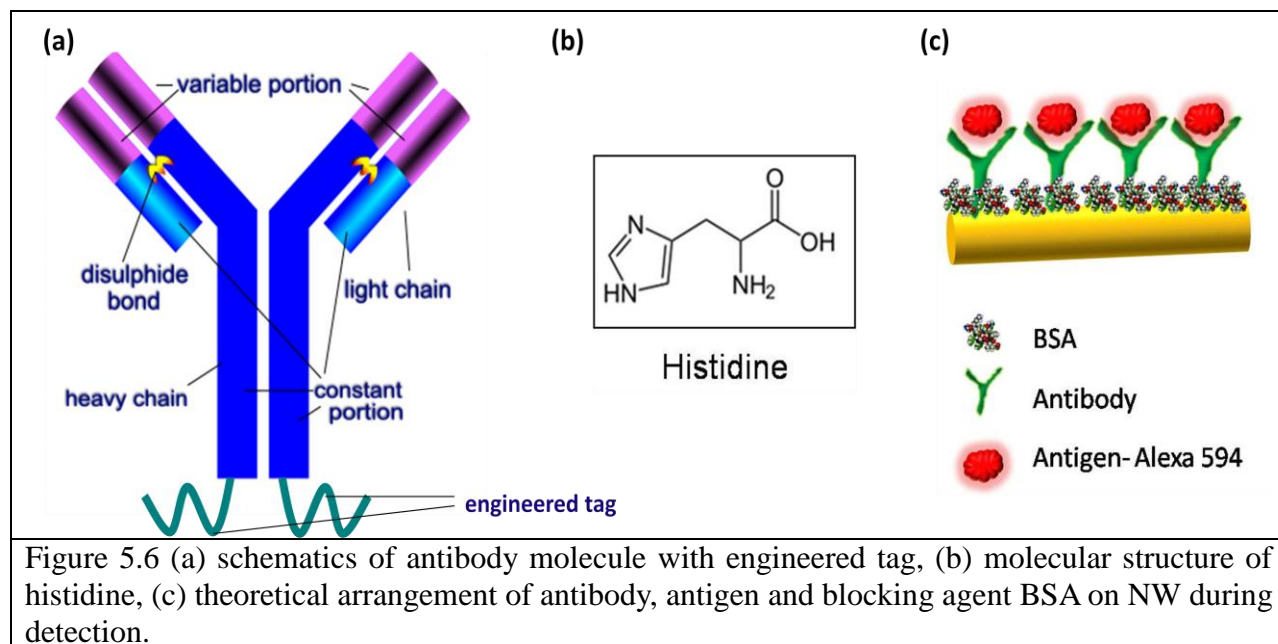
At first, water was injected into the inlet (the current monitored over time under  $V_{ds} = 1.0V$  and  $V_g = 0V$ ), and the current decreased immediately as shown in Figure 5.5 (a), and then returned to the original state once water was removed by air flow. This may be explained as the partially negatively charged oxygen atoms in water molecules have higher affinity with  $In_2O_3$  surface in the form of metal-oxygen conjugate bond than hydrogen atoms, hence providing extra electrons on nanowire surface and inducing the conductance to drop. Then a phosphate buffer saline (PBS, pH=7.4) solution was introduced and similar results were obtained because of additional conjugation effort between  $In_2O_3$  and negative charged phosphate. As the solution of ricin (0.01 mg/L) and its antibodies (0.03 mg/L) were introduced to the device, the current decreased immediately because of PBS, and then increased gradually as a slower response to ricin and antibody. Dilution of this antigen-antibody solution was performed for several times to

achieve 1/2, 1/4, 1/8... of original concentration and injected into the microfluidic channel. As shown in Figure 5.5 (b), the current reduced in a stepwise manner after each injection, which indicates concentration dependent sensitivity. Finally, the current increased again once the ricin solution with high concentration was applied. This current/conductance change compared with that of PBS of the nanowire exposure to solution can be attributed to the charging status of bio-agents. According to the calculation targeting on the amino acid sequence of ricin A chain and its antibody, the ricin-antibody complexes appear to have a theoretical isoelectric point (pI) around 8.6 and carry positive charge in a pH 7.4 PBS buffer, and ricin A chain, has a theoretical pI (isoelectric point) around 6.14, and carry negative charge in a pH 7.4 PBS buffer. While binding on the  $\text{In}_2\text{O}_3$  nanowire surface, they will act as gate voltage and lead to the change of carrier density in the FET. This preliminary text of ricin indicates that the  $\text{In}_2\text{O}_3$  NW device is sensitive to the change of charge from bio-species with different concentration, and it is a promising material for more sophisticated bio-sensing detection.

### **5.3.2 Nonspecific binding of between bio-species and $\text{In}_2\text{O}_3$ nanowire**

**5.3.2.1 Engineered antibody.** The molecule of antibody consists of a constant portion which is common among all antibodies from one species, and a variable portion which is designated to capture specific antigens, as shown in Figure 5.6 (a). The antibody molecules can only be attached to the NW through weak interaction forces such as Van Der Waals forces, electrostatic forces that majorly depend on the amino acids located on the surface of the antibody, therefore the efficiency of binding cannot be guaranteed. Even though binded to the NW, the antibody molecules are in random orientation in which the antigens binding site is not perfectly exposed. By adding engineered tags of 6 amino acid sequences at the end of heavy chains, the antibody is

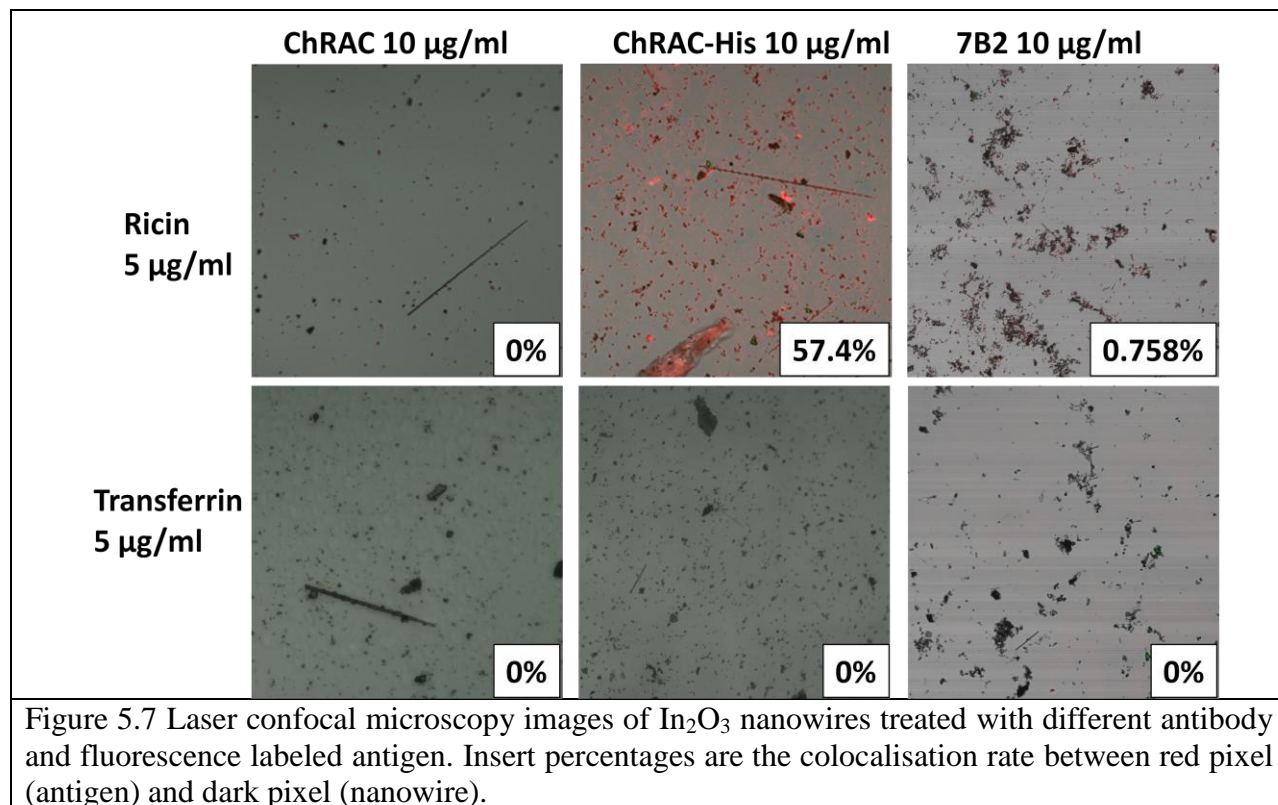
capable of binding to the nanowire more efficiently with an oriented position which exposes the antigen binding site. Histidine (Figure 5.6 (b)) is selected for building the engineered tag because of high affinity between the imidazole groups and metal/metal oxide materials through chelation bond, and no complexity from covalent conjugation using crosslinking reactions.



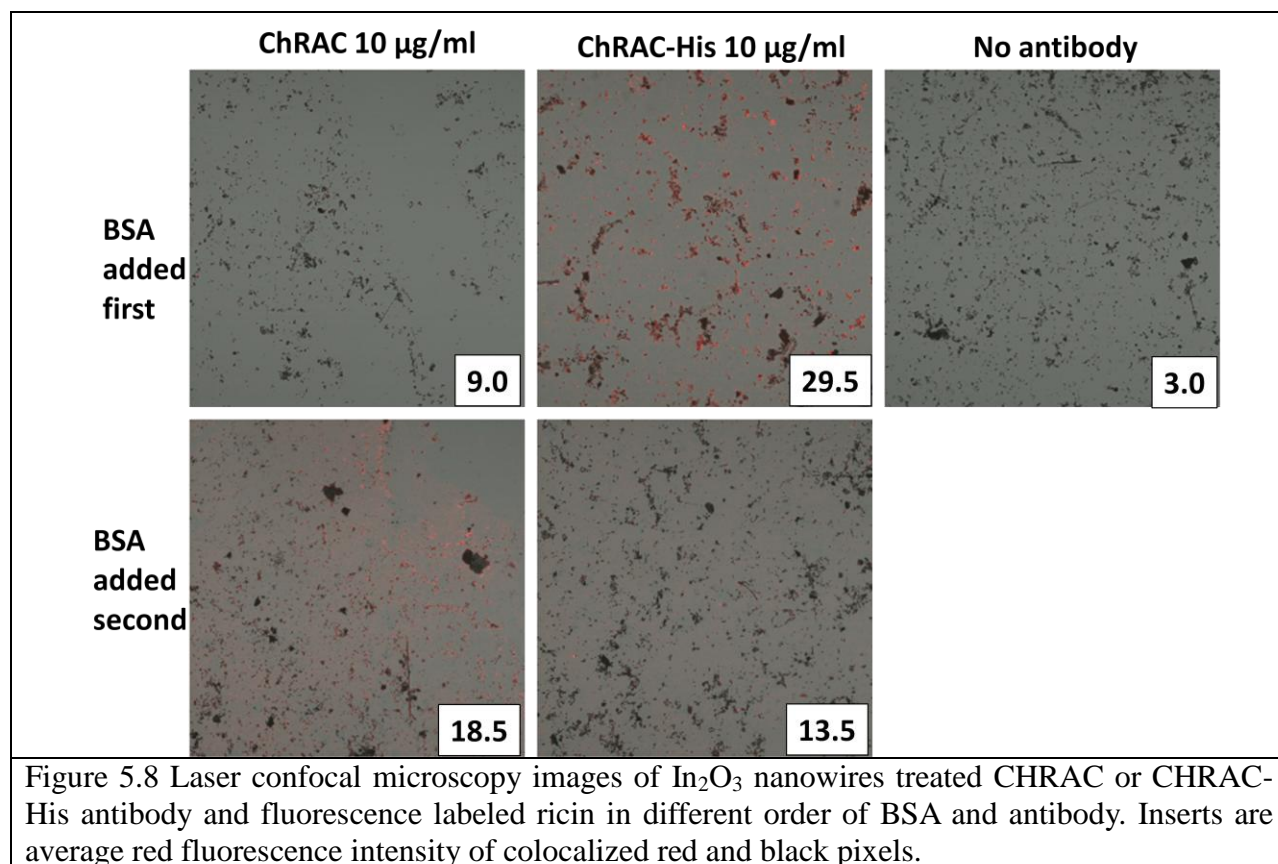
**5.3.2.2 Quantification of binding efficiency between nanowire, antibody and antigen.** The entire ricin detection procedure was simulated by using fluorescence labeled agents in order to confirm successful antigen immobilization and avoid non-specific binding between nanowire and bio-molecules as illustrated in Figure 5.6 (c).  $\text{In}_2\text{O}_3$  nanowires were first deposited on cover slips in 48-well plates, then blocking agent BSA, antibodies and Alexa-594 nm conjugated antigens were applied in sequence. The samples were then sealed and analyzed under Zeiss LSM 510 laser confocal microscopy to obtain image quantification data.

To test the binding efficiency of engineered histidine tagged antibody, the nanowire samples were first treated with different antibodies. ChRAC and ChRAC-His are natural anti-ricin antibodies and engineered antibodies with a histidine tag, respectively. And 7B2 is an irrelevant

antibody which worked as the negative control. After that, bovine serum albumin was used as blocking agent to prevent unspecific binding between nanowire and antigen. At last, Alexa-594 nm conjugated ricin and irrelevant antigen transferring which served as control, were applied.

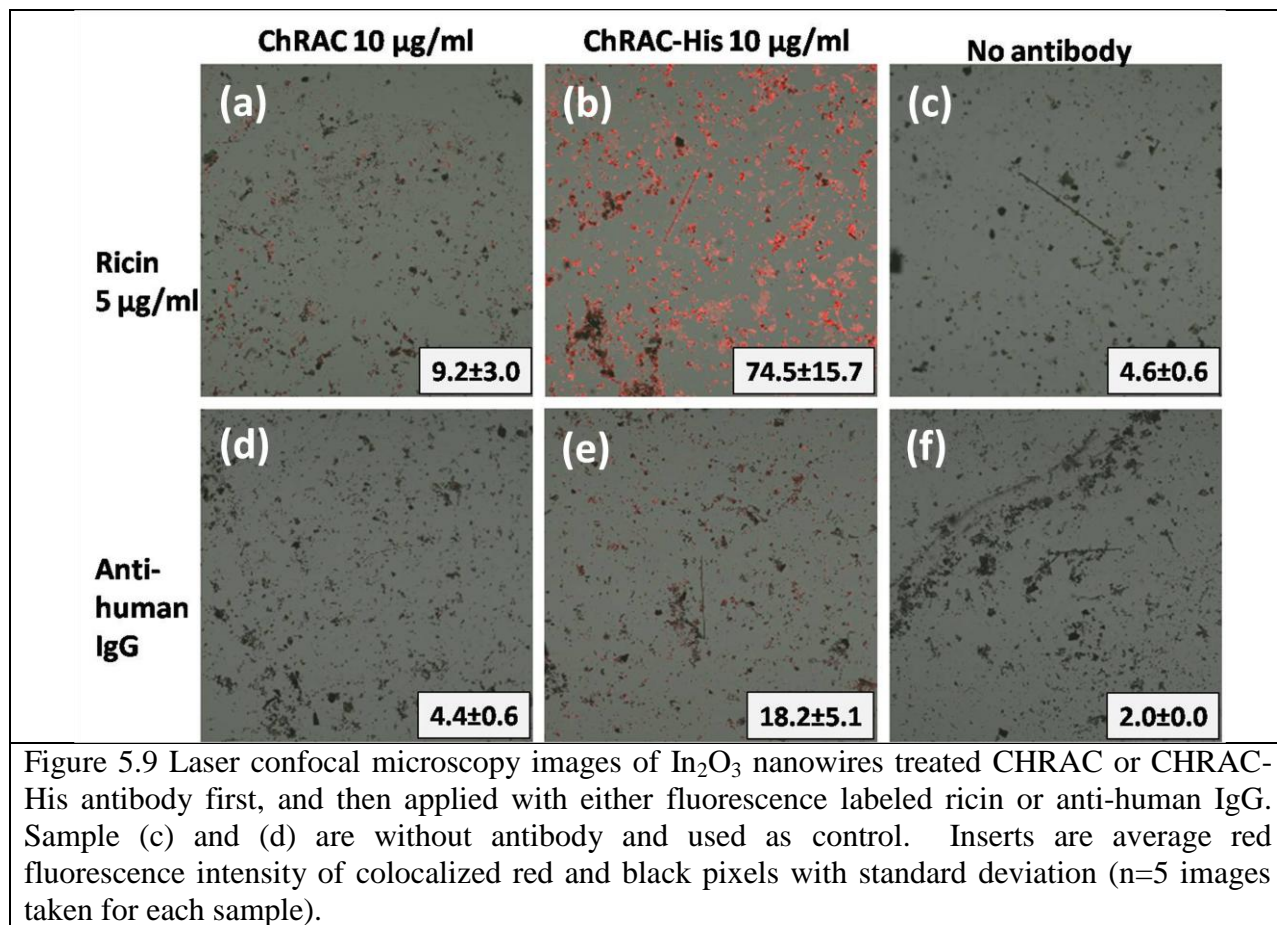


Laser confocal microscopy images (Figure 5.7) are shown with colocalisation percentage between red pixel (antigen) and dark pixel (nanowire), which indicates the successful binding of both antibody on NW and antigen on antibody. As mentioned before, since natural type CHRAC antibody can only bind to NW in low efficiency and the orientation is not optimized, few antigen molecules can be captured on NW as seen in Figure 5.7 (a), the colocalisation rate between NW and antigen is 0%. The ChRAC-His—ricin pair Figure 5.7 (b) yielded the highest colocalisation compared to the controls (Figure 5.7 (c)-(f)) which indicates that engineered ChRAC-His antibody is able to bind on the nanowire surface effectively in favored orientation to capture the targeted antigen specifically.



The order of adding BSA and antibody was also investigated. In most conventional bio-assays which involve antigen-antibody interaction, BSA is applied between antibody and antigen to block the uncovered area, in order to ensure not only sufficient binding of antibody on substrate, but also elimination of non-specific binding between antigen and substrate. In our experiment, two different adding orders, BSA-antibody-antigen and antibody-BSA-antigen were studied. A sample with no antibody (Figure 5.8 (c)) was prepared as a control. It was discovered unexpectedly that adding BSA before the engineered CHRAC-His antibody (Figure 5.8 (b)) gave a better efficiency on capturing antigen than the one with BSA added after antibody just like normal bio-assay (Figure 5.8 (d)). It is most likely caused by interaction between BSA and CHRAC-His molecules through exposed amino acid sequence. The detailed reason of this phenomenon is still under investigation. The sample with the sequence CHRAC-BSA-antigen

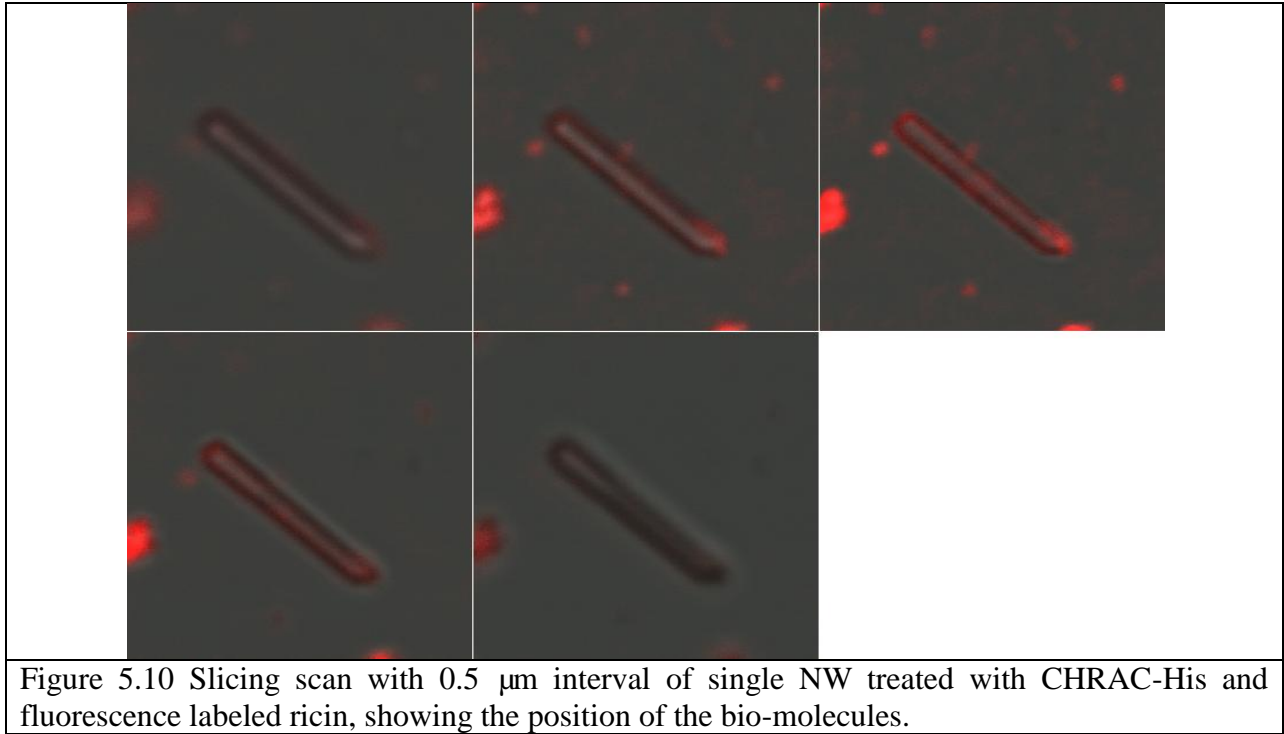
(Figure 5.8 (d)) gave the second highest intensity, but it is obvious from the image that a lot of red pixels are not colocalized with black pixel, suggesting lower blocking efficiency of BSA.



Similar procedures were performed to further confirm the immobilization of histidine-tagged antibody using secondary antibody. Phycoerythrin (PE) conjugated anti-human IgG, which specifically binds to human antibodies, was employed in the place of antigen, and the result was compared with the samples using fluorescence labeled ricin. Laser confocal microscopy images are shown in Figure 5.9 with average intensity of emission ( $n=5$  images per sample) from colocalized red and dark pixels. As seen in Figure 5.9 (e), PE labeled anti-human IgG was able to bind to CHRAC-His and present red fluorescence with higher intensity that colocalized with NW, compared to the sample with only natural type CHRAC (Figure 5.9 (c)) and no antibody (Figure



5.9 (f)). This result further confirms that the engineered CHRAC-His antibody is able to bind to NW surface and remain functional.



To ensure the antibody-antigen interaction did happen on the surface of NW instead of simply overlapped with NW on the fluorescence images, slicing scan along z axis with 0.5  $\mu\text{m}$  intervals was applied on a single nanowire after ChRAC-His binding and ricin-Alexa-594 nm treatment. As shown in Figure 5.10, red fluorescence that comes from labeled ricin is located all around the NW in the slicing image of middle session, but diminished in the image of top and bottom sessions, indicating that the ricin molecules are indeed captured on the surface of nanowire.

## 5.4 Conclusion

In this chapter, semiconductive  $\text{In}_2\text{O}_3$  nanowire was synthesized using CVD method. Back-gate device was fabricated through bottom up method and integrated with microfluidic channel

for bio-species detection. The nanowire device exhibits good field-effect property and is sensitive to the concentration change of antigens during the preliminary detection of ricin. At the same time, fluorescence label antigen ricin was used for simulating the entire bio-detection procedure on nanowire deposited on cover glass and examined by laser confocal microscopy. The result confirms that the engineered antibody is able to bind on NW and capture antigens more effectively than the nature type antibody.

## 5.5 References

- (1) Chen, Y.; Wang, X.; Hong, M. K.; Erramilli, S.; Mohanty, P.; Rosenberg, C. *Appl. Phys. Lett.* **2007**, *91*, 243511.
- (2) Chen, Y.; Wang, X.; Erramilli, S.; Mohanty, P.; Kalinowski, A. *Appl. Phys. Lett.* **2006**, *89*, 223512.
- (3) Cui, Y.; Wei, Q.; Park, H.; Lieber, C. M. *Science* **2001**, *293*, 1289.
- (4) Patolsky, F.; Zheng, G.; Hayden, O.; Lakadamyali, M.; Zhuang, X.; Lieber, C. M. *Proceedings of the National Academy of Sciences of the United States of America* **2004**, *101*, 14017.
- (5) Patolsky, F.; Zheng, G.; Lieber, C. M. *Nanomedicine* **2006**, *1*, 51.
- (6) Stern, E.; Klemic, J. F.; Routenberg, D. A.; Wyrembak, P. N.; Turner-Evans, D. B.; Hamilton, A. D.; LaVan, D. A.; Fahmy, T. M.; Reed, M. A. *Nature* **2007**, *445*, 519.
- (7) Zheng, G.; Patolsky, F.; Cui, Y.; Wang, W. U.; Lieber, C. M. *Nat Biotech* **2005**, *23*, 1294.
- (8) Li, C.; Zhang, D.; Liu, X.; Han, S.; Tang, T.; Han, J.; Zhou, C. *Appl. Phys. Lett.* **2003**, *82*, 1613.
- (9) Li, C.; Lei, B.; Zhang, D.; Liu, X.; Han, S.; Tang, T.; Rouhanizadeh, M.; Hsiai, T.; Zhou, C. *Appl. Phys. Lett.* **2003**, *83*, 4014.
- (10) Tang, T.; Liu, X.; Li, C.; Lei, B.; Zhang, D.; Rouhanizadeh, M.; Hsiai, T.; Zhou, C. *Appl. Phys. Lett.* **2005**, *86*, 103903.
- (11) Curreli, M.; Li, C.; Sun, Y.; Lei, B.; Gundersen, M. A.; Thompson, M. E.; Zhou, C. *J. Am. Chem. Soc.* **2005**, *127*, 6922.
- (12) Li, C.; Curreli, M.; Lin, H.; Lei, B.; Ishikawa, F. N.; Datar, R.; Cote, R. J.; Thompson, M. E.; Zhou, C. *J. Am. Chem. Soc.* **2005**, *127*, 12484.
- (13) Ishikawa, F. N.; Chang, H.-K.; Curreli, M.; Liao, H.-I.; Olson, C. A.; Chen, P.-C.; Zhang, R.; Roberts, R. W.; Sun, R.; Cote, R. J.; Thompson, M. E.; Zhou, C. *ACS Nano* **2009**, *3*, 1219.
- (14) Shen, G.; Chen, D. *J. Mater. Chem.* **2010**, *20*, 10888.



## **Chapter VI: Silicone Nanowire Based Field-Effect Transistor using Top-down Approach for Biosensing**

### **6.1 Introduction**

As mentioned in the previous chapter,  $\text{In}_2\text{O}_3$  nanowires have been a promising semiconducting nanomaterial for biological sensing. However, the synthesis methods of  $\text{In}_2\text{O}_3$  nanowires, such as chemical deposition<sup>1,2</sup> and laser ablation<sup>2</sup>, cause it to be difficult to control nanowires with uniform morphology and FET properties. Also, there is always an issue of poor quality FET fabricated through a bottom up technique, such as loosening electrode contacts. In addition, to perform selective detections, assembling nanowires in an ordered array is a big challenge for many research groups. Therefore, more homogenous nanowires and robust device architectures need to be explored. One effective solution is to utilize a top-down method (microelectronic device processing technique) to fabricate nanowire FET device,<sup>3</sup> in which the nanowire size and location can be predetermined through a precise lithography process which doesn't require 'manual' operation of nanowire alignment, giving a robust architecture.

On the other hand, single nanowire FET detection cannot be the conclusive measurement for the existence and concentration of bio-agents because it is neither capable of performing parallel control experiments nor selective sensing for a mixture sample which is necessary in biological studies. As silicon based FET has already shown its potential bio-sensor ability,<sup>4-8</sup> we are trying to fabricate highly repeatable and robust multiplexed silicon nanowire FET through a top-down method for a systematic detection of different bio-species.

### **6.2 Experimental**

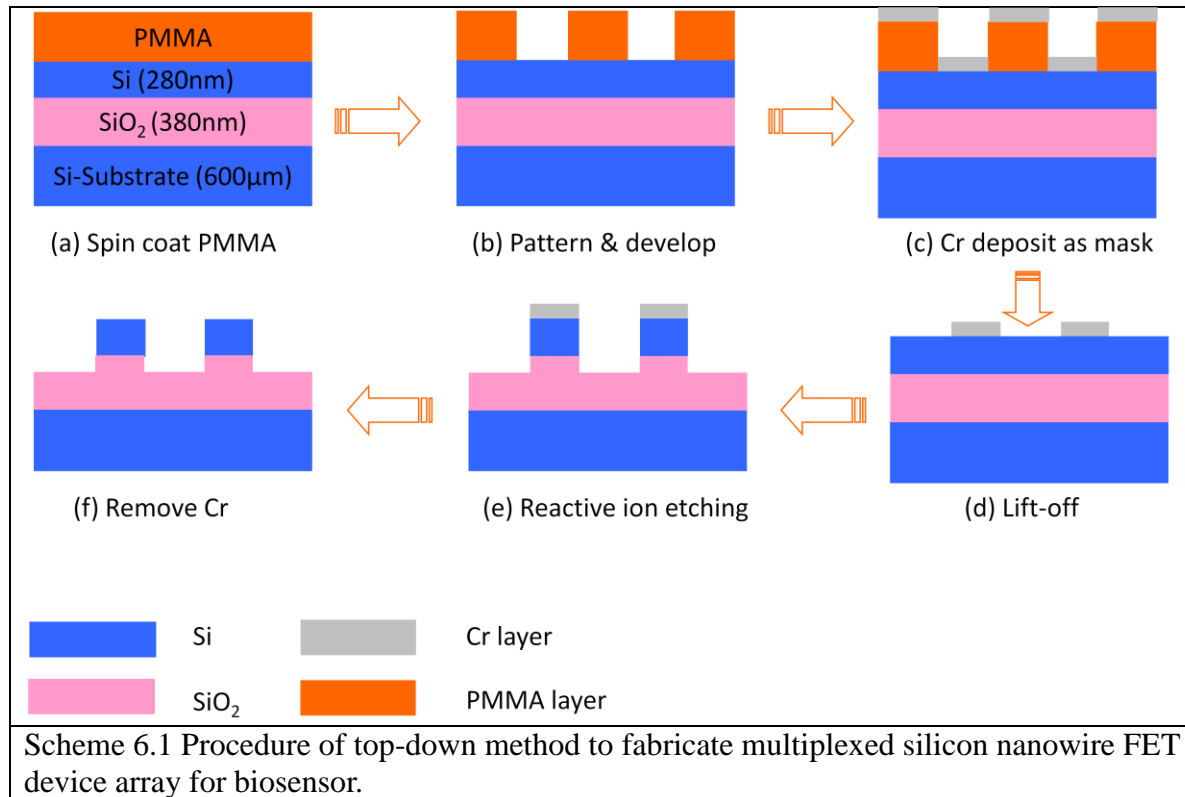
**6.2.1 Materials and chemicals.** Thin film silicon on insulator (SOI) wafer with 52.8 nm thick silicon layer and 156.4 nm thick oxidize layer was purchased from SIMGUI Technology. SOI wafer with a 280 nm silicon layer on top and a 380 nm oxide layer buried was purchased from University Wafer. Acetone (99.5%) and isopropyl alcohol (99.5%) were purchased from EMD Chemical. Absolute ethanol was purchased from AAPer Alcohol and Chemical Co. Positive electron beam resist Poly(methyl methacrylate) 495 PMMA A4, MIBK/IPA 1:3 developer and chromium etchant were purchased from MICROCHEM.

**6.2.2 Device fabrication.** The SOI wafer was first patterned with electrodes, using photoresist, and then diced to individual chips. Nanowires with demanded thickness and array shape were written through *e*-beam nanolithography on a spin-coated PMMA layer on the wafer. After PMMA etching, the patterned area is covered by a chromium mask with 30 nm thickness through metal deposition (Lesker PVD 75 electron beam evaporation system) and lift-off (in acetone overnight). Then the wafer is applied to reactive ion etching (RIE) in CF<sub>4</sub> gas to get the exposed silicon layer removed until reaching the silicon dioxide layer underneath to form silicon nanowires in the Cr covered area. After Cr mask removal, the as-designed silicon nanowire array is achieved.<sup>3</sup>

**6.2.3 Device measurement.** Copper leads were applied to the as-fabricated nanowire device using silver paste and copper leads to connect source and drain electrodes to a Keithley 2400-C sourcemeter to obtain the current-voltage (I-V) curve. BK Precision DC regulated power supply was use to provide gate voltage in the investigation of field-effect transistor property.

### 6.3 Result and discussion

**6.3.1 Device fabrication.** As shown in Scheme 6.1, silicon-on-insulator (SOI) wafers, with a 280 nm silicon layer on top and a 380 nm oxide layer buried, covered with PMMA are used to pattern the configuration of the desired silicon nanowire array by electron-beam lithography. After developing of PMMA, the patterned area is covered by a chromium mask through metal deposition and lift-off. Then the wafer is applied to reactive ion etching (RIE) to get the exposed silicon layer removed until reaching the silicon dioxide layer underneath to form silicon nanowires in the Cr covered area. After Cr mask removal, the as-designed silicon nanowire array is achieved.<sup>3</sup> The morphology of the as-fabricated silicon nanowire array is shown in Figure 6.1 and the wafer will be integrated with microfluidic channel.



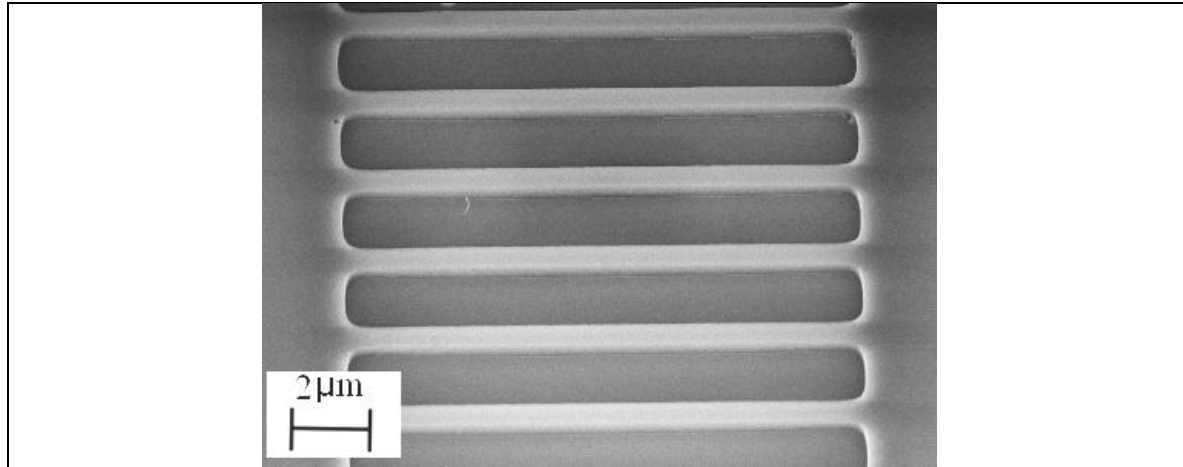


Figure 6.1 SEM images of nanowire array after removing Cr mask. The width of Si NW is about 300 nm.

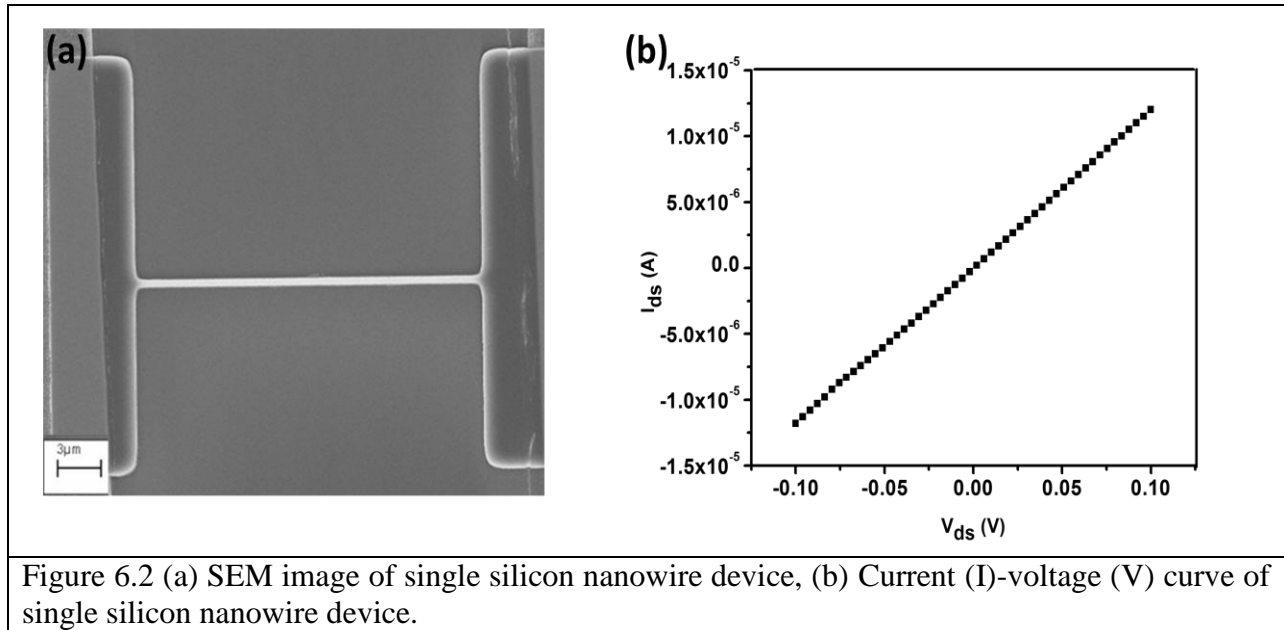


Figure 6.2 (a) SEM image of single silicon nanowire device, (b) Current (I)-voltage (V) curve of single silicon nanowire device.

**6.3.2 FET property.** The basic electrical properties of the as fabricated single, silicon nanowire device (Figure 6.2(a)) was investigated by measuring current (I)-voltage (V) curve as shown in Figure 6.2 (b). The I-V curve of a single nanowire shows very good conductivity with a conductance around 0.12 mS. However, the devices did not exhibit obvious gate-voltage dependence when applying various gate voltages. There are two factors that may contribute to the disappearance of the gate-effect. One is that the quality of the Si layer and insulator layer are

worsened during the fabrication process. It can be seen under SEM that there are some holes in insulator layer and defects on Si nanowires, which may affect the electrical properties of the device. In addition, current leaking was observed within the insulator layer which might have an effect on the field-effect property. Another reason is the carrier concentration in silicon layer on the insulator. The outstanding conductance indicates high carrier density, which may overwhelm the contribution of gate-voltage. We are continuing to optimize the fabrication process to obtain the Si nanowire device with gate effect for biosensor applications in the following work.

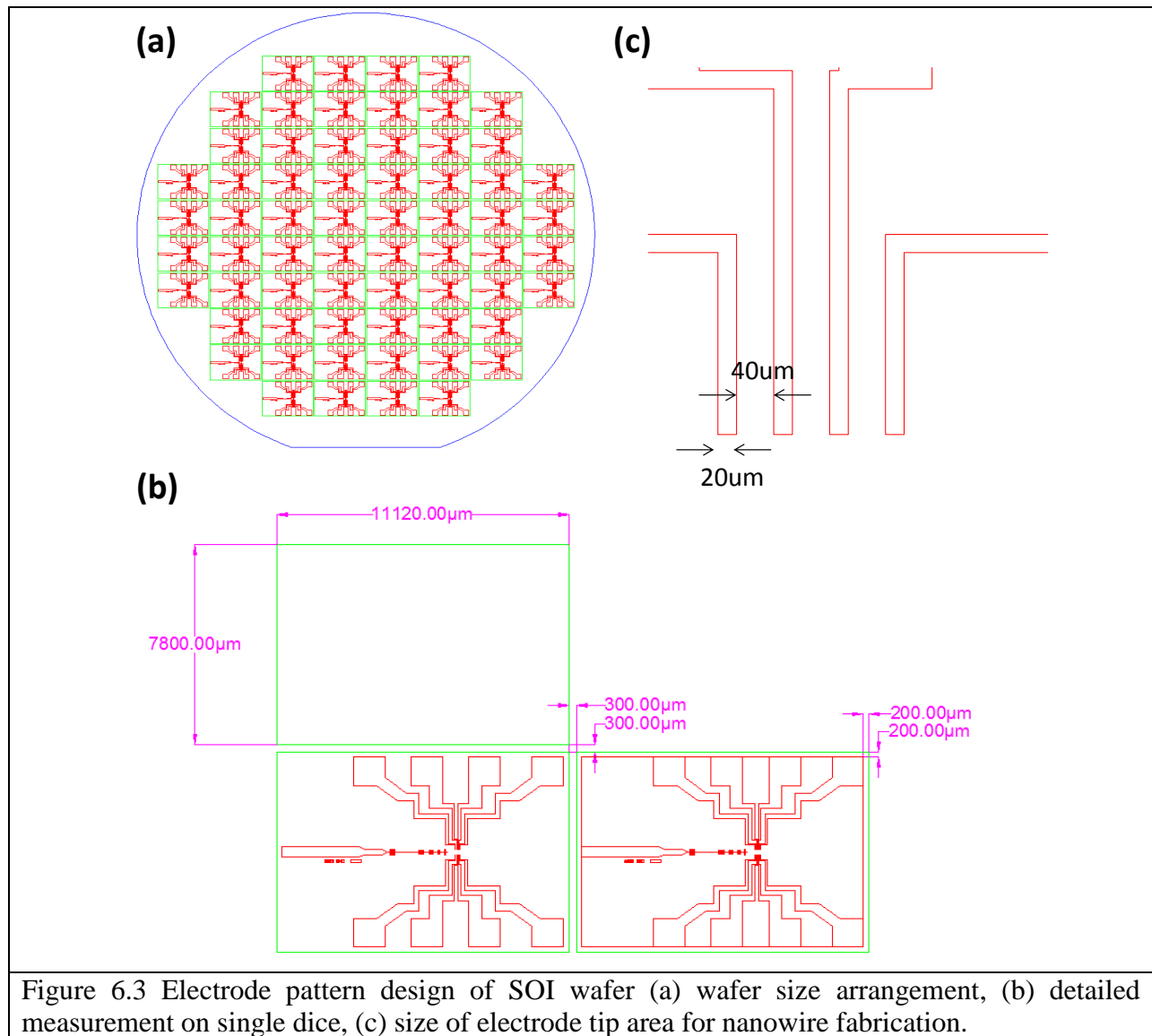
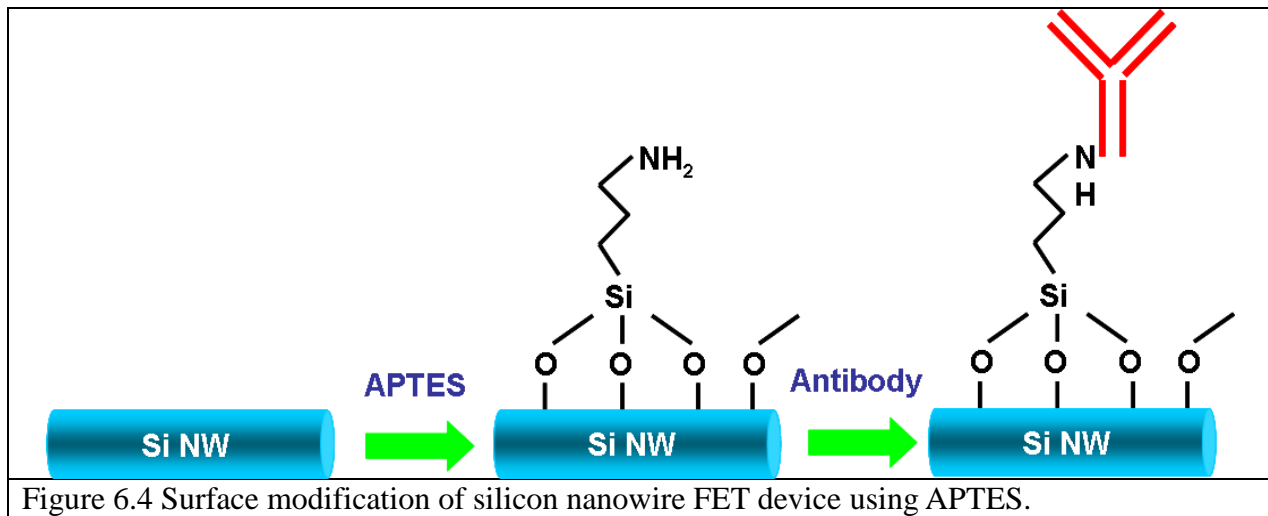


Figure 6.3 Electrode pattern design of SOI wafer (a) wafer size arrangement, (b) detailed measurement on single dice, (c) size of electrode tip area for nanowire fabrication.

**6.3.3 Design of wafer size electrode pattern.** To maximize the usage of each 4-inch SOI wafer, the previous wafer-size electrode pattern design which only carries 16 dices per wafer was revoked and a more efficient pattern has been developed as shown in Figure 6.3. In this design, a total number of 64 dices can be achieved (Figure 6.3 (a)) with electrode pads more separated from each other for convenient lead attachment (Figure 6.3 (b)). The electrode tips are 20  $\mu\text{m}$  in width with 40  $\mu\text{m}$  gap (Figure 6.3 (c)) to suit the working magnification and resolution during e-beam lithography and allows the length of written nanowires to be up to 40  $\mu\text{m}$ .



After the platform of silicon nanowire device using the top-down method was established, this technique can be employed to simultaneous multiplex detection for antigens due to the excellent uniformity between different nanowire devices. By starting this experiment, surface functionalization will be performed on silicon nanowire by using 3-aminopropyltriethoxysilane (APTES), leaving reactive amine groups for further functionalization<sup>4</sup> as shown in Figure 6.4. After that, different engineered antibodies will be immobilized on individual silicon nanowire devices through covalent binding on the same SOI wafer to achieve multiplexed selective detection as shown in Figure 6.5.

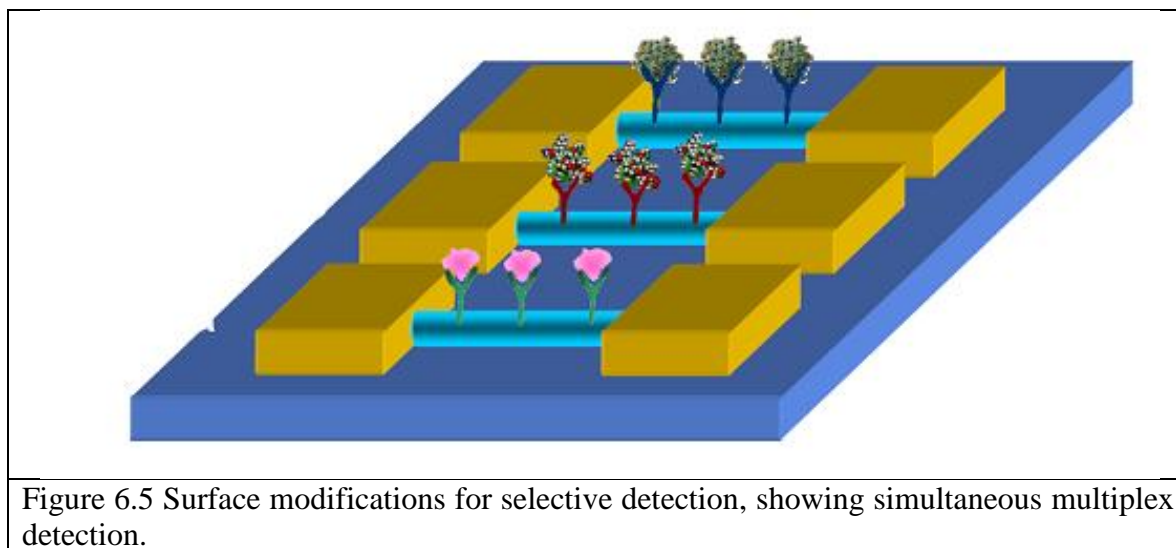


Figure 6.5 Surface modifications for selective detection, showing simultaneous multiplex detection.

## 6.4 Conclusion

In this chapter, e-beam lithography techniques were employed for top-down fabrication of silicon nanowires on SOI wafers for bio-sensing application. Investigation is still undergoing based on newly designed electrode patterns and SOI wafers with better quality to optimize the parameters during device fabrication in order to achieve the qualified field effect transistor property for multiplexed biosensor detection.



## 6.5 References

- (1) Zhongming, Z.; Kai, W.; Zengxing, Z.; Jiajun, C.; Weilie, Z. *Nanotechnology* **2009**, *20*, 045503.
- (2) Curreli, M.; Li, C.; Sun, Y.; Lei, B.; Gundersen, M. A.; Thompson, M. E.; Zhou, C. *J. Am. Chem. Soc.* **2005**, *127*, 6922.
- (3) Gao, Z.; Agarwal, A.; Trigg, A. D.; Singh, N.; Fang, C.; Tung, C.-H.; Fan, Y.; Buddharaju, K. D.; Kong, J. *Anal. Chem.* **2007**, *79*, 3291.
- (4) Cui, Y.; Wei, Q.; Park, H.; Lieber, C. M. *Science* **2001**, *293*, 1289.
- (5) Zheng, G.; Patolsky, F.; Cui, Y.; Wang, W. U.; Lieber, C. M. *Nat Biotech* **2005**, *23*, 1294.
- (6) Kim, A.; Ah, C. S.; Yu, H. Y.; Yang, J.-H.; Baek, I.-B.; Ahn, C.-G.; Park, C. W.; Jun, M. S.; Lee, S. *Appl. Phys. Lett.* **2007**, *91*, 103901.
- (7) Hsiao, C.-Y.; Lin, C.-H.; Hung, C.-H.; Su, C.-J.; Lo, Y.-R.; Lee, C.-C.; Lin, H.-C.; Ko, F.-H.; Huang, T.-Y.; Yang, Y.-S. *Biosens. Bioelectron.* **2009**, *24*, 1223.
- (8) Lin, C.-H.; Hung, C.-H.; Hsiao, C.-Y.; Lin, H.-C.; Ko, F.-H.; Yang, Y.-S. *Biosens. Bioelectron.* **2009**, *24*, 3019.


## Appendix: Copyright and Permission

Rightslink® by Copyright Clearance Center

<https://s100.copyright.com/AppDispatchServlet#formTop>



[Home](#) [Create Account](#) [Help](#)

**ACS Publications** High quality. High impact.

**Title:** Synthesis of Porous Magnetic Hollow Silica Nanospheres for Nanomedicine Application  
**Author:** J. Zhou et al.  
**Publication:** The Journal of Physical Chemistry C  
**Publisher:** American Chemical Society  
**Date:** Nov 1, 2007  
Copyright © 2007, American Chemical Society

User ID

Password

☐ [Enable Auto Login](#)

[LOGIN](#)

[Forgot Password/User ID?](#)

**If you're a copyright.com user,** you can login to RightsLink using your copyright.com credentials. Already a **RightsLink user** or want to [learn more?](#)

### PERMISSION/LICENSE IS GRANTED FOR YOUR ORDER AT NO CHARGE

This type of permission/license, instead of the standard Terms & Conditions, is sent to you because no fee is being charged for your order. Please note the following:

- Permission is granted for your request in both print and electronic formats, and translations.
- If figures and/or tables were requested, they may be adapted or used in part.
- Please print this page for your records and send a copy of it to your publisher/graduate school.
- Appropriate credit for the requested material should be given as follows:  
"Reprinted (adapted) with permission from (COMPLETE REFERENCE CITATION). Copyright (YEAR) American Chemical Society." Insert appropriate information in place of the capitalized words.
- One-time permission is granted only for the use specified in your request. No additional uses are granted (such as derivative works or other editions). For any other uses, please submit a new request.

If credit is given to another source for the material you requested, permission must be obtained from that source.

[BACK](#)[CLOSE WINDOW](#)

Copyright © 2013 Copyright Clearance Center, Inc. All Rights Reserved. [Privacy statement](#).  
Comments? We would like to hear from you. E-mail us at [customer@copyright.com](mailto:customer@copyright.com)



**AMERICAN INSTITUTE OF PHYSICS LICENSE  
TERMS AND CONDITIONS**

Jan 14, 2013

**All payments must be made in full to CCC. For payment instructions, please see information listed at the bottom of this form.**

|                                     |   |
|-------------------------------------|---|
| License Number                      | 3067841264168   |
| Order Date                          | Jan 14, 2013  |
| Publisher                           | American Institute of Physics   |
| Publication                         | Journal of Applied Physics  |
| Article Title                       | Fabrication of magnetic porous hollow silica drug carriers using CaCO <sub>3</sub> /Fe <sub>3</sub> O <sub>4</sub> composite nanoparticles and cationic surfactant double templates |
| Author                              | H. Ma, J. Zhou, D. Caruntu, M. H. Yu, et al.  |
| Online Publication Date             | Mar 31, 2008  |
| Volume number                       | 103   |
| Issue number                        | 7   |
| Type of Use                         | Thesis/Dissertation   |
| Requestor type                      | Author (original article)   |
| Format                              | Print and electronic  |
| Portion                             | Excerpt (> 800 words)   |
| Will you be translating?            | No  |
| Title of your thesis / dissertation | Nanomaterials for Biological Applications: Drug Delivery and Bio-sensing  |
| Expected completion date            | May 2013  |
| Estimated size (number of pages)    | 150   |
| Total                               | 0.00 USD  |

**Terms and Conditions**

American Institute of Physics -- Terms and Conditions: Permissions Uses

American Institute of Physics ("AIP") hereby grants to you the non-exclusive right and license to use and/or distribute the Material according to the use specified in your order, on a one-time basis, for the specified term, with a maximum distribution equal to the number that you have ordered. Any links or other content accompanying the Material are not the subject of this license.

**AMERICAN INSTITUTE OF PHYSICS LICENSE  
TERMS AND CONDITIONS**

Jan 14, 2013

**All payments must be made in full to CCC. For payment instructions, please see information listed at the bottom of this form.**

|                                     |   |
|-------------------------------------|---|
| License Number                      | 3067850088324   |
| Order Date                          | Jan 14, 2013  |
| Publisher                           | American Institute of Physics   |
| Publication                         | Journal of Applied Physics  |
| Article Title                       | Fabrication of magnetic porous hollow silica drug carriers using CaCO <sub>3</sub> /Fe <sub>3</sub> O <sub>4</sub> composite nanoparticles and cationic surfactant double templates |
| Author                              | H. Ma, J. Zhou, D. Caruntu, M. H. Yu, et al.  |
| Online Publication Date             | Mar 31, 2008  |
| Volume number                       | 103   |
| Issue number                        | 7   |
| Type of Use                         | Thesis/Dissertation   |
| Requestor type                      | Author (original article)   |
| Format                              | Print and electronic  |
| Portion                             | Figure/Table  |
| Number of figures/tables            | 4   |
| Title of your thesis / dissertation | Nanomaterials for Biological Applications: Drug Delivery and Bio-sensing  |
| Expected completion date            | May 2013  |
| Estimated size (number of pages)    | 150   |
| Total                               | 0.00 USD  |

**Terms and Conditions**

American Institute of Physics -- Terms and Conditions: Permissions Uses

American Institute of Physics ("AIP") hereby grants to you the non-exclusive right and license to use and/or distribute the Material according to the use specified in your order, on a one-time basis, for the specified term, with a maximum distribution equal to the number that you have ordered. Any links or other content accompanying the Material are not the subject of this license.

**AMERICAN INSTITUTE OF PHYSICS LICENSE  
TERMS AND CONDITIONS**

Jan 14, 2013

**All payments must be made in full to CCC. For payment instructions, please see information listed at the bottom of this form.**

|                                     |  |
|-------------------------------------|--|
| License Number                      | 3067850280599  |
| Order Date                          | Jan 14, 2013   |
| Publisher                           | American Institute of Physics  |
| Publication                         | Journal of Applied Physics   |
| Article Title                       | Synthesis of magnetic porous hollow silica nanotubes for drug delivery   |
| Author                              | H. Ma, J. Tarr, M. A. DeCoster, J. McNamara, et al.                      |
| Online Publication Date             | Mar 12, 2009   |
| Volume number                       | 105  |
| Issue number                        | 7  |
| Type of Use                         | Thesis/Dissertation  |
| Requestor type                      | Author (original article)  |
| Format                              | Print and electronic   |
| Portion                             | Excerpt (> 800 words)  |
| Will you be translating?            | No   |
| Title of your thesis / dissertation | Nanomaterials for Biological Applications: Drug Delivery and Bio-sensing |
| Expected completion date            | May 2013   |
| Estimated size (number of pages)    | 150  |
| Total                               | 0.00 USD   |

**Terms and Conditions**

American Institute of Physics -- Terms and Conditions: Permissions Uses

American Institute of Physics ("AIP") hereby grants to you the non-exclusive right and license to use and/or distribute the Material according to the use specified in your order, on a one-time basis, for the specified term, with a maximum distribution equal to the number that you have ordered. Any links or other content accompanying the Material are not the subject of this license.

**AMERICAN INSTITUTE OF PHYSICS LICENSE  
TERMS AND CONDITIONS**

Jan 14, 2013

**All payments must be made in full to CCC. For payment instructions, please see information listed at the bottom of this form.**

|                                     |  |
|-------------------------------------|--|
| License Number                      | 3067850388191  |
| Order Date                          | Jan 14, 2013   |
| Publisher                           | American Institute of Physics  |
| Publication                         | Journal of Applied Physics   |
| Article Title                       | Synthesis of magnetic porous hollow silica nanotubes for drug delivery   |
| Author                              | H. Ma, J. Tarr, M. A. DeCoster, J. McNamara, et al.                      |
| Online Publication Date             | Mar 12, 2009   |
| Volume number                       | 105  |
| Issue number                        | 7  |
| Type of Use                         | Thesis/Dissertation  |
| Requestor type                      | Author (original article)  |
| Format                              | Print and electronic   |
| Portion                             | Figure/Table   |
| Number of figures/tables            | 3  |
| Title of your thesis / dissertation | Nanomaterials for Biological Applications: Drug Delivery and Bio-sensing |
| Expected completion date            | May 2013   |
| Estimated size (number of pages)    | 150  |
| Total                               | 0.00 USD   |

**Terms and Conditions**

American Institute of Physics -- Terms and Conditions: Permissions Uses

American Institute of Physics ("AIP") hereby grants to you the non-exclusive right and license to use and/or distribute the Material according to the use specified in your order, on a one-time basis, for the specified term, with a maximum distribution equal to the number that you have ordered. Any links or other content accompanying the Material are not the subject of this license.

## **Vita**

Hui Ma was born in Tianjin, China. She obtained her bachelor's degree in biological science from University of Science and Technology of China in 2007. In the same year, she came to the University of New Orleans and joined Professor Zhou's group at Department of Chemistry and Advanced Materials Research Institute (AMRI) to pursue a Ph.D. in material chemistry. She finished her study and got her doctoral degree in 2013.